Fermilab

FERMILAB-THESIS-1999-06

A Search for Production of Scalar Top At the Fermilab Tevatron Collider

by

Nichelle L. Bruner

B.S., Engineering Physics, United States Military Academy, 1989

DISSERTATION

Submitted in Partial Fulfillment of the
Requirements for the Degree of

Doctor of Philosophy
Physics

The University of New Mexico
Albuquerque, New Mexico

July, 1999

DEDICATION

To my husband and my parents

Acknowledgements

The person who deserves the most thanks is my husband, who helped me hold it together. My parents helped him with this.

I am very grateful to my advisor, Prof. Michael Gold, for his knowledge, guidance and support. We were assisted by Dr. Steve Worm who helped me not only with the analysis but helped me maintain my perspective.

A Search for Production of Scalar Top At the Fermilab Tevatron Collider

by

Nichelle L. Bruner

ABSTRACT OF DISSERTATION

Submitted in Partial Fulfillment of the
Requirements for the Degree of

Doctor of Philosophy
Physics

The University of New Mexico
Albuquerque, New Mexico

July, 1999

A Search for Production of Scalar Top At the Fermilab Tevatron Collider

by

Nichelle L. Bruner

B.S., Engineering Physics, United States Military Academy, 1989
Ph.D., Physics, University of New Mexico, 1999

ABSTRACT

We have searched for evidence of direct production of the scalar top quark in $p\overline{p}$ collisions at $\sqrt{s} = 1.8$ TeV using the Collider Detector at Fermilab. We conducted the search assuming two different scenarios for decay of the scalar top. In the first, the scalar top quark decays into a bottom quark and a chargino with 100% probability. If this decay is not kinematically allowed, the scalar top quark decays into a bottom quark, a lepton, and a scalar neutrino. The branching ratios for this decay are 1/3 for each lepton type. The event signatures are the same for both decays so the searches were conducted using the same data sample. We find no evidence for signal in either decay chanel and so set upper limits on the production cross section.

Table of Contents

List of Figures

List of Tables

Chapter 1

Theory and Motivation

This analysis is a search for evidence of new physics, namely supersymmetry in elementary particles and interactions. Supersymmetry has emerged as a viable and popular candidate for incorporating the existing theory of particles and interactions into a more fundamental theory. Assisting its rise in popularity is the continued development of string theory, of which supersymmetry is a key ingredient.

To motivate this analysis, I will give an overview of the existing theory, known as the Standard Model, and an introduction to supersymmetry with emphasis on those aspects relevant to this analysis. There are a number of introductory papers on supersymmetry [1, 2, 3, 4] which give a more thorough treatment of the subject and from which I draw much of the theory presented in Section 1.3.

1.1 The Standard Model

The Standard Model of the electromagnetic, weak, and strong interactions is the currently accepted, highly successful theory used to describe the properties and interactions of the elementary particles. It is a quantum field theory based on the symmetry group $SU(3)_c \times SU(2)_L \times U(1)_Y$ with spontaneous breaking of the $SU(2)_L \times U(1)_Y$ symmetry through the Higgs mechanism [5]. Interactions arise by requiring invariance under the local gauge transformations described by the group generators. The symmetry group $SU(3)_c$ describes the strong interaction. The broken $SU(2)_L \times U(1)_Y$ symmetry describes the weak and electromagnetic interactions. The constituent fields of the Standard Model fall into two groups: fermions and bosons.

The fermions are spin 1/2 particles that constitute ordinary matter; they are typically denoted by the Dirac spinor field, Ψ. The fundamental fermions are quarks, which feel the strong, weak, and electromagnetic forces, and leptons, which feel only the weak and electromagnetic forces. Each left-handed quark and lepton, $\Psi_L \equiv$

$\frac{1}{2}(1-\gamma_5)\Psi$, has a partner to which it is coupled by the weak interaction. The fermions and their weak force pairings are listed in Table 1.1. The fermion electric charge, Q, is also listed in Table 1.1 and is the same for both left handed and right-handed fermions, $\Psi_R \equiv \frac{1}{2}(1+\gamma_5)\Psi$. The weak isospin, t from $SU(2)_L$, and the weak hypercharge, Y from $U(1)_Y$, are defined by their relationship with electric charge: $Q = t_3 + Y/2$. These charges for the fermions are listed in Table 1.2. The charges are different for the left and right handed states of each fermion.

Table 1.1: The spin 1/2 constituents of the Standard Model, or fermions, grouped according to weak couplings.

fermion			electric charge
leptons			
electron neutrino (ν_e)	μ neutrino (ν_μ)	τ neutrino (ν_τ)	0
electron (e)	muon (μ)	τ	-1
quarks			
up (u)	charm (c)	top (t)	$+\frac{2}{3}$
down (d)	strange (s)	bottom (b)	$-\frac{1}{3}$

Table 1.2: The weak isospin and hypercharge values for the Standard Model fermions. The value t_3 is the third member of the weak isospin multiplet and Y is the hypercharge. The subscripts L and R stand for left and right, respectively, and are defined by $\psi_L \equiv \frac{1}{2}(1-\gamma_5)\psi$ and $\psi_R \equiv \frac{1}{2}(1+\gamma_5)\psi$. There are currently no right-handed neutrinos in the Standard Model.

fermion	t_3	Y
ν_{eL},$\nu_{\mu L}$,$\nu_{\tau L}$	$\frac{1}{2}$	-1
e_L,μ_L,τ_L	$-\frac{1}{2}$	-1
e_R,μ_R,τ_R	0	-2
u_L,c_L,t_L	$\frac{1}{2}$	$\frac{1}{3}$
u_R,c_R,t_R	0	$\frac{4}{3}$
d_L,s_L,b_L	$-\frac{1}{2}$	$\frac{1}{3}$
d_R,s_R,b_R	0	$-\frac{2}{3}$

The fundamental bosons are spin 0 or 1 particles which mediate the strong, weak, and electromagnetic interactions. These bosons and the forces they mediate are listed in Table 1.3.

Table 1.3: The spin 0 and 1 constituents of the Standard Model, or bosons, and the forces they mediate.

boson	electric charge	mediated force
photon (γ)	0	electromagnetic
gluon	0	strong
$W^{\pm}$	± 1	weak
Z^0	0	weak
Higgs (H or ϕ)	0	weak

The complete Standard Model Lagrange density is a sum of the densities for the various component fields:

$$\begin{aligned}
\mathcal{L} &= \mathcal{L}_{\text{fermion}} + \mathcal{L}_{\text{scalar}} + \mathcal{L}_{\text{gauge}} + \mathcal{L}_{\text{Yukawa}} \\
&= \overline{\Psi}_L i\gamma^\mu \Big(\partial_\mu + ig\sigma \cdot \mathbf{W}_\mu + \frac{i}{2}g'Y_\mu\Big)\Psi_L + \overline{\Psi}_R i\gamma^\mu \Big(\partial_\mu + \frac{i}{2}g'Y_\mu\Big)\Psi_R \\
&\quad + \frac{1}{2}\Big|\Big(\partial_\mu + ig\sigma \cdot \mathbf{W}_\mu + \frac{i}{2}g'Y_\mu\Big)\phi\Big|^2 - \frac{1}{2}\mu^2\phi^\dagger\phi - \frac{1}{4}|\lambda|(\phi^\dagger\phi)^2 \\
&\quad - \frac{1}{4}\mathbf{W}_{\mu\nu} \cdot \mathbf{W}^{\mu\nu} - \frac{1}{4}Y_{\mu\nu}Y^{\mu\nu} \\
&\quad - G_f[\overline{\Psi_R}(\phi^\dagger\Psi_L) + (\overline{\Psi_L}\phi)\Psi_R]. \qquad (1.1)
\end{aligned}$$

This is the Lagrange density before spontaneous symmetry breaking through the Higgs mechanism. Summation over the $SU(3)_c$ indices is assumed. The $SU(2)_L$ field is $\mathbf{W}$ and the coupling constant is g. The $U(1)_Y$ field is Y with coupling g'. The Higgs field is the only scalar and is denoted by ϕ (and sometimes H.) The Higgs-fermion couplings, referred to as the Yukawa couplings, are how mass terms are introduced for the fermions in a gauge invariant way. The σ_i are the Pauli matrices. Usually, the gauge-covariant derivative, D_μ, defined by

$$D_\mu \equiv \partial_\mu + ig\sigma \cdot \mathbf{W}_\mu + \frac{i}{2}g'Y_\mu,$$

is substituted into Eq. 1.1. The term $-1/2\mu^2\phi^\dagger\phi$ breaks the electroweak symmetry because it forces ϕ to have a non-zero value in the vacuum. The mean value $\langle\phi\rangle_0$ breaks the symmetry and gives particles their masses. This brings the number of unspecified Standard Model parameters to 21, namely

- three coupling constants,
- six quark masses,

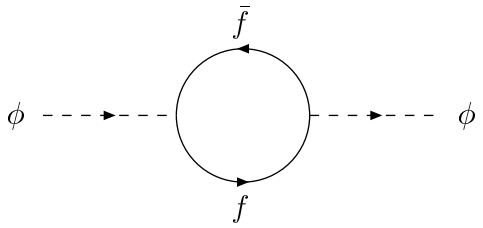

Figure 1.1: Feynman diagram for a fermionic contribution to the self energy of the Higgs boson.

- six lepton masses,
- three quark mixing angles and one phase, and
- the two scalar potential constants.

These parameters must be determined experimentally.

The Standard Model has endured rigorous experimental testing and made many successful predictions, among them

- the discovery of the charm, bottom, and top quarks,
- the discovery of the Z^0,
- and the absence of flavor changing neutral currents.

In spite of these successes, the Standard Model is widely considered not to be a fundamental theory, but rather a low energy effective theory. "Low energy" here means energies achievable in existing and proposed particle experiments, on the order of 10 TeV.

1.2 Problems with the Standard Model

The main problem with the Standard Model is the existence of quadratic divergences in the Yukawa interactions. Consider the one loop correction to the Higgs self energy[1], shown in Fig. 1.1, where G_f is the $\overline{\Psi}\phi\Psi$ coupling from Eq. 1.1 and $N(f)$ is the color

[1]This example of the Standard Model quadratic divergence is taken directly from Ref. [2].

factor after summing over color indices:

$$\begin{aligned}
\pi^f_{\phi\phi}(0) &= -N(f)\int \frac{d^4k}{(2\pi)^4}\mathrm{tr}\left[\left(i\frac{G_f}{\sqrt{2}}\right)\frac{i}{\not{k}-m_f}\left(i\frac{G_f}{\sqrt{2}}\right)\frac{i}{\not{k}-m_f}\right] \\
&= -2N(f)G_f^2\int\frac{d^4k}{(2\pi)^4}\frac{k^2+m_f^2}{(k^2-m_f^2)^2} \\
&= -2N(f)G_f^2\int\frac{d^4k}{(2\pi)^4}\left[\frac{1}{k^2-m_f^2}+\frac{2m_f^2}{(k^2-m_f^2)^2}\right]. \qquad (1.2)
\end{aligned}$$

We see that the first term is quadratically divergent. If instead of evaluating the integral at infinity, we evaluate at the Planck mass, the result would be ~ 30 orders of magnitude greater than the Standard Model Higgs mass, ~ 1 TeV, as it is assumed to be.

If we renormalized this quadratic divergence away as we do with logarithmic divergences, we are left with a correction term, of order $N(f)m_f^2G_f^2/8\pi$, which is independent of the Higgs mass and different for different orders of perturbation theory. Real problems occur if m_f is not just of the order of m_t but of the order of a much higher energy symmetry breaking scale. Then extremely fine tuning is needed to cancel a very large bare mass against very large loop corrections to give a Higgs mass on the order of the electroweak breaking scale, ~ 1 TeV. Moreover, this fine-tuning would be different for different orders of perturbation theory. This point becomes more important as we regard the Standard Model as only an effective theory that must be replaced by a more fundamental theory at higher energies such as a Grand Unified Theory.

This fine-tuning, considered unnatural by theorists, is referred to as the technical gauge hierarchy problem [3]. We can avoid this problem if there exist additional contributions to Eq. 1.2 that cancel the divergences. The additional contributions come from new complex scalar fields, $\tilde{f}_L$ and $\tilde{f}_R$. The new fields could couple to the Higgs as follows:

$$\mathcal{L}_{\phi\tilde{f}} = \frac{1}{2}G_{\tilde{f}}\,\phi^2\left(|\tilde{f}_L|^2+|\tilde{f}_R|^2\right)+vG_{\tilde{f}}\,\phi\left(|\tilde{f}_L|^2+|\tilde{f}_R|^2\right)+\left(\frac{G_{\tilde{f}}}{\sqrt{2}}A_f\phi\tilde{f}_L\tilde{f}_R^*+h.c.\right). \quad (1.3)$$

Then the addition to Eq. 1.2 is

$$\begin{aligned}
\pi^{\tilde{f}}_{\phi\phi}(0) &= -G_{\tilde{f}}N(\tilde{f})\int\frac{d^4k}{(2\pi)^4}\left[\frac{1}{k^2-m^2_{\tilde{f}_L}}+\frac{1}{k^2-m^2_{\tilde{f}_R}}\right] \\
&+ (G_{\tilde{f}}\,v)^2N(\tilde{f})\int\frac{d^4k}{(2\pi)^4}\left[\frac{1}{(k^2-m^2_{\tilde{f}_L})^2}+\frac{1}{(k^2-m^2_{\tilde{f}_R})^2}\right] \\
&+ |G_{\tilde{f}}A_f|^2N(\tilde{f})\int\frac{d^4k}{(2\pi)^4}\frac{1}{(k^2-m^2_{\tilde{f}_L})(k^2-m^2_{\tilde{f}_R})}.
\end{aligned}$$

All quadratic divergences cancel if the following hold:

$$\begin{aligned} N(\tilde{f}) &= N(f) \quad \text{and} \\ G_{\tilde{f}} &= -G_f^2. \end{aligned}$$

And if $m_{\tilde{f}} = m_f$ and $A_f = 0$, the total correction vanishes.

These nice features have led to the proposal that there exists a supersymmetric operator that transforms fermions into bosons and bosons into fermions such that all other quantum numbers are preserved. The change in the Lagrange density under a supersymmetric transformation leads to explicit definitions of these supersymmetric operators. Since the change in the Lagrange density due to a supersymmetric transformation is shown in Ref. [4] to be a total derivative, the action and equations of motion are demonstrated to be invariant under supersymmetry. We will use the most general renormalizable, supersymmetric, gauge-invariant Lagrange density, given in Ref. [4], as the starting point in the next section.

1.3 The MSSM Lagrangian

In the Minimal Supersymmetric Standard Model (MSSM), the Standard Model is combined with supersymmetry with the goals of minimizing the number of new particles and interactions and remaining consistent with observation. Starting with Eq. 1.3, we have adopted the convention that supersymmetric partners are denoted with a tilde. In addition, an "s-" is added to the beginning of names of scalar superpartners to Standard Model fermions (quark $\leftrightarrow$ squark), while "-ino" is added to the end of names of fermionic superpartners to bosons (photon $\leftrightarrow$ photino). Without the terms that could break the supersymmetry, the MSSM Lagrange density is [4]

$$\begin{aligned} \mathcal{L} &= -\frac{1}{4} v^a_{mn} v_a^{mn} - i\overline{\lambda}^a \overline{\sigma}^m \mathcal{D}^{ab}_m \lambda^b - \overline{\mathcal{D}^{ij}_m \phi^j} \mathcal{D}^{mik} \phi^k - i\overline{\psi}^i \overline{\sigma}^m \mathcal{D}^{ij}_m \psi^j \\ &\quad -\frac{1}{2} g_a^2 (\overline{\phi}_i T^a_{ij} \phi_j)^2 + i\sqrt{2} g_a (\overline{\phi}_i T^a_{ij} \psi_j \lambda^a - \overline{\lambda}^a \overline{\psi}_i T^a_{ij} \phi_j) \\ &\quad -\frac{1}{2} m_{ij} \psi_i \psi_j - \frac{1}{2} \overline{m}_{ij} \overline{\psi}_i \overline{\psi}_j - g_{ijk} \psi_i \psi_j \phi_k - \overline{g}_{ijk} \overline{\psi}_i \overline{\psi}_j \overline{\phi}_k \\ &\quad -|m_{ij} \phi_j + g_{ijk} \phi_j \phi_k|^2, \end{aligned} \tag{1.4}$$

where ψ is a two-component spinor, v^a_{mn} is the Yang-Mills field strength tensor, a is an index in the adjoint representation of the gauge group, λ^a is the gaugino, T^a_{ij} is the generator of the gauge group a ($SU(3)_c \times SU(2)_L \times U(1)$), and g is the gauge coupling. In this notation, the $\mathbf{T}^a$ generators represent the group $SU(3)_c \times SU(2)_L \times U(1)$, and are dimensioned accordingly. The gauge-covariant derivatives are:

$$\mathcal{D}_m \phi^i = \partial_m \phi^i + igA^a_m T^a \phi^i,$$

$$\begin{aligned}\mathcal{D}_m\psi^i &= \partial_m\psi^i + igA_m^aT^a\psi^i, \quad \text{and} \\ \mathcal{D}_m\lambda^a &= \partial_m\lambda^a - gf_{abc}A_m^b\lambda^c.\end{aligned}$$

The first line in Eq. 1.4 is the kinetic terms for the gauge, gaugino, and matter fields. The second line contains the quartic term required by supersymmetry and the trilinear coupling terms. The third line contains Majorana fermion mass terms and the Yukawa interactions. The interactions in the second line are completely specified by the gauge symmetries and supersymmetry. The couplings in the fourth line, the scalar potential, are completely unspecified. Keeping only the terms in Eq. 1.4 that are required to be consistent with experiment, m_{ij} becomes zero for Standard Model fermions.

The Yukawa interactions and Higgs scalar potential arise from terms in the superpotential:

$$\begin{aligned}V_{\text{super}} &= \sum_{i,j=1}^{3} \epsilon_{\alpha\beta}\Big[(G_e)_{ij}H_1^\alpha\tilde{l}_{iL}^\beta\tilde{e}_{jR}^* + (G_d)_{ij}H_1^\alpha\tilde{q}_{iL}^\beta\tilde{d}_{jR}^* + (G_u)_{ij}H_2^\beta\tilde{q}_{iL}^\alpha\tilde{u}_{jR}^* \\ &\quad +\mu\epsilon_{\alpha\beta}(H_2^\alpha H_1^\beta)\Big], \qquad (1.5)\end{aligned}$$

where i, j are the generation indices and α, β are the $SU(2)_L$ indices. Summation over the $SU(3)_c$ indices is assumed. For terms in the MSSM Lagrange density that are the product of fields, all fields in the term must have the same chirality. This is to preserve invariance under a supersymmetric transformation [4, 2]. Therefore a second Higgs doublet is needed in Eq. 1.5 to provide a mass term for the down-type quarks. The matrices $\mathbf{G_u}$ and $\mathbf{G_d}$ give rise to quark mixing and $\mathbf{G_e}$ may be diagonal. We may also make $\mathbf{G_u}$ diagonal so that all quark mixing is parameterized in $\mathbf{G_d}$, which is the standard convention. Eq. 1.5 contributes to the Lagrange density in the following way [2]

$$\mathcal{L}_V = -\sum_i \left|\frac{\partial V}{\partial\phi_i}\right|^2 - \frac{1}{2}\sum_{i,j}\left[\overline{\psi}_{iL}\frac{\partial^2 V}{\partial\phi_i\partial\phi_j}\psi_j + \text{h.c.}\right]. \qquad (1.6)$$

The second term gives rise to the Yukawa interactions.

The superpotential could contain terms with an odd number of superpartners such as

$$\epsilon_{ij}(c_1 l_L^i l_L^j\tilde{e}_R + c_2 l_L^i q_L^j\tilde{d}_R) + c_3 u_R d_R\tilde{d}_R^*.$$

These terms conserve electric charge, but violate lepton and baryon number conservation and could mediate proton decay through the exchange of a down squark. Since proton decay is not observed, we omit these terms from the superpotential. Requiring the superpotential to contain only terms with an even number of superpartners is called R-parity conservation.

If supersymmetry were unbroken, the supersymmetric particles would have the same masses as their Standard Model partners. Since we don't observe this, supersymmetry must be broken. Some of the more popular supersymmetric breaking terms are quadratic terms for the scalar fields and polynomials of the scalar fields with cubic terms being the highest order [4]. These terms are called "soft" breaking terms because they do not re-introduce the quadratic divergences that supersymmetry eliminated. They break supersymmetry by operating only on the scalars and not their superpartners. The following representation is from Ref. [2] with an added $\tilde{\nu}$ mass term:

$$\begin{aligned}\mathcal{L}_{\text{breaking}} &= -m_{\tilde{q}}^2|\tilde{q}_L|^2 - m_{\tilde{u}}^2|\tilde{u}_R^*|^2 - m_{\tilde{d}}^2|\tilde{d}_R^*|^2 - m_{\tilde{l}}^2|\tilde{l}_L|^2 - m_{\tilde{e}}^2|\tilde{e}_R^*|^2 - m_{\tilde{\nu}}^2|\tilde{\nu}_R^*|^2 \\ &\quad -(G_e A_e H_1 \tilde{l}_L \tilde{e}_R^* + \lambda_\nu A_\nu H_2 \tilde{l}_L \tilde{\nu}_R^* + G_d A_d H_1 \tilde{q}_L \tilde{d}_R^* + G_u A_u H_2 \tilde{q}_L \tilde{u}_R^* \\ &\quad + bH_1 H_2 + \text{h.c.}) \\ &\quad -m_1^2|H_1|^2 - m_2^2|H_2|^2 - \frac{1}{2}m_{\tilde{B}}\tilde{B}\tilde{B} - \frac{1}{2}m_{\tilde{W}}\tilde{W}\tilde{W} - \frac{1}{2}m_{\tilde{g}}\tilde{g}\tilde{g}. \end{aligned} \tag{1.7}$$

In this equation the $SU(2)_L$ and $SU(3)_c$ indices have been suppressed.

It is instructive to see the Higgs potential with the explicit couplings since these couplings contribute to the squark mass matrices to be discussed in the next section. The Higgs potential includes supersymmetry preserving and breaking terms from Eqs. 1.4 and 1.7 [1]:

$$\begin{aligned}V_{\text{Higgs}} &= (|\mu|^2 + m_2^2)(|H_2^0|^2 + |H_2^+|^2) + (|\mu|^2 + m_1^2)(|H_1^0|^2 + |H_1^-|^2) \\ &\quad + b[(H_2^+ H_1^- - H_1^0 H_1^0) + \text{h.c.}] \\ &\quad + \frac{1}{8}(g^2 + g'^2)(|H_2^0|^2 + |H_2^+|^2 - |H_1^0|^2 - |H_1^-|^2)^2. \end{aligned}$$

The Higgs self coupling, μ, is a free parameter, but g and g' are the couplings specified by the $\text{SU}(2)_L$ and $\text{U}(1)_Y$ gauges, respectively. The supersymmetry and gauge symmetry are broken in the same manner as in the Standard Model where the vacuum expectation values of H_1 and H_2 are v_1 and v_2, respectively. The masses of the physical Higgs particles and the gauge bosons are usually expressed in terms of the ratio of v_1 and v_2, namely

$$\tan\beta \equiv \frac{v_2}{v_1} \ .$$

The obvious drawback to the MSSM is that it introduces a superpartner for every Standard Model particle and a second Higgs doublet with its superpartner, none of which have been observed. The entire MSSM particle spectrum is listed in Table 1.4. A general parameterization of the supersymmetry breaking phenomenon introduces more than 100 free parameters[2].

Table 1.4: The Standard Model particle spectrum with the addition of a second Higgs doublet is shown on the left side of the table. The MSSM additions to the particle spectrum are shown on the right. The arrows indicate the mixing of weak eigenstates to form mass eigenstates. The braces ({}) indicate what is mixed in the weak sector. This table is taken from Ref. [6].

Standard Model with two Higgs doublets			MSSM			
Quarks (spin-$\frac{1}{2}$)	$\begin{pmatrix} u \\ d \end{pmatrix}_L$	u_R d_R	Squarks (spin-0)	$\begin{pmatrix} \tilde{u} \\ \tilde{d} \end{pmatrix}_L$	$\tilde{u}_R$ $\tilde{d}_R$	
	$\begin{pmatrix} c \\ s \end{pmatrix}_L$	c_R s_R		$\begin{pmatrix} \tilde{c} \\ \tilde{s} \end{pmatrix}_L$	$\tilde{c}_R$ $\tilde{s}_R$	
	$\begin{pmatrix} t \\ b \end{pmatrix}_L$	t_R b_R		$\begin{pmatrix} \tilde{t} \\ \tilde{b} \end{pmatrix}_L$	$\tilde{t}_R$ $\tilde{b}_R$	$\longrightarrow$ $\tilde{q}_{1,2}$
Leptons (spin-$\frac{1}{2}$)	$\begin{pmatrix} e \\ \nu_e \end{pmatrix}_L$	e_R	Sleptons (spin-0)	$\begin{pmatrix} \tilde{e} \\ \tilde{\nu}_e \end{pmatrix}_L$	$\tilde{e}_R$	
	$\begin{pmatrix} \mu \\ \nu_\mu \end{pmatrix}_L$	μ_R		$\begin{pmatrix} \tilde{\mu} \\ \tilde{\nu}_\mu \end{pmatrix}_L$	$\tilde{\mu}_R$	
	$\begin{pmatrix} \tau \\ \nu_\tau \end{pmatrix}_L$	τ_R		$\begin{pmatrix} \tilde{\tau} \\ \tilde{\nu}_\tau \end{pmatrix}_L$	$\tilde{\tau}_R$	$\longrightarrow$ $\tilde{l}_{1,2}$
Gauge bosons (spin-1)	g		Gauginos (spin-$\frac{1}{2}$)	$\tilde{g}$		
	γ			$\tilde{\gamma}$		Neutralinos
	Z			$\widetilde{Z}$		$\longrightarrow \widetilde{\chi}^0_{1,2,3,4}$
	$W^\pm$			$\widetilde{W}^\pm$		$\{\tilde{\gamma}, \widetilde{Z}, \widetilde{H}^0_{1,2}\}$
Higgs bosons (spin-0)	h, H, A		Higgsinos (spin-$\frac{1}{2}$)	$\widetilde{H}^0_{1,2}$		Charginos $\longrightarrow \widetilde{\chi}^\pm_{1,2}$
	$H^\pm$			$\widetilde{H}^\pm$		$\{\widetilde{W}^\pm, \widetilde{H}^\pm\}$

1.4 Motivation for a light $\tilde{t}_1$

The mass matrices for the squarks are created from the terms in Eqs. 1.4, 1.6, and 1.7 quadratic in the squark fields. Ignoring mixing between squark generations, we have six 2×2 mass matrices in the basis ($\tilde{q}_L$,$\tilde{q}_R$), one for each squark flavor. Diagonal contributions to the mass matrices come from the first term in Eq. 1.6:

$$\begin{aligned} \text{for } \tilde{u}_L: \quad & |G_u H_2^0 \tilde{u}_L|^2 = (G_u \frac{v_2}{\sqrt{2}})^2 = m_u^2 \text{ and} \\ \text{for } \tilde{u}_R: \quad & |G_u H_2^0 \tilde{u}_R^*|^2 = (G_u \frac{v_2}{\sqrt{2}})^2 = m_u^2, \end{aligned}$$

where, in the second step, H_2 was replaced by its vacuum expectation value. Other diagonal contributions come from the mass terms in Eq. 1.7, $m_{\tilde{u}}^2 |\tilde{u}_L|^2$ and $m_{\tilde{u}}^2 |\tilde{u}_R^*|^2$.

The last diagonal contribution comes from $\frac{1}{2} g_a^2 (\overline{\phi}_i T_{ij}^a \phi_j)^2$ in Eq. 1.4 for the case where the scalars are two squarks and two Higgs fields. Expanding the relevant components of this term, we have

$$\begin{aligned} \frac{1}{2} g_a^2 (\overline{\phi}_i T_{ij}^a \phi_j)^2 &= \frac{1}{2} g^2 [H_2^{0*} \mathbf{t}_3 H_2^0 + H_1^{0*} \mathbf{t}_3 H_1^0 + \tilde{q}_L^* \mathbf{t}_3 \tilde{q}_L]^2 + ... \\ &\quad + \frac{1}{4} g'^2 [H_2^{0*} y H_2^0 + H_1^{0*} y H_1^0 + \tilde{q}_L^* y \tilde{q}_L - \tilde{q}_R^* y \tilde{q}_R]^2 + ... \end{aligned}$$

The matrix $\mathbf{t}_3$ is the Pauli matrix σ_3 times the weak isospin charge, which depends on particle type. The hypercharge, y, also depends on particle type. The sign of the right-handed term is flipped due to the definition of the covariant derivative for right-handed multiplets [4]. Replacing the Higgs fields with their vacuum expectation values, we have

$$\begin{aligned} \frac{1}{2} g_a^2 (\overline{\phi}_i T_{ij}^a \phi_j)^2 &= \frac{1}{2} g^2 \left[(0, \frac{v_1}{\sqrt{2}}) \begin{pmatrix} \frac{1}{2} & 0 \\ 0 & -\frac{1}{2} \end{pmatrix} \begin{pmatrix} 0 \\ \frac{v_1}{\sqrt{2}} \end{pmatrix} + (\frac{v_2}{\sqrt{2}}, 0) \begin{pmatrix} \frac{1}{2} & 0 \\ 0 & -\frac{1}{2} \end{pmatrix} \begin{pmatrix} \frac{v_2}{\sqrt{2}} \\ 0 \end{pmatrix} \right. \\ &\quad \left. + (\tilde{u}, \tilde{d})_L \begin{pmatrix} \frac{1}{2} & 0 \\ 0 & -\frac{1}{2} \end{pmatrix} \begin{pmatrix} \tilde{u} \\ \tilde{d} \end{pmatrix}_L \right]^2 + ... \\ &\quad + \frac{1}{4} g'^2 \left[\frac{v_2^2}{2} y + \frac{v_1^2}{2} y + \tilde{q}_L^* y \tilde{q}_L - \tilde{q}_R^* y \tilde{q}_R \right]^2 + ... \\ &= \frac{1}{2} g^2 \left[\frac{1}{4} (v_2^2 - v_1^2) + \frac{1}{2} \tilde{u}_L^* \tilde{u}_L \right]^2 + ... \\ &\quad + \frac{1}{4} g'^2 \left[\frac{1}{4} (v_1^2 - v_2^2) + \frac{1}{3} \tilde{u}_L^* \tilde{u}_L - \frac{4}{3} \tilde{u}_R^* \tilde{u}_R \right]^2 + ... \end{aligned}$$

Keeping only terms quadratic in $\tilde{u}$, we have

$$\begin{aligned} \frac{1}{2} g_a^2 (\overline{\phi}_i T_{ij}^a \phi_j)^2 &= \frac{1}{8} g^2 (v_2^2 - v_1^2) \tilde{u}_L^* \tilde{u}_L + ... \\ &\quad - \frac{1}{8} g'^2 (v_2^2 - v_1^2) \left[\frac{1}{3} \tilde{u}_L^* \tilde{u}_L - \frac{4}{3} \tilde{u}_R^* \tilde{u}_R \right] + ... \end{aligned}$$

We can make use of the relations

$$\begin{aligned}
\cos 2\beta &= \frac{v_2^2 - v_1^2}{v_2^2 + v_1^2}, \\
\sin^2\theta_W &= \frac{g'^2}{g^2 + g'^2}, \quad \text{and} \\
M_Z^2 &= \frac{v_1^2 + v_2^2}{4(g^2 + g'^2)},
\end{aligned}$$

to get

$$\begin{aligned}
\frac{1}{2}g_a^2(\overline{\phi}_i T^a_{ij}\phi_j)^2 &= M_Z^2\cos 2\beta\frac{1}{2}(1-\sin^2\theta_W)\tilde{u}_L^*\tilde{u}_L + ... \\
&\quad -\frac{1}{2}M_Z^2\cos 2\beta\sin^2\theta_W\left[\frac{1}{3}\tilde{u}_L^*\tilde{u}_L - \frac{4}{3}\tilde{u}_R^*\tilde{u}_R\right] + ... \\
&= M_Z^2\cos 2\beta(\frac{1}{2} - \frac{2}{3}\sin^2\theta_W)\tilde{u}_L^*\tilde{u}_L \\
&\quad +\frac{2}{3}M_Z^2\cos 2\beta\sin^2\theta_W\tilde{u}_R^*\tilde{u}_R + ...
\end{aligned}$$

The last diagonal matrix element contributions for $\tilde{u}_L$ and $\tilde{u}_R$ are

$$\begin{aligned}
&\text{for } \tilde{u}_L: \quad M_Z^2\cos 2\beta(\frac{1}{2} - \frac{2}{3}\sin^2\theta_W) \quad \text{and} \\
&\text{for } \tilde{u}_R: \quad \frac{2}{3}M_Z^2\cos 2\beta\sin^2\theta_W.
\end{aligned}$$

Off-diagonal contributions come from Eq. 1.7:

$$\begin{aligned}
&\text{for } \tilde{u}_L: \quad A_u G_u H_2^0\tilde{u}_R^* = A_u G_u\frac{v_2}{\sqrt{2}} = A_u m_u \quad \text{and} \\
&\text{for } \tilde{u}_R: \quad A_u G_u H_2^{0*}\tilde{u}_L^* = A_u G_u\frac{v_2}{\sqrt{2}} = A_u m_u.
\end{aligned}$$

Other off-diagonal contributions come from the first term in Eq. 1.6, specifically

$$\begin{aligned}
\left|\frac{\partial V}{\partial H_2}\right|^2 &= \left|G_u\tilde{u}_L\tilde{u}_R^* - \mu H_1^0\right|^2 \\
&= G_u^2|\tilde{u}_L\tilde{u}_R^*|^2 - G_u\mu\tilde{u}_L\tilde{u}_R^*H_1^0 - G_u\mu\tilde{u}_R\tilde{u}_L^*H_1^{0*} + \mu^2(H_1^0)^2.
\end{aligned}$$

Keeping only the terms that are quadratic in the squark fields leaves:

$$\begin{aligned}
&\text{for } \tilde{u}_L: \quad -G_u\mu H_1^0\tilde{u}_R^* = -G_u\mu\frac{v_1}{\sqrt{2}} = -\mu m_u\cot\beta \quad \text{and} \\
&\text{for } \tilde{u}_R: \quad -G_u\mu H_1^{0*}\tilde{u}_L^* = -G_u\mu\frac{v_1}{\sqrt{2}} = -\mu m_u\cot\beta.
\end{aligned}$$

The mass matrix mixing $\tilde{t}_L$ and $\tilde{t}_R$ is

$$\mathcal{M}_{\tilde{t}}^2 = \begin{pmatrix} m_{\tilde{t}_L}^2 + m_t^2 + m_Z^2 \cos 2\beta(\frac{1}{2} - \frac{2}{3}\sin^2\theta_W) & m_t(A_t - \mu\cot\beta) \\ m_t(A_t - \mu\cot\beta) & m_{\tilde{t}_R}^2 + m_t^2 + m_Z^2\cos 2\beta(\frac{2}{3}\sin^2\theta_W) \end{pmatrix}.$$

The mass matrix eigenvalues are

$$\begin{aligned} m_{\tilde{t}_{1,2}}^2 &= \frac{1}{2}(m_{\tilde{t}_L}^2 + m_{\tilde{t}_R}^2) + \frac{1}{4}m_Z^2\cos 2\beta + m_t^2 \\ &\pm \left(\left[\frac{1}{2}(m_{\tilde{t}_L}^2 - m_{\tilde{t}_R}^2) + m_Z^2\cos 2\beta(\frac{1}{4} - \frac{2}{3}\sin^2\theta_W) \right]^2 + m_t^2(A_t - \mu\cot\beta)^2 \right)^{\frac{1}{2}} \end{aligned} \quad (1.8)$$

And the mass eigenstates are

$$\begin{aligned} \tilde{t}_1 &= \cos(\theta_t)\tilde{t}_L - \sin(\theta_t)\tilde{t}_R \\ \tilde{t}_2 &= \sin(\theta_t)\tilde{t}_L + \cos(\theta_t)\tilde{t}_R. \end{aligned}$$

We don't know A_t, μ, or $\cos\beta$, but since the splitting is proportional to the top quark mass (175 GeV/c^2), the splitting between $\tilde{t}_2$ and $\tilde{t}_1$ could be very large. This could make the $\tilde{t}_{1,2}$ splitting the largest of all the squarks forcing $m_{\tilde{t}_1}$ to be the smallest squark mass.

In addition to the large mass splitting, the $m_{\tilde{t}_L}$ and $m_{\tilde{t}_R}$ could be the smallest of all the $m_{\tilde{q}_L}$ and $m_{\tilde{q}_R}$. This is a result of the evolution of the masses from very large energies ($\sim M_{\text{Planck}}$) down to the electroweak scale ($\sim$ 1 TeV) using the Renormalization Group (RG) equations. The RG equations for the (mass)^2 parameters of the third family of squarks are [1]

$$16\pi^2\frac{d}{dt}m_{Q_3}^2 = X_t + X_b - \frac{32}{3}g_3^2|M_3|^2 - 6g_2^2|M_2|^2 - \frac{2}{15}g_1^2|M_1|^2 \quad (1.9)$$

and

$$16\pi^2\frac{d}{dt}m_{\overline{u}_3}^2 = 2X_t - \frac{32}{3}g_3^2|M_3|^2 - \frac{32}{15}g_1^2|M_1|^2 \quad (1.10)$$

where M_3, M_2, and M_1 are the gluino, wino and bino mass parameters at $\sim M_{\text{Planck}}$, g_3, g_2, and g_1 are the gauge couplings at $\sim M_{\text{Planck}}$,

$$X_t = 2|G_t|^2(m_{H_2}^2 + m_{Q_3}^2 + m_{\overline{u}_3}^2) + 2|A_t|^2,$$

and

$$X_b = 2|G_b|^2(m_{H_1}^2 + m_{Q_3}^2 + m_{\overline{d}_3}^2) + 2|A_b|^2.$$

After running the gauge couplings down to the electroweak scale, $g_2 = g$ and $g_1 = \sqrt{5/3}g'$. Also after running, we get the gaugino masses from Eq. 1.7: $M_3 = m_{\tilde{g}}$, $M_2 = m_{\tilde{W}}$, and $M_1 = m_{\tilde{B}}$. Since the top Yukawa coupling ($G_t = \sqrt{2}m_t/v_2$) is much

larger than the other quark Yukawa couplings, X_t is large and has a large effect on the RG equations. Therefore, at the electroweak scale we expect $m^2_{\overline{u}_3} < m^2_{Q_3}$ and that both of these are smaller than the (mass)^2 first two families, for which X_q are negligible. This taken together with the large $\tilde{t}_{1,2}$ mass splitting make $\tilde{t}_1$ the best candidate for the lightest squark and potentially lighter than the top quark.

1.5 $\tilde{t}_1\bar{\tilde{t}}_1$ production

Feynman diagrams illustrating the dominant mechanisms for $\tilde{t}_1\bar{\tilde{t}}_1$ production at the Tevatron[2] are shown in Fig. 1.2. Results from theoretical calculations for the $p\overline{p} \to \tilde{t}_1\bar{\tilde{t}}_1$ production cross section at the Tevatron are plotted in Fig. 1.3. The $\tilde{t}_1\bar{\tilde{t}}_1$ cross section is affected by other SUSY parameters, such as other squark and gluino masses, only in the higher order corrections, so these are not listed in the figure. The production cross section was calculated using the PROSPINO code described in Ref. [7]. Some production cross section values extracted from Fig. 1.3 are listed in Table 1.5. Comparing these cross sections to the top quark production cross section used

Table 1.5: Next-to-leading order theoretical production cross section for $p\overline{p} \to \tilde{t}_1\bar{\tilde{t}}_1$ at the Tevatron [7]. The renormalization scale used in the calculation is $\mu = m_{\tilde{t}_1}$. The parton distribution function used was CTEQ3M.

$m_{\tilde{t}_1}$ [GeV/c^2]	σ_{NLO} [pb]
70	89.2
80	43.7
90	23.0
100	12.8
110	7.46
120	4.51
130	2.81

in Section 3.2, 5.1 pb, we see that we could be sensitive to $\tilde{t}_1\bar{\tilde{t}}_1$ production at the Tevatron for $m_{\tilde{t}_1}$ up to around 120 GeV/c^2.

[2]The Tevatron will be discussed in Section 2.1.

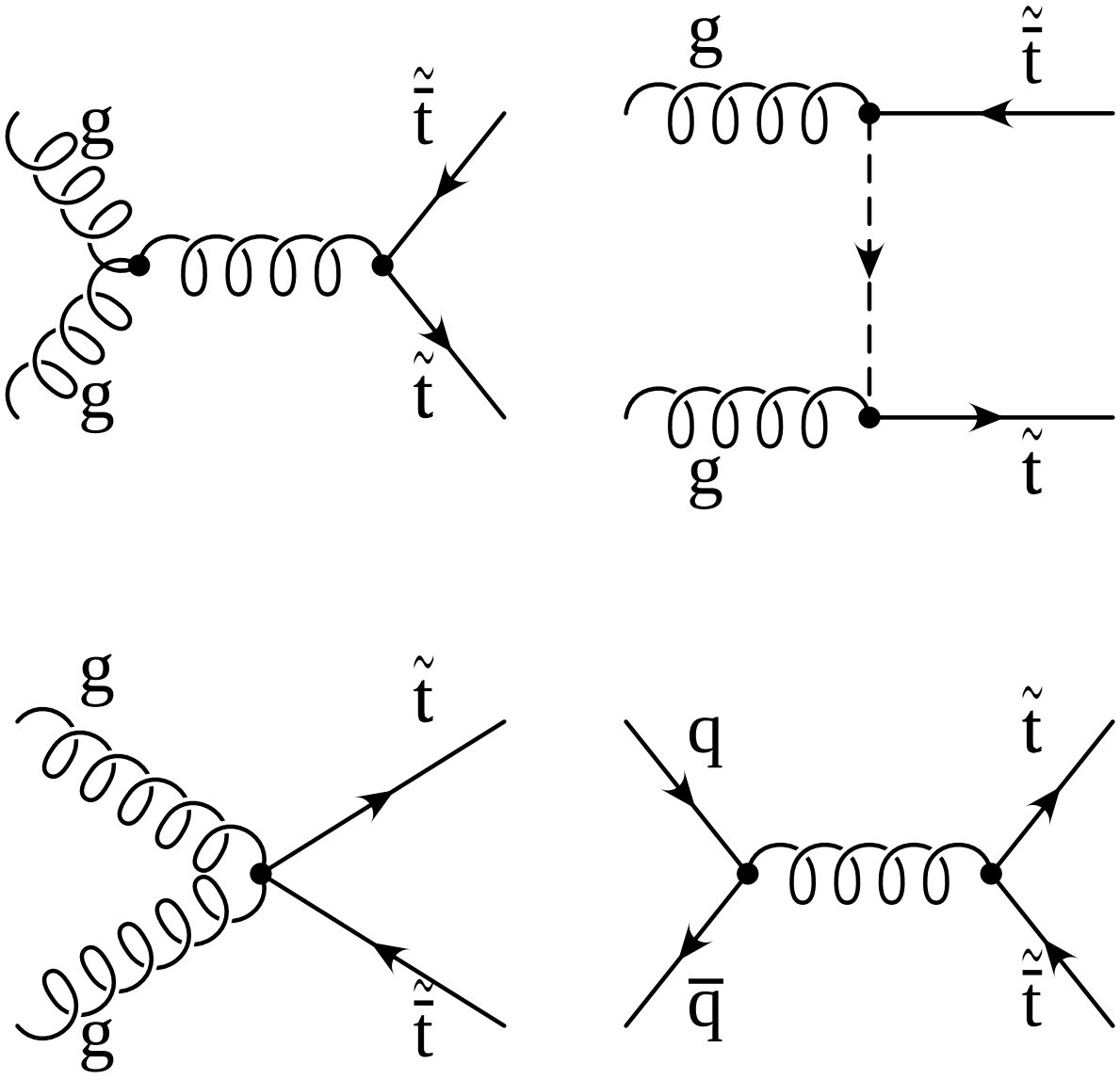

Figure 1.2: Feynman diagrams for the dominant $\tilde{t}_1\bar{\tilde{t}}_1$ production mechanisms at the Tevatron.

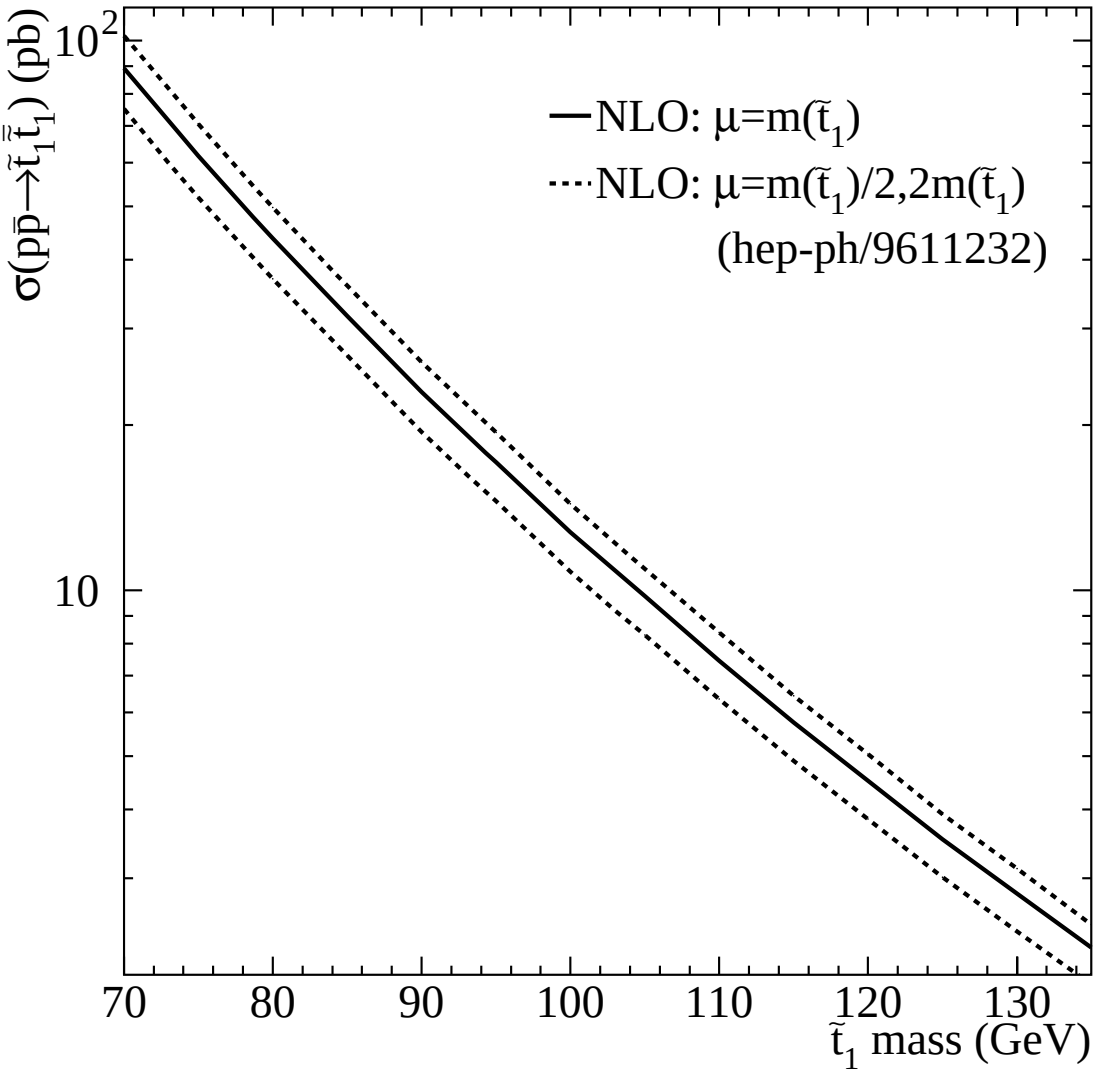

Figure 1.3: Theoretical cross section for $p\overline{p} \to \tilde{t}_1\bar{\tilde{t}}_1$ calculated to next-to-leading order using the PROSPINO code described in Ref. [7]. The renormalization scale used in the calculation is $\mu = m_{\tilde{t}_1}$. The parton distribution function used was CTEQ3M.

1.6 $\tilde{t}_1$ event signature

Having shown that $\tilde{t}_1$ could be lighter than the top quark and that the production cross section for some masses is high enough to be potentially observable at the Tevatron, I will outline ways in which $\tilde{t}_1$ could be observed. First, I must make a couple of statements about the model outlined in Section 1.3. I have mentioned that Eq. 1.5 only contains terms with an even number of superpartners, referred to as R-parity conservation. This implies that there is a lightest supersymmetric particle, LSP, which does not decay. For this to be true, the LSP must have 0 electric charge or it would be easy to detect and we would have already observed it. There are two choices for LSP, the lightest neutralino, $\tilde{\chi}_1^0$, and the sneutrino, $\tilde{\nu}$.

We expect $\tilde{t}_1$ to decay as follows [8]:

- $\tilde{t}_1 \to b\tilde{\chi}_1^{\pm}$,
- $\tilde{t}_1 \to bl\tilde{\nu}$ if $m_{\tilde{t}_1} < m_b + m_{\tilde{\chi}_1^{\pm}}$,
- or $\tilde{t}_1 \to c\tilde{\chi}_1^0$ if $m_{\tilde{t}_1} < m_b + m_{\tilde{\nu}} + m_l$.

Feynman diagrams for these decays are shown in Fig. 1.4. For $m_{\tilde{t}_1} > m_b m_{\tilde{\chi}_1^{\pm}}$, the $\tilde{t}_1 \to b + \tilde{\chi}_1^{\pm}$ decay would proceed with a branching ratio of 100%. For reasons discussed in Ref. [8], the $\tilde{t}_1 \to b\nu\tilde{l}$ decay is greatly supressed compared to $\tilde{t}_1 \to bl\tilde{\nu}$ and is not considered. If this decay is not kinematically allowed, $\tilde{t}_1 \to bl\tilde{\nu}$ would dominate, with an assumed branching ratio of 100%. The $\tilde{t}_1 \to c\tilde{\chi}_1^0$ decay is via loops and is, therefore, supressed. It only proceeds when the first two are not kinematically allowed.

We searched for $\tilde{t}_1\bar{\tilde{t}}_1$ production in the first two decay modes. The third decay was the subject of a separate Tevatron search. In the search for $\tilde{t}_1\bar{\tilde{t}}_1$ from $\tilde{t}_1 \to b\tilde{\chi}_1^{\pm}$, we required one chargino to decay via $\tilde{\chi}_1^+ \to e^+\nu\ \tilde{\chi}_1^0$ or $\mu^+\nu\ \tilde{\chi}_1^0$, where $\tilde{\chi}_1^0$ is the lightest neutralino, with an assumed branching ratio of 11% for each lepton type. In the search for $\tilde{t}_1\bar{\tilde{t}}_1$ from $\tilde{t}_1 \to bl\tilde{\nu}$, the lepton could be an electron, muon, or tau with equal probability. The signature for events from both decay modes is at least one lepton, missing transverse energy from the LSPs and at least 2 jets from the b quark fragmentation and decays.

In the next Chapter, I will describe the Tevatron accelerator and the detector we used for this $\tilde{t}_1\bar{\tilde{t}}_1$ search.

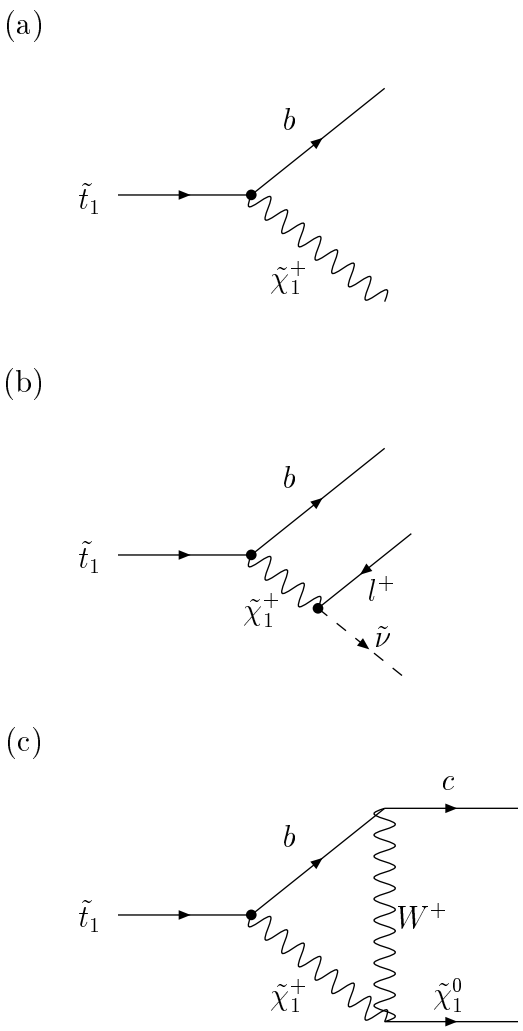

Figure 1.4: Feynman diagram for $\tilde{t}_1$ decays: (a) $\tilde{t}_1 \to b\tilde{\chi}_1^{\pm}$, (b) $\tilde{t}_1 \to bl\tilde{\nu}$, and (c) $\tilde{t}_1 \to c\tilde{\chi}_1^0$. Decay (c) is not considered in this analysis, but is the subject of a separate CDF search.

Chapter 2

The CDF Experiment

This experiment was conducted at the Fermi National Accelerator Laboratory (Fermilab), about 35 miles west of Chicago. The principal accelerator at Fermilab is a superconducting proton-antiproton ($p\bar{p}$) synchrotron and storage ring with a 1 km radius, called the Tevatron.

2.1 Fermilab and the Tevatron

The Tevatron is a superconducting accelerator which collides proton and antiproton beams at a center of mass energy of 1.8 TeV. The proton beam is accelerated in five stages [9]. In the first stage the beam is created and accelerated in the preaccelerator. The proton beam is then passed into the Linac, the Booster, the Main Ring, and finally injected into the Tevatron. The antiproton beam is created from a portion of the proton beam during main ring acceleration. The entire complex is shown in Fig. 2.1.

The proton beam originates as bunches created in the preaccelerator, where electrons are added to H_2 gas to create H^-.[1] The preaccelerator consists of this H^- source, a Cockcroft-Walton generator [10], an electrostatic accelerating column, and a transport line which injects the beam into the Linac. The H^- ions are accelerated to 750 keV in the Cockcroft-Walton generator prior to injection into the Linac.

The Linac is a 150 meter long Alvarez drift-tube accelerator which produces a pulsed 200 MeV beam of H^- [10]. Following this acceleration, the ions drift 46

[1] H^- is used because the object being accelerated by the LINAC must be oppositely charged from the particles in the Booster, the protons. This is due to the design of the injection process which rotates particles clockwise while the Booster rotates particles counter-clockwise.

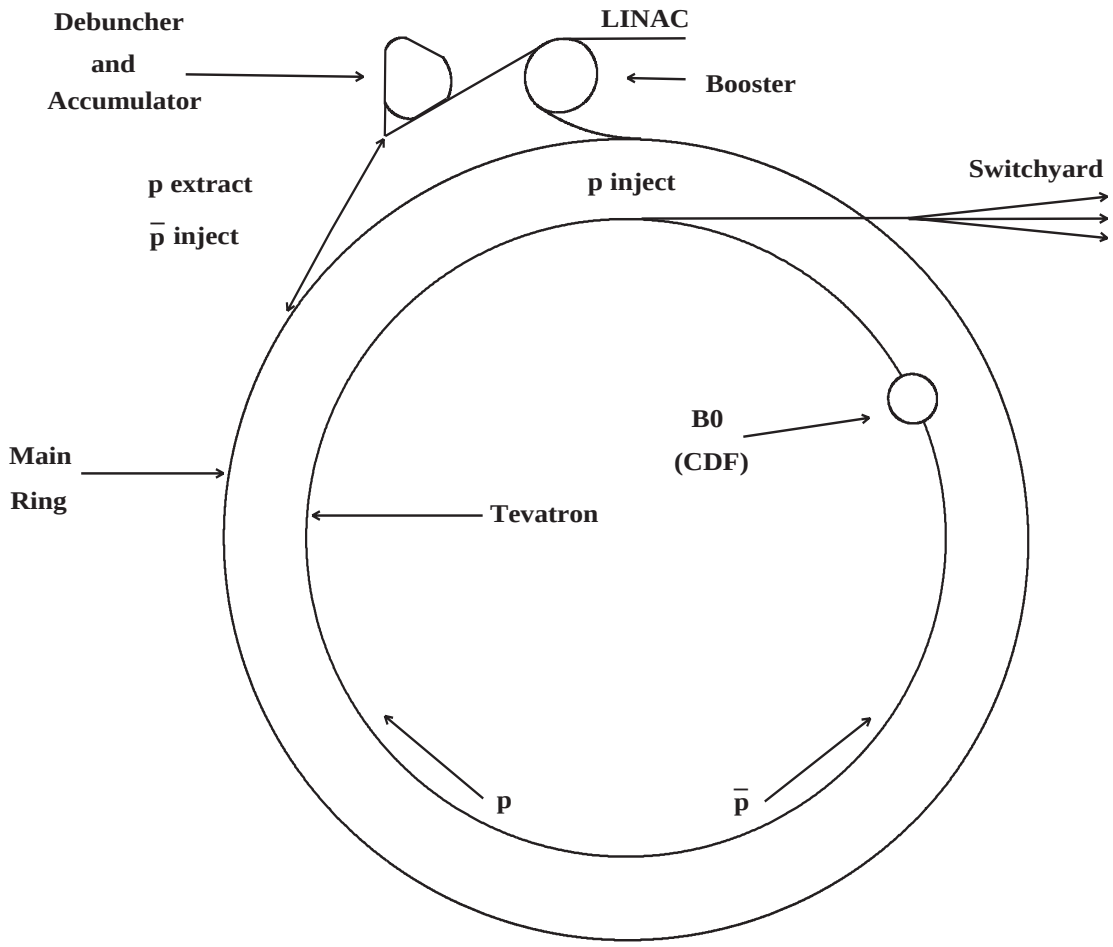

Figure 2.1: Layout of the Fermilab accelerator complex. The preaccelerator and the Cockcroft-Walton generator are not shown, but would appear before the Linac in the figure. The Main Ring and Tevatron are located in the same tunnel.

meters down a transport line to a radio frequency debuncher, which minimizes the momentum spread of ions, before they are injected into the Booster.

The Booster is a 75.5 meter radius fast-cycling synchrotron. In the Booster, the H^- pass through a carbon foil designed to remove the electrons from the H^-. The resulting bare protons are captured by the Booster, while H^- ions and H atoms are directed to a beam dump. The new batch of protons is merged with any beam that is already in the Booster. The Booster fills in six turns with 3×10^{12} protons. Once filled, the carbon foil is removed from the proton path and radio frequency cavities are turned on to accelerate the protons to 8 GeV. The Booster cycle repeats twelve times in rapid succession, loading twelve proton bunches into the Main Ring.

The Main Ring is another, larger synchrotron, with a radius of 1km. It is located in the same tunnel as the Tevatron, and uses conventional magnets to steer the proton beam. It contains a single radio frequency cavity which further accelerates the protons to 150 GeV prior to injection into the Tevatron. For colliding beam operations, the Main Ring is also used to generate 120 GeV protons for antiproton production.

Antiprotons are created from a portion of the proton beam which has been accelerated to 120 GeV in the Main Ring and sent to the Antiproton Source. This proton beam is focused on a tungsten target. Antiprotons are one of the collision products. Using a magnetic field, the antiprotons are selected and sent to the Accumulator where they are stored until enough have been produced. For every million protons sent into the Antiproton Source, about 20 antiprotons are produced. The stack rate for antiprotons is about 4×10^{10} antiprotons per hour. Stacking continues until 10_{12} antiprotons are accumulated. The antiprotons are then sent back into the Main Ring and accelerated to 150 GeV. Since the protons and antiprotons have opposite charge, the same ring can be used to circulate them in opposite directions.

The Main Ring injects the proton and antiproton beams into the Tevatron. The Tevatron is also a fast-cycling synchrotron, but with superconducting magnets to steer the beams. The Tevatron accelerates the beams to 900 GeV each, or 1.8 TeV center-of-mass. In collider mode, six proton and six antiproton bunches revolve in opposite directions in the Tevatron and are collided in two regions with a beam-crossing every 3.5 μs.

The number of collisions, N, occurring in the Tevatron is calculated using

$$N = \sigma \times \int \mathcal{L} dt, \tag{2.1}$$

where $\mathcal{L}$ is the instantaneous luminosity, measured in $\mathrm{cm}^{-2}\mathrm{s}^{-1}$, t is time, and σ is

the cross sectional area, measured in cm^2. With a typical luminosity[2] of $\sim\ 2 \times 10^{31}$ $\mathrm{cm}^{-2}\mathrm{s}^{-1}$, and with a total inelastic cross section of $\sim\ 5 \times 10^{-26}$ cm^2 for $p\overline{p}$ collisions at $\sqrt{s} = 1.8$ TeV, the Tevatron interaction rate is roughly 1 MHz. With a bunch crossing rate of 3.5 μm (286 kHz), this translates in to roughly 3 interactions per crossing.

2.2 The CDF Detector

One of the collision regions of the Tevatron is located inside the Collider Detector at Fermilab (CDF). When a proton and an antiproton collide, any of a number of processes may take place, some of which are described in Section 1.5. The CDF detector allows experimenters to study many types of processes using charged particle tracking, magnetic momentum analysis and calorimetry.

Charged particle tracking and momentum analysis are conducted inside a superconducting solenoid generating a 1.4T magnetic field. The solenoid is surrounded by calorimeters and muon chambers. Fig. 2.2 shows one quarter of the CDF detector. A detailed description of the entire CDF detector is given in Refs. [11] and [12].

Since CDF is a solenoidal detector with forward-backward symmetry, a cylindrical coordinate system centered on the (nominal) interaction point is used to specify direction. The z axis is defined to be the beam axis with the proton direction of motion defining positive z. We define θ to be the polar angle from the z axis and ϕ to be the azimuthal angle measured from the horizontal away from the Tevatron. More often, events are described using using ϕ and pseudorapidity, η, defined as

$$\eta \equiv -\ln\ \tan(\frac{\theta}{2}).$$

Using η is convenient when describing particles with $p \gg m$ because boosts along z can be handled more simply. For a boost along z of velocity β, $\eta \rightarrow \eta + \tanh^{-1}\beta$ [13]. The coordinates η and z are shown in Fig. 2.2.

In a $p\bar{p}$ collision, the proton and antiproton constituents are what actually interact. Although these constituents travel more or less along the beamline, we do not know their momentum fraction for each collision, hence we do not know the total momentum of the collision. Instead, we use as conserved quantities the momenta and energy of particles transverse to the beam. We define the transverse momentum (p_T) and transverse energy (E_T) by

$$\begin{aligned} E_T &= E \times \sin\theta, \\ p_T &= p \times \sin\theta. \end{aligned}$$

[2]Section 2.3.2 describes the luminosity measurement.

Figure 2.2: Schematic picture of one quarter of the CDF detector for Run I, 1992-1996. The position and size of the forward calorimeter is not to scale, but it has been included to illustrate the full CDF pseudorapidity range. The central electron shower-maximum detector is labeled "CES". The central pre-radiator is labeled "CPR".

Another useful quantity is the missing transverse energy, $\not\!\!E_T$. It is defined as the negative of the vector sum of the E_T in an event. See Section 2.4.4 for a more complete treatment. In an ideal detector, without cracks and energy mismeasurement, $\not\!\!E_T$ represents energy carried away by neutral particles, such as neutrinos.

The detector components relevant to this analysis are

- the Silicon Vertex Detector (SVX),
- the central tracking chamber (CTC),
- the central muon detector (CMU),
- the central muon detector upgrade (CMP),
- the central muon detector extension (CMX),
- the central electromagnetic (CEM), and central hadronic (CHA) calorimeters.

These components are shown in Fig. 2.2. I will briefly describe each.

2.2.1 The Silicon Vertex Detector

The innermost tracking subsystem and the component of the CDF detector closest to the beam pipe is the Silicon Vertex Detector. The SVX provides approximately 10 μm resolution tracking in the plane transverse to the beam. The SVX consists of two identical electrical/mechanical units called barrels, one on either side of the beam and centered on $z = 0$. The total active length of the SVX is 51 cm. However, the true interaction point is described by a Gaussian centered on $z = 0$ with $\sigma = 30$ cm, which reduces SVX acceptance to about 60%.

A schematic of one barrel is shown in Fig. 2.3. Each barrel consists of four concentric layers; the radius of the first layer is 2.86 cm from the beam and radius the fourth layer is 7.87 cm from the beam. Each layer consists of silicon microstrip sensors bonded in groups of three along the length of the barrel. Each group of three is referred to as a ladder. Each layer is composed of twelve ladders surrounding the beamline. The silicon microstrip sensor $r - \phi$ readout pitch is 60 μm for the first three layers and 55 μm for the last layer.

A key role of the precision SVX tracking is to reconstruct vertices displaced from the primary interaction. These secondary vertices are a signature of decays of b and c quarks.

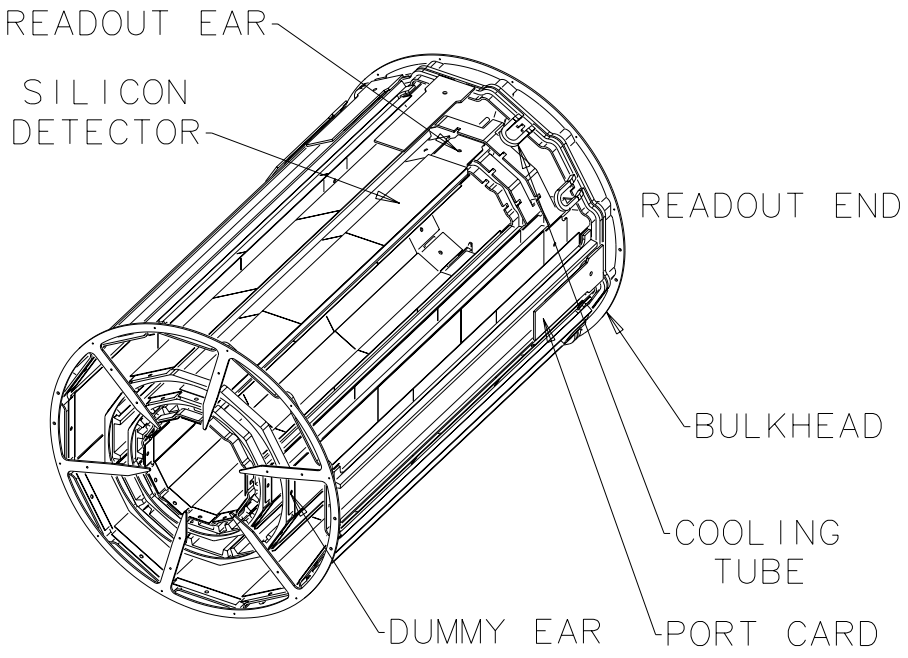

Figure 2.3: Schematic view of one SVX barrel.

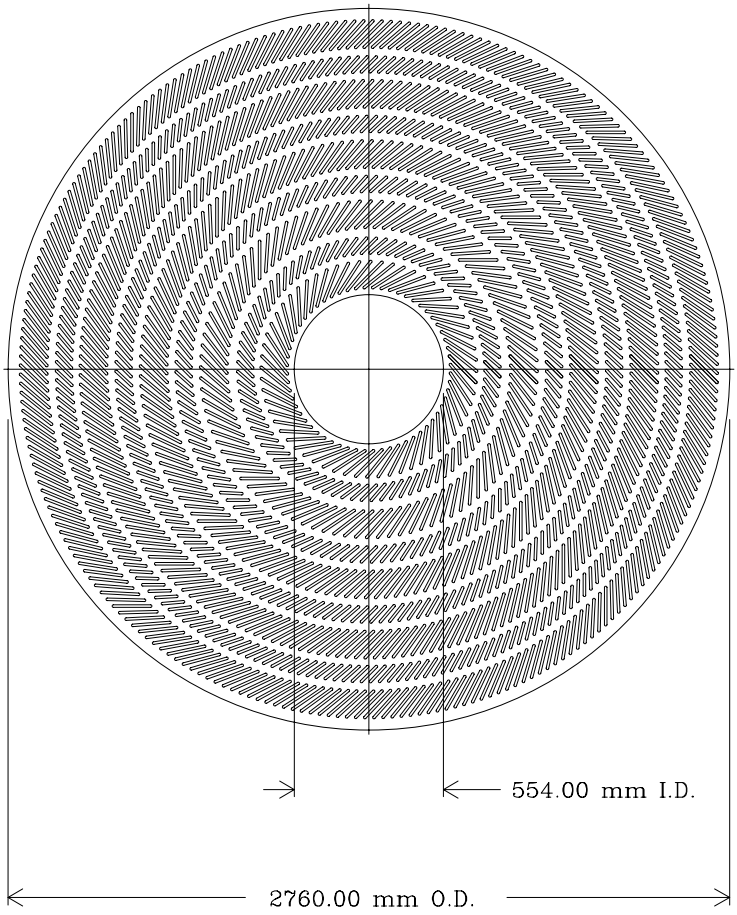

Figure 2.4: An end plate of the Central Tracking Chamber. The nine superlayers shown are the groupings of axial and stereo sense wires.

2.2.2 The Central Tracking Chamber

The momenta of charged particles are measured in the second tracking subsystem, the central tracking chamber (CTC), just outside of the SVX but within the solenoid. The CTC is a 3.2 m long cylindrical drift chamber with 84 layers of sense wires grouped in to nine superlayers. The inner radius of the CTC is 31 cm and the outer radius is 132 cm. This corresponds to a region of coverage of $|\eta| < 1.0$. The sense wires are grouped in to 5 axial superlayers alternating with 4 small angle stereo superlayers inside an argon-ethane-ethanol gas mixture (49.6/49.6/0.8%).

The CDF tracking algorithm begins by reconstructing charged particle tracks in the r-ϕ plane using information from the axial superlayers. The z position of the

primary vertex is used as a seed for the stereo track reconstruction, the z position of a track. The CTC wire resolution is about 200 μm and the two track resolution is about 5 mm. This translates into a beam constrained momentum resolution of better than $\delta p_T/p_T = 0.002 \times p_T$ for isolated, high p_T tracks. Tracks found in the CTC are combined with SVX information by projection roads, when possible, improving resolution to $\delta p_T/p_T = 0.001 \times p_T$.

2.2.3 The Central Calorimeters

Electromagnetic and hadronic calorimeters surround the solenoid and are used to identify electrons and jets[3]. Particles with $p_T > 350$ MeV/c^2 will be able to penetrate the magnetic field and be detected in the calorimetry. The central calorimeters are divided azimuthally into 24 wedges, each covering 15 degrees in ϕ. Each wedge is composed of towers which cover $\Delta\eta$ =0.1. Each tower in the CHA is directly behind and associated with a tower in the CEM. The tower segmentation and coverage is shown in Fig. 2.5. The inner radius of the CEM is 173 cm and extends to the inner radius of the CHA, 208 cm. They are about 500 cm long, centered on $z = 0$.

We use electrons identified in the CEM which covers the region $|\eta|$ <1.1. The CEM uses 31 layers of 3.2 mm lead sheets alternated with 5 mm sheets of plastic scintillator. Each CEM tower is readout by two photomultiplier tubes, one at each end. The energy resolution is

$$\frac{\Delta E}{E} = \left[\left(\frac{13.5\%}{\sqrt{E_T}} \right)^2 + (2\%)^2 \right]^{1/2} .$$

The CEM contains a set of proportional strip and wire chambers called the central electron shower-maximum detector or CES. As the name suggests, it is located at the depth where an electromagnetic shower deposits its maximum energy. The strips provide the z location of the shower and the wires provide the $r-\phi$ information. The resolution for both is 2 mm.

The CHA uses 32 layers of 25 mm steel plates alternated with 10 mm of plastic scintillator in its central region, where coverage is $|\eta|$ <0.9. There is an additional endwall component which we will include as part of the CHA, which covers 0.9 < $|\eta|$ <1.3. The endwall component uses 15 layers of 51 mm steel plates alternated with 10 mm of plastic scintillator. The CHA energy resolution is

$$\frac{\Delta E}{E} = \left[\left(\frac{75\%}{\sqrt{E_T}} \right)^2 + (3\%)^2 \right]^{1/2}$$

[3]A jet is a collection of tracks originating from the same vertex and being associated in $\eta - \phi$ space, such as from the fragmentation of a quark or gluon.

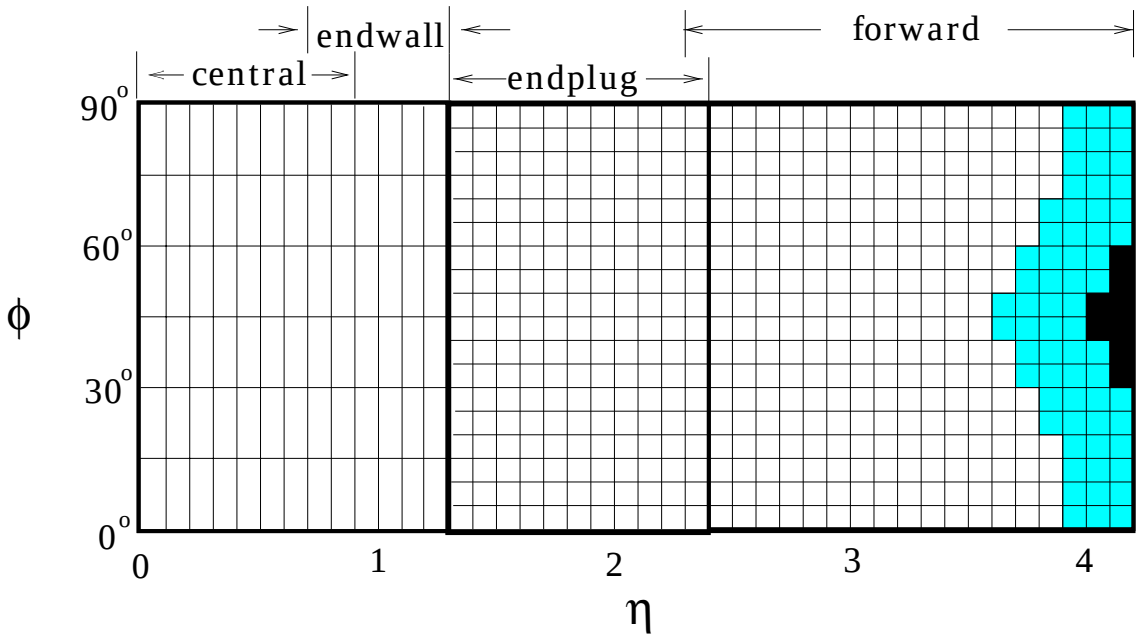

Figure 2.5: The $\eta - \phi$ segmentation of the calorimeters in the CDF detector. The central region is $|\eta| < 1.1$ where the calorimeters are segmented $(\Delta\eta = 0.1) \times (\Delta\phi = 15°)$. The Endplug region is $1.1 < |\eta| < 2.4$ and is segmented $(\Delta\eta = 0.1) \times (\Delta\phi = 5°)$. The Forward region is $2.4 < |\eta| < 4.4$ and is also segmented $(\Delta\eta = 0.1) \times (\Delta\phi = 5°)$. The shaded area in the Forward region is where there is only electromagnetic coverage, and the black area has no coverage at all (due to the presence of Tevatron steering magnets).

for isolated pions.

2.2.4 The End Plug Electromagnetic Calorimeter

We use an additional calorimeter component, the end plug electromagnetic calorimeter (PEM), to increase our jet acceptance. The PEM covers the region $1.3 \leq |\eta| \leq 2.4$. As shown in Fig. 2.5, the PEM has the same η segmentation as the CEM ($\Delta\eta = 0.1$), but finer segmentation in ϕ ($\Delta\phi = 5^\circ$). The PEM is composed of a multi-wire gas (argon-ethane) proportional system with 34 tube arrays interleaved with 2.7 mm thick steel absorbers. This gives the PEM a thickness of about 19 radiation lengths.

2.2.5 The Central Muon Detectors

Muons are identified by tracks in drift chambers in two detector subcomponents outside the calorimeters, the CMU and the CMP. The first muon subsystem, the CMU, is located behind the calorimeters, which constitute five absorption lengths of material. A muon must have $p_T > 1.4$ GeV/c to penetrate through to the CMU. The CMU consists of four layers of drift chambers, shown in Fig. 2.6, and covers the region $|\eta| < 0.6$. The chambers shown in Fig. 2.6 measure four points along a muon's trajectory in z and ϕ. The ϕ measurement is made using the drift chamber time-to-distance relationship. The z component is measured using charge division. The accuracy per point of the ϕ measurement is 250 μm and that of the z measurement is 1.2 mm. The CMP is located behind 0.6 m of steel which provides an additional three absorption lengths of material. The CMP also consists of four layers of drift chambers. Approximately 84% of the detector is covered by the CMU, 63% by the CMP, and 53% by both. A muon must have $p_T > 2.3$ GeV/c to penetrate through to the CMP [14]. We primarily use muons which have hits in both the CMU and CMP. This reduces the chance that pions which have punched through the CHA will be identified as muons. The muon purity from CMU muons with CMP confirmation is $\sim 95\%$.

A third muon detector subcomponent is the central muon extension (CMX) which was added to provide additional muon identification in the region $0.6 < |\eta| < 1.0$. The CMX consists of four free-standing conical arches on either side of the central region. Each arch contains four layers drift chambers in between scintillator counters used for triggering. A muon must have $p_T > 1.4$ GeV/c to penetrate through to the CMX. The combined $\eta - \phi$ coverage of the the CMU, CMP, and CMX is shown in Fig. 2.7. The CMX only covers about 71% of the solid angle in $0.6 < |\eta| < 1.0$ due to obstacles.

In the CMU, CMP, and CMX, muons must have hits in three separate layers

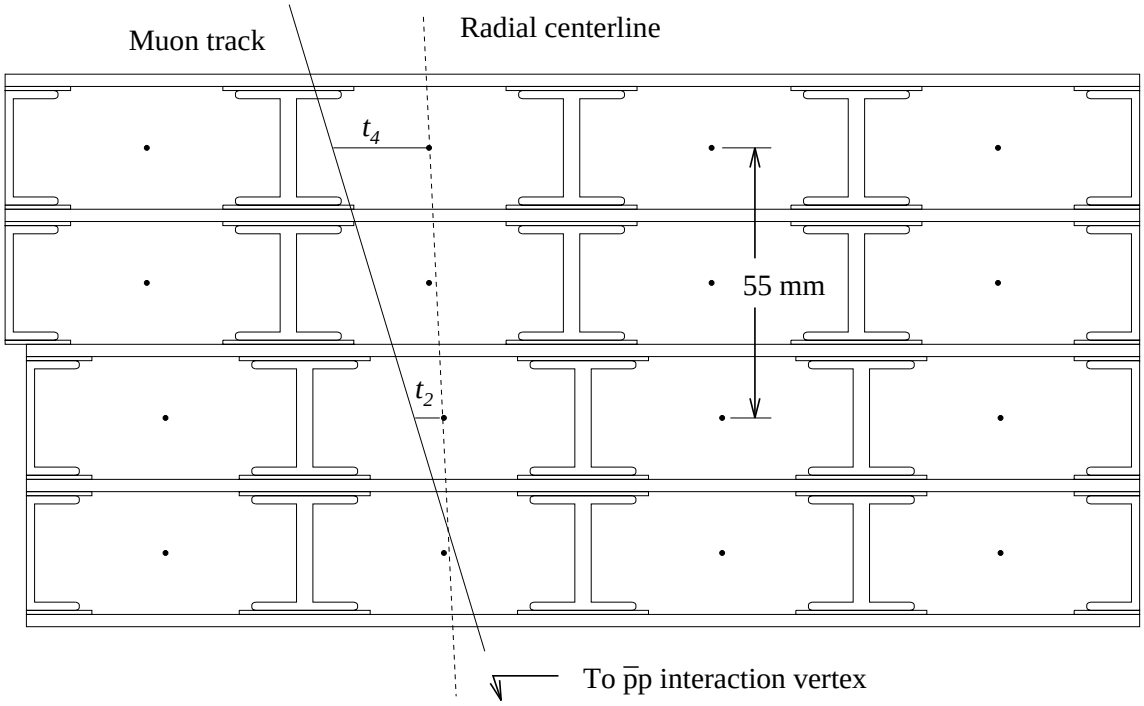

Figure 2.6: The CDF central muon detector shown in the $r - \phi$ plane. The detector consists of the four layers of drift chambers shown. The drift times t_2 and t_4 are used to compute muon momentum for triggering.

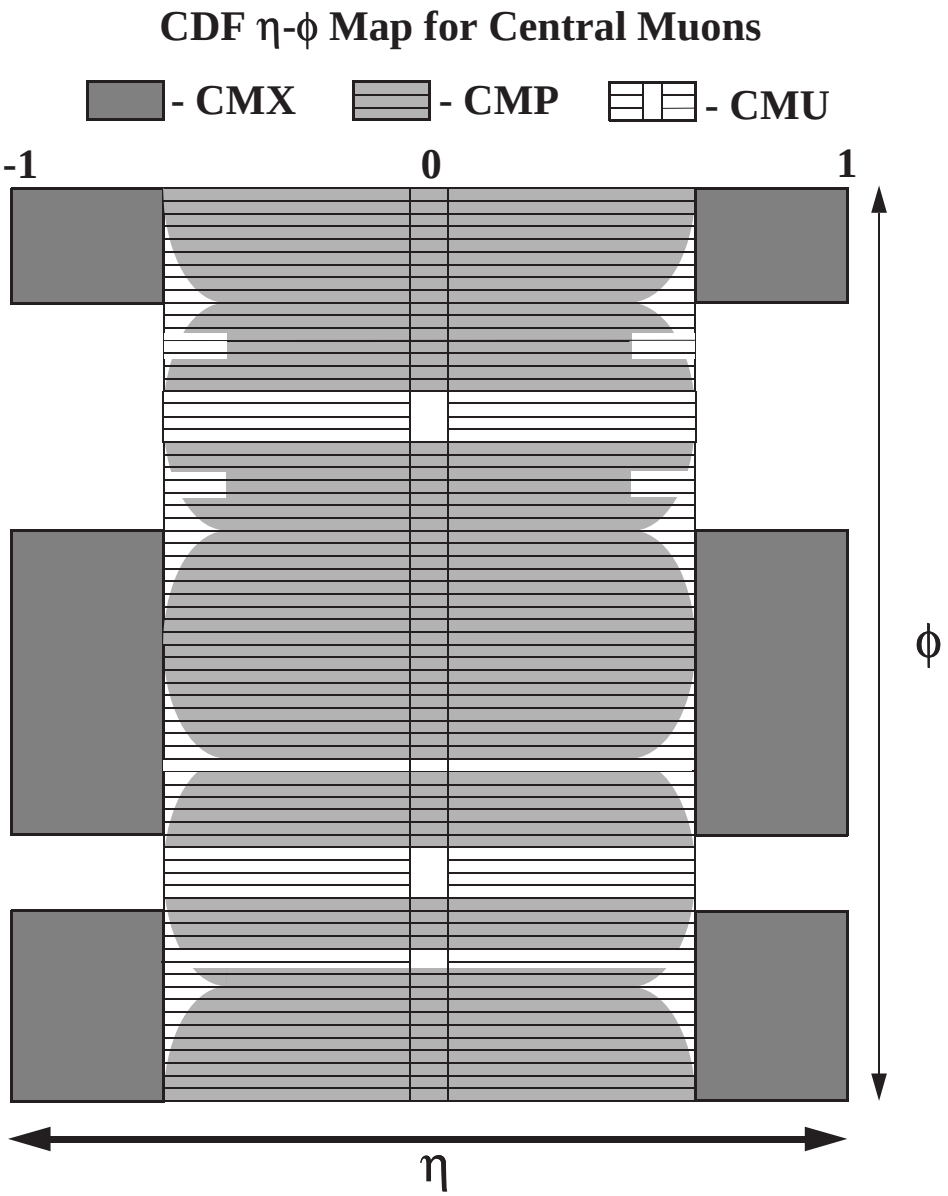

Figure 2.7: The CDF central muon $\eta - \phi$ coverage. The ϕ gaps in the CMX coverage occur where the CMX intersects the floor (large gap) and the Tevatron (small gap).

to be identified. These hits must be aligned to within detector resolution in the $r-\phi$ and $r-z$ planes. These segments are then merged to form a three dimensional track stub.

2.3 Data Taking

The CDF detector sees many more collisions than could possibly be recorded and the interesting, high Q^2 events are a small fraction of the total. Therefore, selection criteria are applied before data is stored to tape. These selection criteria are included in a set of hardware and software filters called triggers.

2.3.1 Triggers

CDF uses a three level trigger system. Each level has various trigger paths to accommodate varying physics interests. For example, there are muon triggers for use in b quark physics and $\not\!\!E_T$triggers for use in supersymmetry searches, etc. The first trigger, referred to as Level 1, relies on fast, analog output from detector preamplifiers to decide whether to keep an event for further processing and selection. The detector preamplifiers send output to the trigger logic and also hold data until the decision is made. This analog decision process takes less than 3.5 μs, which is the time between beam crossings. At an average instantaneous luminosity of 10×10^{30} cm^{-2}s^{-1}, the Level 1 trigger rate is about 1 kHz (see Table 2.1.)

Table 2.1: CDF level 1, 2, and 3 trigger accept rates and dead times at an instantaneous luminosity of 10×10^{30} cm^{-2}s^{-1}. This table is taken from Ref. [15].

Trigger Level	Accept Rate	Dead Time
Level 1	1 kHz	0%
Level 2	20 Hz	4%
Level 3	5 Hz	10%

The second step, the Level 2 trigger, is a digital hardware trigger. This trigger looks at calorimeter clusters, fast timing information from the CTC, and CTC track matches to tracks in the muon chambers. The time required for Level 2 processing depends on the complexity of the event. Most simple events can be analyzed in 20 - 30 μs, but for events with a large number of calorimeter clusters and tracks, the event may take an order of magnitude longer.

The last trigger, Level 3, is a software trigger run on six Silicon Graphics Power Servers, each with eight RS4000 CPUs. At Level 3, electron and muon candidates

have been fully constructed, jets have been clustered, and $\not\!\!E_T$ has been computed. This allows the various Level 3 triggers to accommodate the diverse physics interests of the CDF users. The Level 3 triggers are fed into various data streams according to physics interest. For example, high p_T electron and muon triggers were processed for use in the top quark discovery. Low p_T muon triggers, in which two muons are required, are used to reconstruct $J\psi$ particles for bottom quark physics. The $\not\!\!E_T$ trigger is often used for supersymmetry searches. We used data from two streams for this analysis. One was for low p_T, central electrons, called ECLB, and was primarily acquired using the Level 3 triggers ELEB_CEM_8_6 and ELEB_CEM_8. These two triggers accept an event with at least one electron reconstructed in the CEM with E_T $\geq$8 GeV. ELEB_CEM_8_6 also requires the electron to have CTC reconstructed p_T $\geq$7.5 GeV/c. The second data stream used for this analysis was for low p_T, central muons, called MULB, and was primarily acquired using the Level 3 triggers MUOB_CMU_CMP_8 and MUOB_CMX_8. These two triggers accept an event with at least one muon with p_T $\geq$8 GeV/c in the CMU with CMP confirmation and in the CMX, respectively.

2.3.2 Luminosity measurement

Luminosity is measured using the Beam Beam Counter (BBC), which is two sets of scintillator panels on either side of the CDF $p\overline{p}$ collision region. The instantaneous luminosity of a $p\overline{p}$ collider is given by

$$\mathcal{L} = \frac{N_p N_{\bar{p}} N_B f}{4\pi\sigma^2}, \tag{2.2}$$

where N_p and $N_{\bar{p}}$ are the numbers of protons and antiprotons per bunch, N_B is the number of bunches of each type (6), $f(\approx 50$ kHz) is the revolution frequency, and σ^2 is the RMS cross sectional area of a bunch. A typical instantaneous luminosities for Run IB was 1.6×10^{31} cm^{-2}s^{-1}. The highest instantaneous luminosity for Run IB was 2.8×10^{31} cm^{-2}s^{-1}. When integrating the luminosity over time for use in Eq. 2.1, events with potentially corrupted data were omitted. Events in which only data from specific, non-critical detector subcomponents were corrupted, were still classified as good for the other detector subcomponents. This led to trigger path specific integrated luminosities. The luminosity integrated over time for ECLB is 88.59 ± 3.63 pb^{-1}. The integrated luminosity for MULB is 87.43 ± 3.58 pb^{-1}.

2.4 The CDF data structure

The Level 3 trigger processing identifies physics objects such as muon candidates, electron candidates, jets, and $\not\!\!E_T$. The information from the relevant detector sub-

components used to describe these objects is stored in persistent data structures called banks. I will describe the banks relevant to this analysis in more detail.

2.4.1 CMUO bank

A muon track stub in the CMU, CMP, or CMX drift chambers is matched to a track that has been extrapolated from the CTC. For CMU matching, the candidate CTC track must also match the muon stub to within ± 50 cm in z. The magnetic field in the calorimetry and multiple scattering are taken into account during extrapolation. This is used to reconstruct a muon object. The muon detector subcomponent, track momentum, and the quality of the CTC and muon detector track match are recorded in the muon object bank, labeled CMUO. The CMUO bank also contains the energy the muon deposited in the calorimetry along its trajectory, the CTC track parameters, and momentum errors. There is a CMUO bank for each muon candidate.

2.4.2 JETS bank

In a grouping of calorimeter towers with hits, those calorimeter towers with the largest energy deposited are used as seed towers for calorimeter clusters. Tower energy must be least 1 GeV to be used in clustering. We define a cone in η and ϕ as $R \equiv \sqrt{\eta^2 + \phi^2}$. Towers must be within a cone of fixed radius (R= 0.4, 0.7, or 1.0) about the seed tower to be considered in clustering. The algorithm used to cluster jets within a specified cone size is given in Ref. [16]. We use $R = 0.7$ for this analysis. If two clusters overlap, sharing at least 75% of their energy, these clusters are merged. Tower clusters are combined with corresponding CTC tracks to identify jets. Information for each jet is stored in a separate JETS bank.

The information found in the JETS bank includes number of tracks, CEM and CHA energy fractions, total energy, and reconstructed four momentum. To reconstruct four momentum, the jet η must be determined. The reconstructed primary vertex is used to determine the cluster *event* η. The cluster *detector* η is defined from $z = 0$. Both event η and detector η are included in the JETS bank.

2.4.3 ELES bank

Electrons (and photons[4]), like jets, are identified by calorimeter tower clusters. Unlike jets, the minimum energy of an electron seed tower is 3 GeV. Also, only the two towers on either side of the seed are included in the cluster. If the seed tower lies adjacent

[4]Photons are clustered in the same manner as electrons and are also stored in ELES banks. They differ from electrons in that they have no CTC track pointing to the calorimeter cluster.

to the calorimeter crack at $\eta = 0$, the tower on the other side of the crack is not used. The cluster must have a minimum E_T of 5 GeV. To improve electron identification, the ratio of the CHA energy to the CEM energy must be less than 0.125. The tower clusters are matched to extrapolated CTC tracks.

Information for each electron candidate is stored in a separate ELES bank. Bank information includes electron CEM energy, CHA energy in the corresponding tower, E_T in towers adjacent to the electron cluster, number of tracks pointing to the cluster, and four momentum and charge of the highest p_T track pointing to the cluster.

2.4.4 METS bank

The missing transverse energy, $\not\!\!E_T$, in an event is defined as the negative of the vector sum of E_T for all calorimeter towers above threshold with $|\eta| < 3.6$:

$$\vec{\not\!\!E}_T = -\sum_i \vec{E}_T^i,$$

where E_T^i is the transverse energy of the ith tower. The threshold is 0.1 GeV in the central calorimeters, but larger in the plug and forward regions. The resolution of $\not\!\!E_T$ is approximately $0.7\sqrt{\sum E_T}$, where $\sum E_T$ is the scalar sum of the transverse energy of an event (including $\not\!\!E_T$).

The $\not\!\!E_T$, total calorimeter energy, and total calorimeter E_T, among other things, are stored in the METS bank. There is one METS bank per event.

Chapter 3

Event Simulation

In this analysis, like all analyses conducted at multipurpose, high energy physics experiments, the offline analysis proceeds by taking the data collected by the triggers and apply some selection criteria to enhance the signal events with respect to background. To do this requires knowledge of the statistical behavior of signal and background events. We gain this knowledge using computer simulations of these physics processes from $p\overline{p}$ collisions. Large numbers (of order 10^4) of events of each process type are simulated to determine the best selection criteria from their resulting signal to background ratio.

Before we began our study of signal selection criteria, we first decided which background processes were relevant. Starting with the $\tilde{t}_1$ decay signature described in Section 1.6 (a lepton, $\not\!\!E_T$, and at least 2 b quark jets), we determined what Standard Model processes we expected to have this same signature. These processes are top and bottom quark production, and $Wb\overline{b}$ production. In addition, other Standard Model processes can mimic this signal by having mismeasured transverse energy which gives rise to $\not\!\!E_T$. The simulations used to determine the amounts of signal and these background processes in our 88 pb^{-1} of data were performed by a Monte Carlo technique. CDF Monte Carlos are performed in two steps.

In the first step, physics events are generated according to known production mechanisms. Initially, a hard scattering is generated according to the appropriate QCD cross section with parton momentum fractions given by some parton distribution function. Radiative corrections are added to the initial and final states. Then Bare quarks are fragmented according to various theoretical models. And finally, short-lived particles are decayed according to measured or calculated branching ratios. Particle types and momenta are recorded for use in the second step. This part of the simulation can be done with a variety of software packages developed by the particle physics community. Different packages are better at simulating different

physics processes. I will list the specific packages that we used in Sections 3.1.2 and 3.2.

In the second step, the particle momenta are used to propagate the particles through a simulated CDF detector. There are two CDF detector simulation packages available. One, CDFSIM, creates raw detector data from the propagated tracks. This is useful for testing event reconstruction software, but is too time consuming for most CDF analyses. The faster yet very reliable alternative is QFL′. This software doesn't produce raw data, but higher level detector component data, which would have been produced for real data after some event reconstruction had been performed. The simulated data is smeared from the generator level input values according to measured detector resolutions.

After this, the simulated events are ready for the offline reconstruction. We can run the same offline reconstruction modules on the simulated data as on real data. These produce the data structures described in Section 2.4.

We simulated large numbers of events for both $\tilde{t}_1 \to b\tilde{\chi}_1^{\pm}$ and $\tilde{t}_1 \to bl\tilde{\nu}$ signals and backgrounds. From these we determined the detector acceptance, the trigger efficiencies, and the efficiencies of our signal selection criteria, which will be discussed in Chapter 4.

3.1 Modeling the signal

The choice of Monte Carlo generator used for simulating supersymmetry is briefly discussed in this section. Since no supersymmetric particle masses have been measured, these must be entered into the Monte Carlo. Some supersymmetric particle mass limits have been set by previous searches. These motivate our choices of input masses, which we describe in this section as well.

3.1.1 Experimental limits on superpartner masses

Although the $p\overline{p} \to \tilde{t}_1\bar{\tilde{t}}_1$ production cross section is insensitive to other supersymmetric parameters and particle masses, as mentioned in Section 1.5, the cross sections measured in this analysis are still a function of $\tilde{t}_1$ mass and the masses of the $\tilde{t}_1$ daughters. This is because these masses affect geometrical acceptance and selection cut efficiencies used to calculate the cross section. A review of the current 95% confidence level (C.L.) lower limits on mass of the daughter particles, $\tilde{\chi}_1^{\pm}$, $\tilde{\chi}_1^0$, and $\tilde{\nu}$, is given in this section in order to motivate the our choices of masses input into the Monte Carlo generator.

Lower limits on $m_{\tilde{\chi}_1^\pm}$ and $m_{\tilde{\chi}_1^0}$

Results published from the measurements of $m_{\tilde{\chi}_1^\pm}$ and $m_{\tilde{\chi}_1^0}$ are model dependent. Although most measurements are made in the framework of the MSSM, differences arise in the choice of the LSP, R parity violation, massiveness of sleptons, degeneracy of the squark masses, and sensitivity to regions of μ and $\tan\beta$. Significant model differences can make a particular measurement inapplicable to this analysis. It is for this reason that we do not use the result from another Tevatron experiment, DØ , in which the gravitino is considered the LSP. The models used in the CDF and LEP measurements are consistent with that outlined in Chapter 1 and are presented here. However, even these results explore different regions of parameter space (μ, $\tan\beta$, and other squark masses) such that one can not be considered as superseding the other.

The current $m_{\tilde{\chi}_1^\pm}$ and $m_{\tilde{\chi}_1^0}$ lower limits determined by CDF[18] at the 95% C.L. are shown in Table 3.1. The limits are listed as a function of μ and $\tan\beta$, defined in Chapter 1, and the assumed degenerate gluino masses and degenerate squark masses. These limits were calculated for a Supergravity-inspired MSSM, discussed in Ref. [6]. The distinctive feature of the Supergravity-inspired MSSM is that $m_{\tilde{l}}$ and $m_{\tilde{\nu}}$ are related through the Renormalization Group Equations to $m_{\tilde{q}}$ and $m_{\tilde{g}}$, reducing the number of free parameters.

Table 3.1: Current CDF lower limits on $m_{\tilde{\chi}_1^\pm}$ and $m_{\tilde{\chi}_1^0}$ at the 95% C.L. as a function of μ, $\tan\beta$, and the assumed degenerate gluino and squark masses[18, 6]. These limits were calculated for a Supergravity-inspired MSSM, discussed in Ref. [6]. All masses are in units of GeV/c^2.

Input Parameters				Mass Limits	
μ	$\tan\beta$	$m_{\tilde{q}}$	$m_{\tilde{g}}$	$m_{\tilde{\chi}_1^\pm}$	$m_{\tilde{\chi}_1^0}$
-200	2	200	200	72.5	30.7
-400	2	330	220	68.0	29.2
-400	2	364	220	71.0	32.0
-400	2	240	240	76.5	36.1
-400	2	500	200	58.0	26.4
-600	2	260	260	81.5	38.1
-800	2	270	270	81.0	39.3
-1000	2	260	260	78.5	37.5

The current $m_{\tilde{\chi}_1^\pm}$ and $m_{\tilde{\chi}_1^0}$ lower limits determined by OPAL[19] at the 95% C.L. are shown in Table 3.2 as a function of $\tan\beta$ and m_0, the common sfermion mass

at the GUT scale. These limits were calculated using a constrained MSSM and are only valid if $m_{\tilde{\chi}_1^\pm} - m_{\tilde{\chi}_1^0} \geq$10 GeV/c^2 and $m_{\tilde{\chi}_2^0} - m_{\tilde{\chi}_1^0} \geq$10 GeV/c^2. The details of this constrained MSSM are given in reference [19], but the main feature appears to be degenerate sfermion masses and degenerate gaugino masses at the GUT scale.

Table 3.2: Current OPAL lower limits on $m_{\tilde{\chi}_1^\pm}$ and $m_{\tilde{\chi}_1^0}$ at the 95% C.L. as a function of $\tan\beta$ and m_0, the common sfermion mass at the GUT scale [19]. The term "lightest" refers to the lightest possible value of m_0 given current OPAL limits on $m_{\tilde{\nu}}$ and $m_{\tilde{l}}$ [19]. All masses are in units of GeV/c^2.

Input Parameters		Mass Limits	
$\tan\beta$	m_0	$m_{\tilde{\chi}_1^\pm}$	$m_{\tilde{\chi}_1^0}$
1.0	lightest	65.7	13.3
1.0	1,000	84.5	24.7
1.5	lightest	72.1	23.9
1.5	1,000	85.0	34.6
35	lightest	74.4	40.9
35	1,000	85.1	43.8

The ALEPH collaboration reports their least restrictive $m_{\tilde{\chi}_1^0}$ lower limit at 29.8 GeV/c^2 for low $\tan\beta$ and $m_0 = 200$ GeV/c^2 [20]. This limit increases with $\tan\beta$, plateauing at 46 GeV/c^2. Limits also increase with m_0, but these values were not reported. ALEPH uses the same MSSM model as OPAL where sensitivity is significant for $m_{\tilde{\chi}_1^\pm} - m_{\tilde{\chi}_1^0} \geq$10 GeV/c^2. Results for the limit of $m_{\tilde{\chi}_1^\pm}$ are reported for $\tan\beta = \sqrt{2}$ where higher values tend to give higher limits. For $\mu \leq -100$ or $\mu \geq 200$ GeV/c^2 and $m_0 = 200$ GeV/c^2, $m_{\tilde{\chi}_1^\pm} > 91$ GeV/c^2 at the 95% C.L.

The L3 collaboration reports a limit for $m_{\tilde{\chi}_1^\pm}$ that is consistent with ALEPH; however, they also report a limit for $m_{\tilde{\chi}_1^0}$ of 25.9 GeV/c^2 for any m_0 [21]. This limit increases to 30 GeV/c^2 with $\tan\beta$.

Lower limit of $m_{\tilde{\nu}}$

Unlike the $m_{\tilde{\chi}_1^\pm}$ and $m_{\tilde{\chi}_1^0}$ lower limits, the $m_{\tilde{\nu}}$ is not model dependent. The LEP1 experiment searched for Z^0 decays into previously unobserved channels. The result was a lower limit on $m_{\tilde{\nu}}$ of 41.1 GeV/c^2 at the 95% C.L. [22].

Lower limit of $m_{\tilde{t}_1}$

The ALEPH and OPAL measurements of $m_{\tilde{t}_1}$ are based on the assumption that all supersymmetric particles except $\tilde{\chi}_1^0$ and $\tilde{\nu}$ are heavier than the $\tilde{t}_1$ [23]. They search for $\tilde{t}_1$ in two channels, $\tilde{t}_1 \to c\tilde{\chi}_1^0$ and $\tilde{t}_1 \to b\, l\tilde{\nu}$. The sensitive regions for these experiments are $m_{\tilde{t}_1} - m_{\tilde{\chi}_1^0} \geq$10 GeV/c^{2}and $m_{\tilde{t}_1} - m_{\tilde{\nu}} \geq$10 GeV/c^2. The limits achieved are shown in Table 3.3.

Table 3.3: Recent limits on $m_{\tilde{t}_1}$ [23].

	channel: $\tilde{t}_1 \to c\tilde{\chi}_1^0$	channel: $\tilde{t}_1 \to b\, l\tilde{\nu}$
ALEPH	$m_{\tilde{t}_1} > 74$ GeV/c^2	$m_{\tilde{t}_1} > 82$ GeV/c^2
OPAL	$m_{\tilde{t}_1} > 80$ GeV/c^2	$m_{\tilde{t}_1} > 83$ GeV/c^2

3.1.2 Monte Carlo generation of signal

Signal event samples were created using the Monte Carlo generator ISAJET [24] version 7.20 with structure function CTEQ3L. ISAJET is the Monte Carlo generator capable of generating supersymmetric particles that is currently supported at by the CDF collaboration. The CLEO collaboration Monte Carlo package QQ version 9.0 was used to decay bottom and charm mesons according to the most recent measured branching ratios. The sparticle masses input into ISAJET were consistent with current limits. For the $\tilde{t}_1 \to b\tilde{\chi}_1^{\pm}$ decay scenario, we used $m_{\tilde{t}_1} =$ 100, 110, 115, and 120 GeV/c^2. We also used $m_{\tilde{\chi}_1^{\pm}} =$ 90 GeV/c^2 and $m_{\tilde{\chi}_1^0} =$ 40 GeV/c^2. In this decay, we were restricted to higher $m_{\tilde{t}_1}$ due to the high $m_{\tilde{\chi}_1^{\pm}}$. We forced one of the $\tilde{\chi}_1^{\pm}$ to decay via $\tilde{\chi}_1^+ \to l^+\nu\tilde{\chi}_1^0$ in this simulation. For the $\tilde{t}_1 \to bl\tilde{\nu}$ decay scenario, we used $m_{\tilde{t}_1} =$ 80 through 135 GeV/c^2, and $m_{\tilde{\nu}} =$ 40 through 50 GeV/c^2. Event reconstruction was performed with QFL$'$ (version 3.59).

The detector acceptance and signal selection efficiencies determined from simulation are used to predict the number of events observed in the data sample using a version of Eq. 2.1. For the $\tilde{t}_1 \to b\tilde{\chi}_1^{\pm}$ decay, we use the following equation:

$$N_{\rm obs} = \int \mathcal{L}dt\ \sigma_{\tilde{t}_1\bar{\tilde{t}}_1}\ [\mathcal{B} + (1-\mathcal{B})\mathcal{B}]\ \epsilon_{\rm trig}\ \epsilon_{\rm selection\ cuts}, \tag{3.1}$$

where σ is the theoretical cross section and $\mathcal{B}$ is the $\tilde{\chi}_1^+ \to l^+\nu\tilde{\chi}_1^0$ branching ratio of 11%. It is included as $[\mathcal{B}+(1-\mathcal{B})\mathcal{B}]$ because only one $\tilde{\chi}_1^{\pm}$ decay is forced, though both in reality may decay leptonically. Therefore, we include the probability that one $\tilde{\chi}_1^+$ decays leptonically plus the probability that the other $\tilde{\chi}_1^-$ decays leptonically given

that the first did not. For the $\tilde{t}_1 \to bl\tilde{\nu}$ decay, we forced no decays, so the number of events observed in the data is

$$N_{\rm obs} = \int \mathcal{L}dt \; \sigma_{\tilde{t}_1\bar{\tilde{t}}_1} \quad \epsilon_{\rm trig} \; \epsilon_{\rm selection\ cuts}. \tag{3.2}$$

Once we have measured $N_{\rm obs}$, we calculate the $\tilde{t}_1\bar{\tilde{t}}_1$ cross section by inverting Eqs. 3.2 and 3.1.

3.2 Modeling the backgrounds

We only modeled those Standard Model processes which we expected would be in our data after the first stage of filtering. This first stage of filtering will be described in detail in Chapter 4, but involves the $\tilde{t}_1$ signature of a lepton, at least 2 jets, and $\not\!\!E_T$. The complete list of these background processes is

1. $t\bar{t}$
2. $W^{\pm} \to l^{\pm}\nu$ + $\geq$2 jets
3. $b\bar{b}$
4. $Z \to \tau^+\tau^-$ + $\geq$ 1 jet
5. $Z \to e^+e^-(\mu^+\mu^-)$ + $\geq$ 2 jets
6. $\gamma \to l^+l^-$
7. $t\bar{b}$
8. $c\bar{c}$
9. fake leptons

For these processes which don't have neutrinos, the missing transverse energy typically comes from jet energy mismeasurement. A fake lepton is a particle, such as a pion, which is falsely reconstructed as an electron or muon. We use the term "fake leptons" to include events with a fake lepton, no heavy quarks, or both. Since real leptons are primarily a result of heavy flavor quark decay, we include the expected small contribution of light quark with real lepton events with the fake leptons. Fake lepton events are not modeled since this is something that QFL′ does not simulate. We, therefore, concentrate our efforts in the remainder of this chapter on the other eight background processes, which we will refer to as the Standard Model backgrounds. The fake lepton event contribution to the data sample will be determined later.

Each Standard Model background was modeled to determine the impact of signal selection cuts, discussed in Chapter 4. The numbers of background events surviving selection cuts are predicted from these cut efficiencies and CDF measured cross sections. For cases in which there is no measured cross section, corrections to Monte Carlo calculated LO cross sections are used. The numbers of background events are calculated using Eq. 3.2:

$$N_{\rm obs} = \int \mathcal{L} dt \; \sigma \;\; \epsilon_{\rm trig} \; \epsilon_{\rm selection \;\; cuts}.$$

The Monte Carlo generators and cross sections are discussed in the next section. In Section 4.7.2, we verify cross sections and cross section scale factors by comparing predicted background events to data.

3.2.1 Monte Carlo generation of backgrounds

The Monte Carlo generators used varied by process but in all cases reconstruction was performed with QFL′ (version 3.59).

Samples of $t\bar{t}$ (65,000) and $t\bar{b}$ (22,000) events were created using HERWIG [25] version 5.6 with structure function CTEQ3L. QQ version 9.0 was used to decay bottom and charm mesons according to the most recent measured branching ratios. We use the CDF measured value of $t\bar{t}$ production for $m_t = 175$ GeV/c^2 [26]:

$$\sigma_{t\bar{t}} = 5.1 \pm 1.6 \text{ pb},$$

and the value of $t\bar{b}$ production from W-gluon fusion for $m_t = 175$ GeV/c^2 calculated to NLO [27]:

$$\sigma_{t\bar{b}} = 1.70 \pm 0.15 \text{ pb}.$$

The $b\bar{b}/c\bar{c}$ and Drell-Yan samples were generated by Stephan Lammel using ISAJET with structure function CTEQ2L [17]. In each sample, one lepton was required to have $p_T \geq 9$ GeV/c. The production mechanisms for the $b\bar{b}/c\bar{c}$ samples are direct production and initial and final state gluon splitting. The ISAJET calculated cross sections for $b\bar{b}/c\bar{c}$ were shown to agree with data [28]. The Drell-Yan cross section,

$$\sigma_{\gamma \to l^+l^-}(p_T(l) \geq 9.0) = 135.4 \pm 0. \text{ pb},$$

must be scaled by 2.16 ± 0.11 to agree with data [28].

A $W^{\pm} \to e^{\pm}\nu + \geq 2$ jets sample (50,222 unweighted events) was provided by CDF collaborators from Duke University. It was generated using VECBOS [29] version 3.00 with structure function CTEQ3M and fragmented using HERWIG. The parton cuts for VECBOS were $p_T > 8$ GeV/c, $|\eta| < 3.5$, and parton-parton separation, ΔR_{jj},

greater than 0.4. The $W^{\pm} \to \mu^{\pm}\nu + \geq 2$ jets and $W^{\pm} \to \tau^{\pm}\nu + \geq 2$ jets samples were created from the electron sample, as is necessary when using VECBOS. The lepton flavors were changed prior to fragmentation and decay by HERWIG. The cross section times branching ratio was calculated by VECBOS using structure function CTEQ3L and $Q^2 = \langle p_T \rangle^2$ for the renormalization and fragmentation scales:

$$\sigma(W+ \geq 2 \text{ jets}) \times \mathcal{B}(W \to e\nu) = 404.121 \pm 0.213 \text{ pb}.$$

We generated Z + 1 jet and Z + 2 jets samples using VECBOS version 3.03 with CTEQ3L and fragmented with HERWIG. The parton cuts are identical to those in the W samples. Using $Q^2 = \langle p_T \rangle^2$ for the renormalization and fragmentation scales, the calculated cross sections are

$$\sigma(Z+ \geq 2 \text{ jets}) \times \mathcal{B}(Z \to e^+e^-) = 39.639 \pm 0.068 \text{ pb} \text{ and}$$

$$\sigma(Z+ \geq 1 \text{ jet}) \times \mathcal{B}(Z \to e^+e^-) = 87.637 \pm 0.061 \text{ pb}.$$

Scale factors have been measured at CDF to bring W or Z + jets LO QCD cross sections in agreement with data for jet $E_T \geq 15$ GeV and particular choices of renormalization and fragmentation Q^2s. The scale factors appropriate for these samples are data/theory($W, Z+ \geq 2$ jets) = 1.2 ± 0.1 and data/theory($W, Z+ \geq 1$ jet) = 1.5 ± 0.1 [30].

Since we generated Z events with VECBOS using a modified unweighting scheme, we will discuss it in detail in the next section.

3.2.2 The VECBOS unweighting scheme

VECBOS generates events which are given weights according to their probability of occurrence and such that the sum of all weights equals the cross section. Then each event contributes to a histogram according to its weight. Since a statistically significant sample of such events can be quite large, it is common to extract from it a set of events with unit weight but with frequencies according to their probability of occurrence. This unweighted sample is traditionally created by comparing the weight of a given event, W_i, to the largest weight in the sample, W_{max}. If the ratio W_i/W_{max} is greater than a random fraction, x, where $0 < x < 1$, the event is kept. Although the kinematic distributions of the weighted sample is preserved in this unweighting scheme, it can take a very large weighted sample to create a very modest unweighted sample. To improve the unweighting efficiency, we use the unweighting scheme proposed by M. Mangano [31] and implemented by D. Gerdes [32]. In this scheme, W_{max} is replaced by a smaller weight, $W_{<max}$, with one restriction - the events with $W_i > W_{<max}$ must be less than 10% of the cross section. This restriction

is to prevent the introduction of kinematic biases from keeping all high weight events, some of which can lie at the extremes of a distribution.

In practice, the $W_{<max}$ we chose was well within the restriction. For the $Z + \geq 2$ jets sample, it was chosen such that events with $W_i > W_{<max}$ represented less than 1.36% of the cross section. For the $Z + \geq 1$ jet sample, $W_{<max}$ was chosen such that events with $W_i > W_{<max}$ represented less than 0.42% of the cross section. Figures 3.1 and 3.2 are plots of the p_T of the Z, its daughter electrons, and the leading jet in each event for the $Z + \geq 2$ jets and $Z + \geq 1$ jet samples, respectively. Each histogram in the figures shows the distribution of both the unweighted and weighted samples. The deviation between the two samples is within the systematic error due to the choice of Q^2 in generation.

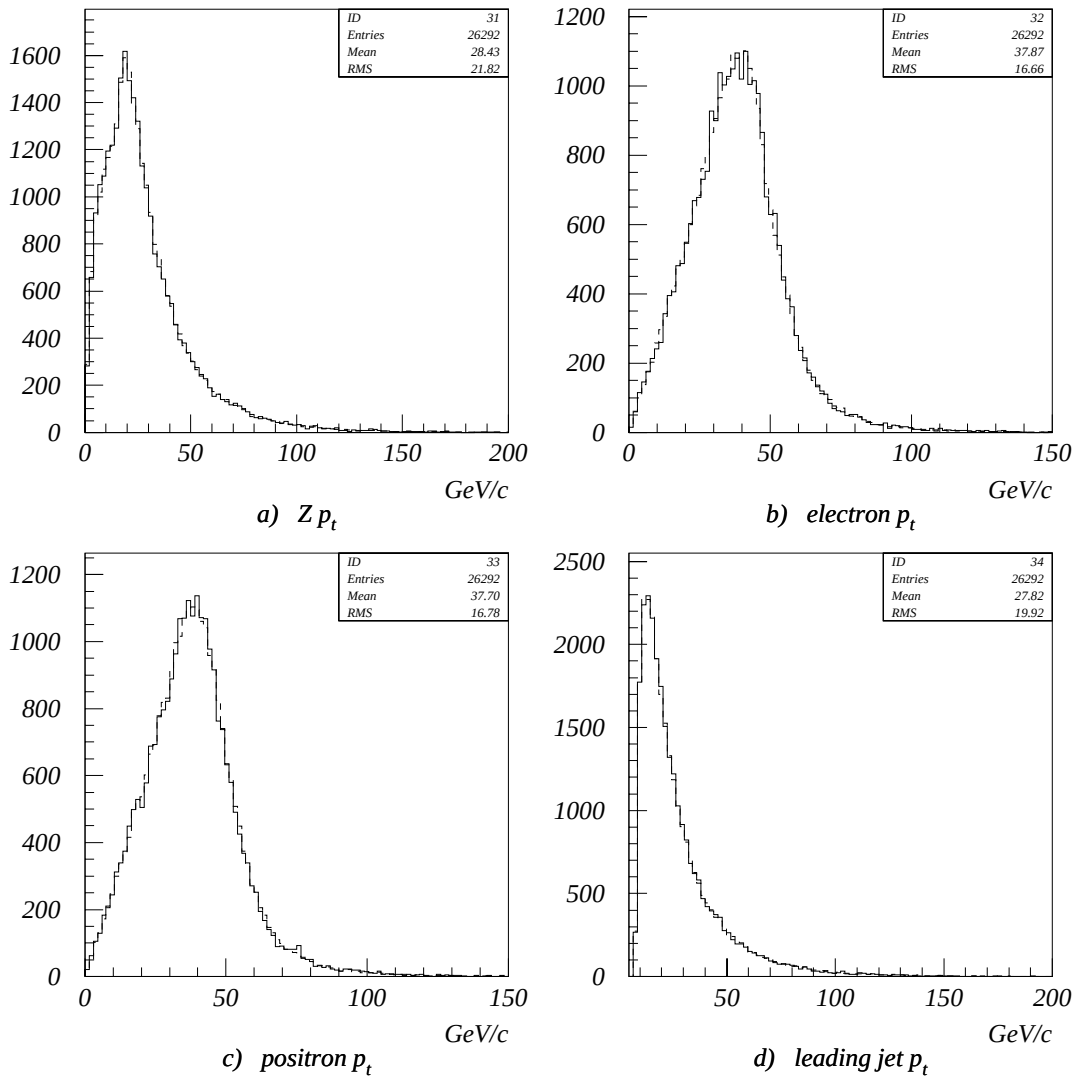

Figure 3.1: Histograms of four kinematic variables for both weighted and unweighted $Z \rightarrow e^+e^- + \geq 2$ jets events. The solid lines in each plot represent the sample after the unweighting procedure has been performed. The dashed lines represent the weighted sample normalized to the number of unweighted events.

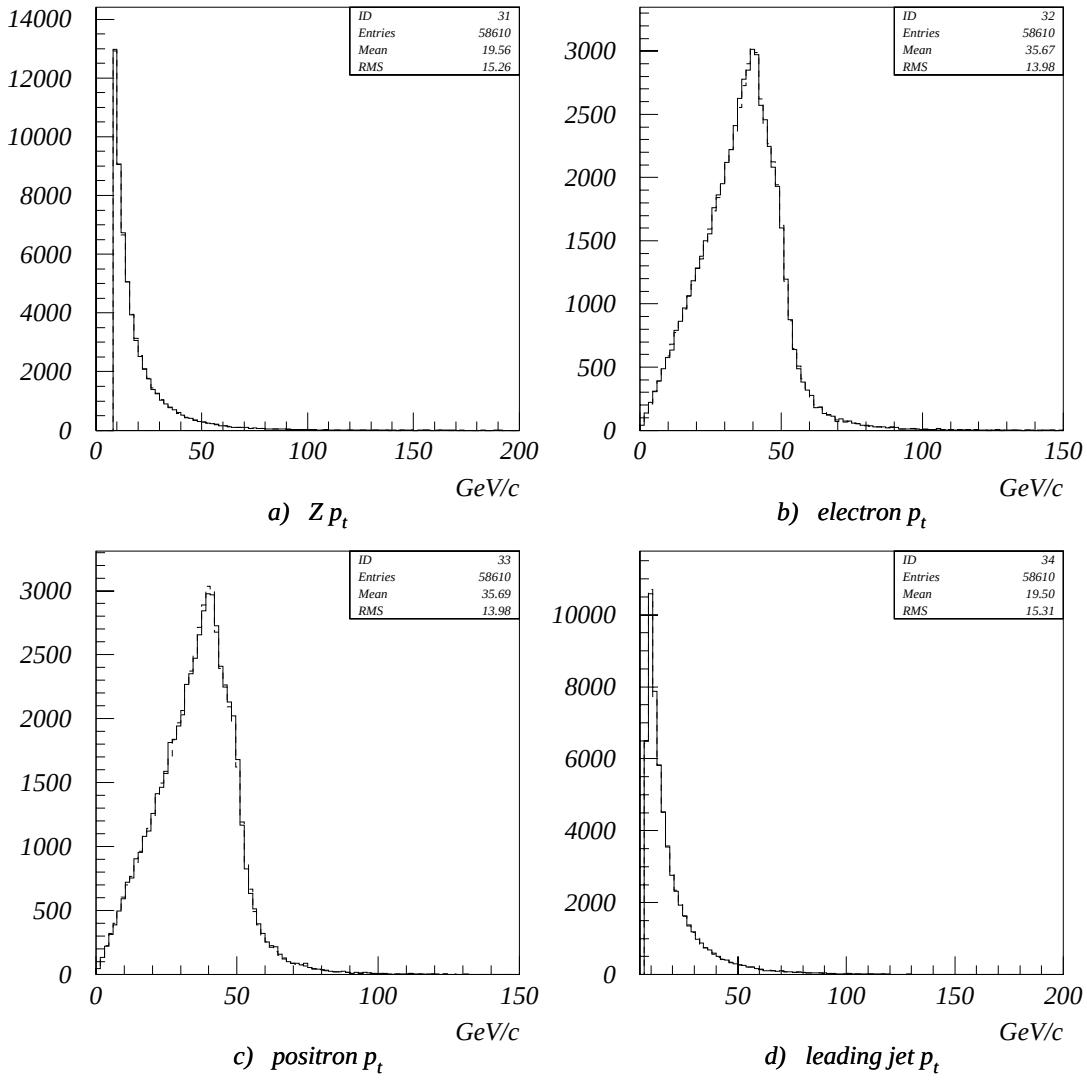

Figure 3.2: Histograms of four kinematic variables for both weighted and unweighted $Z \to e^+e^- + \geq 1$ jet events. The solid lines in each plot represent the sample after the unweighting procedure has been performed. The dashed lines represent the weighted sample normalized to the number of unweighted events.

Chapter 4

Data Reduction

The first step in analyzing signal selection criteria was to model the signal and relevant background processes. Having identified and modeled the relevant background processes we expected to have been recorded by our triggers in Section 3.2, we devised a four stage filtering process to improve our signal to background ratio. The four stages of filtering after triggering are

1. data tape stripping (require an isolated lepton with $p_T \geq 10$ GeV/c, $\not\!\!E_T \geq 15$, and one jet with $E_T \geq$12 GeV and a second with $E_T \geq$8 GeV)

2. Z^0/γ event reduction (remove events with two isolated, opposite sign leptons)

3. b jet tagging

4. $b\bar{b}$ reducing cuts (require $\not\!\!E_T \geq 25$ GeV and $\Delta\phi(\not\!\!E_T$, nearest jet$) \geq 0.5$)

The first filter comes from the $\tilde{t}_1$ decay signature described in Section 1.6. The rest of the filters specifically target the surviving backgrounds. Each of these filters will be described in detail.

We have mentioned that the $\tilde{t}_1$ decay signature is also the signature of the t quark. However, we could exploit the the potentially lower $\tilde{t}_1$ mass (and the potentially small mass difference between the $\tilde{\chi}_1^{\pm}$ and $\tilde{\chi}_0^{\pm}$ for the $\tilde{t}_1 \rightarrow b\tilde{\chi}_1^{\pm}$ decay scenario,) by using data from the low momentum, inclusive lepton triggers typically used in b quark analyses. These triggers and the data sets recorded from them, ECLB and MULB, were described in Section 2.3. In addition to describing the other four filters, we will describe the method we used to model the efficiencies of the ECLB and MULB triggers in the Monte Carlos.

4.1 Stripping

4.1.1 Stripping cuts

In the first step of filtering, data tapes are reduced to a subset of events that are considered richer in signal. In this step, referred to as stripping, the cuts are typically loose in order to record as much signal as possible, throwing away only the most irrelevant processes. Events from the ECLB and MULB data tapes were stripped using cuts that fall into three categories: 1) lepton identification cuts which are specific to the CDF detector, 2) event purity cuts driven by particular obvious backgrounds, and 3) loose energy cuts based on the physics process we wish to isolate.

We begin with the first category of cuts, lepton identification. There are a collection of standard CDF lepton identification cuts which are defined here.

Electron identification cuts

Had/EM is the ratio of the energy deposited in the CHA to the energy deposited in the CEM. Almost all of an electron's energy is deposited in the CEM. We use a common CDF cut for this quantity of Had/EM ≤ 0.05.

L_{SHR} is the transverse profile of the electromagnetic shower. The leakage of shower energy from an electron from its CEM tower into adjacent towers has a distinct shape as measured from test beam data. This shape is compared to electron candidate showers using the variable L_{SHR}, defined as

$$L_{SHR} \equiv 0.14 \sum_i \frac{E_i^{\text{adj}} - E_i^{\text{prob}}}{\sqrt{0.14^2 E + (\Delta E_i^{\text{prob}})^2}}$$

where E_i^{adj} is the measured energy in a tower adjacent to the seed tower, E_i^{prob} is the expected energy in the adjacent tower, $0.14\sqrt{E}$ is the error on the energy measurement, and ΔE_i^{prob} the error on the energy estimate. E_i^{prob} is calculated using a parameterization from test beam data. The electron requirement of $L_{SHR} \leq 2.0$ was made during triggering for ECLB data, and we did not impose it again later. Therefore, it is possible that some electron events were recorded in the MULB data without this requirement.

$|\Delta x|$ and $|\Delta z|$ are track matching cuts between a CTC track and the CES shower position. The $r - \phi$ plane matching requirement is $|\Delta x| \leq 3.0$ cm. The z matching requirement is $|\Delta z| \leq 5.0$ cm.

χ^2_{strip} is the comparison the CES pulse height for all 11 strips in a chamber to test beam data. This quantity is scaled for the energy of the cluster. The typical requirement is $\chi^2_{strip} \leq 10$.

$\chi^2_{\mathbf{wire}}$ is the comparison the wire pulse height in the CES to test beam data. Bremsstrahlung tends to broaden an electromagnetic shower in $r-\phi$, so this is not an ideal cut for high E_T electrons. The requirement of $\chi^2_{wire} \leq 10$ was made in the ECLB level 3 triggers, and we did not impose it again later. Again, it is possible that some electron events were recorded in the MULB data without this requirement.

Muon identification cuts

EM is the energy deposited in the CEM of the muon's tower. Since a muon should not deposit substantial amounts of energy in any calorimeter, we require EM$\leq$ 2.0 GeV.

Had is the energy deposited in the CHA of the muon's tower. The CHA contains more absorber material than the CEM, so a muon has a higher probability of depositing some energy. Therefore, we require Had $\leq$ 6.0 GeV.

$|\mathbf{\Delta x}|$ is a track matching cut between the CTC track and the muon chamber track in $r-\phi$. We require $|\Delta x| \leq 2.0$ cm between the CTC and the CMU and $|\Delta x| \leq$ 5.0 cm between the CTC and the CMP or CMX.

$\chi^2_{\mathbf{x}}$ **and** $\chi^2_{\mathbf{z}}$ are more track matching cuts between the CTC track and the muon chamber track in $r-\phi$ and z. They are a measure of the deviation of the track due to multiple scattering, energy loss, and measurement error. The MULB Level 3 triggers required $\chi^2_x \leq 11$ for muons in the CMU and CMP. The CMX requirement was $\chi^2_x \leq 16$. The MULB Level 3 triggers also required $\chi^2_z \leq 14$ for muons in the CMU with no CMP or CMX z requirement. We did not require this again, so it is possible that some muon events were recorded in the ECLB data without this requirement.

The lepton identification cuts are summarized in Tables 4.1 and 4.2. The efficiencies of these cuts on $Z^0 \rightarrow l^+l^-$ events have been studied by others [34, 35, 36] with results that agree within one standard deviation in the cases where the cuts are the same.

Table 4.1: Selection criteria for electrons. The efficiencies listed, computed in Ref. [34], are determined for $Z^0 \to e^+e^-$ events. The third column contains efficiencies determined from Run 1B data. The fourth column contains efficiencies obtained from Monte Carlo data reconstructed with QFL′.

Central Electron Identification			
Variable	Cut	Efficiency (1B)	Efficiency (MC)
Hadron/EM calorimeter energy	≤ 0.05	0.968±0.003	0.981±0.002
$\|\Delta x\|$ [cm]	≤ 3.0	0.973±0.003	0.977±0.002
$\|\Delta z\|$ [cm]	≤ 5.0	0.996±0.001	0.994±0.001
χ^2_{strip}	≤ 10.0	0.958±0.004	0.973±0.002
$\epsilon^{\dagger}_{\rm total}$		0.899±0.006	0.927±0.004

† Correlations between cuts are negligible.

Table 4.2: Selection criteria for muons. The efficiencies listed are for $Z^0 \to \mu^+\mu^-$ events and are taken from Refs. [34] and [35], as noted. The third column contains efficiencies determined from Run 1B data. The fourth column contains efficiencies obtained from Monte Carlo data reconstructed with QFL′. Results for CMU/CMP muons in Ref. [35] are for types CMU only, CMP only, or CMU/CMP.

Central Muon Identification			
Variable	Cut	Efficiency (1B)	Efficiency (MC)
EM calorimeter energy [GeV]			
(CMU/CMP)	≤ 2.0	0.958±0.010 [35]	0.989±0.002†
(CMX)	≤ 2.0	0.969±0.009 [35]	0.987±0.003 [34]
Hadron calorimeter energy [GeV]			
(CMU/CMP)	≤ 6.0	0.988±0.006 [35]	0.983±0.002†
(CMX)	≤ 6.0	0.988±0.005 [35]	0.988±0.003 [34]
$\|\Delta x\|$ (CMU) [cm]	≤ 2	0.952 ± 0.010 [35]	0.995±0.001‡
$\|\Delta x\|$ (CMP) [cm]	≤ 5	0.995 ± 0.002 [35]	0.995±0.001‡
$\|\Delta x\|$ (CMX) [cm]	≤ 5	0.993 ± 0.005 [35]	0.999±0.001‡
$\epsilon_{\rm total}$ (CMU/CMP)		0.923 ± 0.014 [35]	0.977±0.003†
$\epsilon_{\rm total}$ (CMX)		0.952±0.011 [35]	0.977±0.005 [34]

† This number is from Ref. [34] for CMU muons with CMP confirmation.
‡ This number is from Ref. [34] in which the efficiency is measured for an event passing either the $|\Delta x|$ or a $\chi^2_x < 9$ cut.

The second category of cuts, the event purity cuts, are designed to remove obviously undesirable events. These include events in which certain detector components were not functioning properly or the lepton has a known parentage (that is not our signal). These cuts are defined as:

Conversion Removal is the identification of electrons that are the daughters of photon conversion. CDF has a standard routine to identify these electrons which is called CONVERT2. This routine looks for a second track in an event that combined with the identified electron is consistent with a conversion pair. If there are, this is likely a photon that converted in the material of the solenoid.

Fiducial Area is the requirement that the lepton has hit a region of the detector with a well-understood response. CDF has standard routines for electrons and muons. The electron routine is called FIDELE and the muon routine is called FIDCMU92.

ISO is the calorimeter isolation of a lepton. The isolation is defined as the energy deposited in some cone around the lepton minus the energy of the lepton cluster, where the cone is defined by $\Delta R \equiv \sqrt{\Delta\phi^2 + \Delta\eta^2}$. This identifies leptons that are embedded in jets, as the result of a b quark decay, for example, since they will be surrounded by calorimeter activity. Leptons from the decays of gauge bosons will typically be separated from jets and be well isolated. We used a cone size of 0.4. We require that there be less than 2 GeV in energy surrounding the leptons. This is a rather tight cut, but was chosen to reduce the expected large contribution from b and c quark production events.

Bad Run Removal is the removal of events identified as occurring when some detector components were not operating properly or beam conditions were not nominal. There is a standard CDF routine to determine if the run was good, called BADRUN [37]. This routine compares the run number to a list of bad run numbers.

Cosmic Ray Removal identifies muons which are not a result of the $p\overline{p}$ collision, but from cosmic rays. We used a standard CDF routine to identify cosmic rays called CMCOS [38]. It identifies a cosmic ray muon as either not being consistent with originating at the primary vertex or being back-to-back with another muon track.

The event purity cuts and efficiencies are summarized in Table 4.3. The isolation efficiencies in Table 4.3 are for events which have passed the identification cuts in Tables 4.1 or 4.2.

Table 4.3: These lepton cuts are designed to remove obvious backgrounds that are common to many analyses. The third column contains efficiencies determined from Run 1B data taken from the references noted. The fourth column contains efficiencies obtained from Monte Carlo data reconstructed with QFL′.

Central Lepton			
Variable	Cut	Efficiency (1B)	Efficiency (MC)
Calorimeter Isolation:			
$\mathrm{Iso_{cal}}(\mathrm{R}=0.4)$ ($e^{\pm}$) [GeV]	≤ 2	0.8700±0.0084 [39]	0.963±0.003
$\mathrm{Iso_{cal}}(\mathrm{R}=0.4)$ ($\mu^{\pm}$) [GeV]	≤ 2	0.8977±0.0063 [39]	0.921±0.004
Cosmic Ray Removal		1.000±0.001 [34]	1.000±0.001 [34]
Photon Conversion Removal		0.958±0.004 [34]	0.977±0.002 [34]

The third category of cuts, the loose energy cuts based on the physics process we wish to isolate, is based on the $\tilde{t}_1\bar{\tilde{t}}_1$ signal described in Section 1.6. Prior to applying any selection criteria, the vertex associated with the highest p_T lepton was used as the primary vertex.[1] Jets were reclustered and $\not\!\!E_T$ was recalculated using the new vertex. The following loose cuts were made as a first pass at removing background:

- lepton energy requirement:
  - electron $E_T \geq 10$ GeV and $p_T \geq 7.5$ GeV/c, or
  - muon $p_T \geq 10.0$ GeV,
- $\not\!\!E_T \geq 15.0$ GeV,
- one jet with $p_T \geq 12.0$ GeV and $|\eta| \leq 2.0$,
- and second jet with $p_T \geq 8.0$ GeV and $|\eta| \leq 2.4$.

The electron p_T differs from its E_T because the E_T is the transverse energy deposited in the electron's CEM cluster, where the p_T is the transverse momentum of the electron measured by the CTC. The p_T requirement is less than the E_T requirement for the electron because the electron radiates as it traverses the magnetic field in the CTC, which lowers the p_T measurement. However, this radiated energy is recovered in the electron's CEM cluster. The $\not\!\!E_T$ described in Section 2.4.4, was

[1] A change in primary vertex was made for about 1% of the events in the ECLB and MULB data.

corrected for muons with $p_T \geq 7.5$ GeV/c, meaning the muon vector E_T was subtracted from the $\not\!\!E_T$. CDF also records minimum ionizing objects which have tracks and some calorimeter energy but which do not extrapolate to the fiducial regions of the muon chambers. These are considered muon candidates and the $\not\!\!E_T$ was also corrected for these objects if their p_T was greater than 20.0 GeV/c.

The geometrical acceptance $\times$ efficiency for each signal and background to pass the stripping cuts was determined by passing Monte Carlo generated events through QFL′ event reconstruction. The lepton identification efficiencies from QFL′ must then be corrected to the values obtained from data. This is done by inserting the values for $\epsilon^{\rm 1B}/\epsilon^{\rm QFL'}$ for $Z^0 \to l^+l^-$ events, given in Tables 4.1, 4.2, and 4.3, into the following equation:

$$(A \times \epsilon_{\rm strip})^{\rm 1B} = (A \times \epsilon_{\rm strip})^{\rm QFL'} \frac{\epsilon_{\rm id}^{\rm 1B}}{\epsilon_{\rm id}^{\rm QFL'}} \frac{\epsilon_{\rm conv}^{\rm 1B}}{\epsilon_{\rm conv}^{\rm QFL'}} \frac{\epsilon_{\rm cosm}^{\rm 1B}}{\epsilon_{\rm cosm}^{\rm QFL'}} \frac{\epsilon_{\rm iso}^{\rm 1B}}{\epsilon_{\rm iso}^{\rm QFL'}}. \quad (4.1)$$

4.1.2 Stripping results

The stripping efficiencies for $\tilde{t}_1\bar{\tilde{t}}_1$ events in the $\tilde{t}_1 \to b\tilde{\chi}_1^{\pm}$ decay scenario are listed in Table 4.4 as a function of $\tilde{t}_1$ mass, $\tilde{\chi}_1^{\pm}$ mass, and $\tilde{\chi}_1^0$ mass. The efficiencies are listed separately for the electron and muon channels representing the forced leptonic decay of one of the $\tilde{\chi}_1^{\pm}$s. The stripping efficiencies for the $\tilde{t}_1 \to bl\tilde{\nu}$ decay scenario are listed

Table 4.4: Stripping efficiencies for $\tilde{t}_1\bar{\tilde{t}}_1$ in the $\tilde{t}_1 \to b\tilde{\chi}_1^{\pm}$ decay scenario. Efficiencies are listed as a function of $m_{\tilde{t}_1}$.

$m_{\tilde{t}_1}$ [GeV/c^2]	$m_{\tilde{\chi}_1^{\pm}}$ [GeV/c^2]	$m_{\tilde{\chi}_1^0}$ [GeV/c^2]	$(A \times \epsilon_{\rm strip})^{\rm QFL'}$ $e^{\pm}$ decay channel	$(A \times \epsilon_{\rm strip})^{\rm QFL'}$ $\mu^{\pm}$ decay channel
100	90	40	0.204±0.004	0.209±0.004
110	90	40	0.263±0.004	0.274±0.004
115	90	40	0.288±0.005	0.275±0.004
120	90	40	0.309±0.005	0.295±0.005

in Table 4.5 as a function of $\tilde{t}_1$ mass and $\tilde{\nu}$ mass. These efficiencies are larger than those for $\tilde{t}_1 \to b\tilde{\chi}_1^{\pm}$ primarily because the leptons have higher energies.

The stripping efficiencies for the Standard Model backgrounds are listed by process in Table 4.6. The stripping efficiencies for some processes are effected by cuts imposed during Monte Carlo generation. These processes and cuts are noted in Table 4.6.

Table 4.5: Stripping efficiencies for $\tilde{t}_1\bar{\tilde{t}}_1$ in the $\tilde{t}_1 \to bl\tilde{\nu}$ decay scenario. Efficiencies are listed as a function of $m_{\tilde{t}_1}$ and $m_{\tilde{\nu}}$.

$m_{\tilde{t}_1}$ [GeV/c^2]	$m_{\tilde{\nu}}$ [GeV/c^2]	$(A \times \epsilon_{\rm strip})^{\rm QFL'}$
80	40	0.172±0.003
90	40	0.244±0.003
100	40	0.307±0.003
110	40	0.349±0.003
120	40	0.386±0.003
130	40	0.415±0.002
80	50	0.110±0.002
90	50	0.184±0.003
100	50	0.253±0.003
110	50	0.312±0.003
120	50	0.356±0.003
130	50	0.391±0.003

Table 4.6: Stripping efficiencies for Standard Model backgrounds.

background	$(A \times \epsilon_{\rm strip})^{\rm QFL'}$
$t\bar{t}$	0.204± 0.002
$W^{\pm} \to e^{\pm}\nu$ + ≥2 jets	0.128±0.001[a]
$W^{\pm} \to \mu^{\pm}\nu$ + ≥2 jets	0.106±0.001[a]
$W^{\pm} \to \tau^{\pm}\nu$ + ≥2 jets	0.015±0.0005[a]
$\gamma \to l^+l^-$	0.010±0.003[b]
$Z \to \tau^+\tau^-$ + ≥ 1 jet	0.019±0.001[a]
$Z \to e^+e^-$ + ≥ 2 jets	0.172±0.002[a]
$Z \to \mu^+\mu^-$ + ≥ 2 jets	0.147±0.002[a]
$t\bar{b}$ (from $W-g$ fusion)	0.090±0.002

[a]Determined from events with parton $p_T \geq 8.0$ GeV/c and $|\eta| \leq 3.5$.
[b]Determined from events with leptons with $p_T \geq 9.0$ GeV/c.

4.2 Modeling the Triggers

Level 1, 2, and 3 trigger efficiencies were modeled with a routine written by Stephan Lammel called MC_WGT. We modified this routine to include only those Level 3 triggers used for the ECLB and MULB streams [40]. The Level 1 and 2 triggers input into the ECLB and MULB data sets include all available CDF triggers: inclusive muon, inclusive electron, dilepton, inclusive photon, jet, total E_T, and $\not\!\!E_T$ triggers. The Level 3 triggers input into the ECLB and MULB data sets were limited to inclusive muon and inclusive electron triggers with low p_T thresholds.

The trigger efficiency for each contributing trigger was measured as a function of electron E_T or muon p_T, as appropriate. All Level 1 and 2 trigger efficiencies had been measured by other collaborators, but our Level 3 trigger efficiencies had not. A detailed description of our measurement of the Level 3 trigger efficiencies is given in Appendix A.

The MC_WGT routine codes the individual Level 1, 2, and 3 trigger efficiencies in bins of electron E_T or muon p_T of widths 0.5 or 1.0 GeV. The routine incorporates these efficiencies as the probability that a given event will pass a given trigger based on the E_T of the good lepton or leptons in an event. (Good leptons have passed the lepton identification cuts of a given trigger.) For all uncorrelated triggers at a given level, the logical OR of these probabilities is summed[2]. This provides the probability that an event passes a given level of triggering. The product of the probabilities that an event passes Levels 1, 2, and 3 is the total event weight. The weights for all events in a sample are summed and divided by the total number of events tested. These are the overall trigger efficiencies listed in Tables 4.7 through 4.9. The $\tilde{t}_1 \to bl\tilde{\nu}$ decays have higher trigger efficiencies that the $\tilde{t}_1 \to b\tilde{\chi}_1^{\pm}$ decays for a given $m_{\tilde{t}_1}$ due to higher lepton energies.

[2]The efficiencies of two uncorrelated triggers a and b are summed using

$$\epsilon_{a+b} = \epsilon_a + \epsilon_b(1 - \epsilon_a).$$

Table 4.7: Run 1B ECLB and MULB trigger efficiencies for $\tilde{t}_1\bar{\tilde{t}}_1$ in the $\tilde{t}_1 \to b\tilde{\chi}_1^{\pm}$ decay scenario. Efficiencies are for events passing the stripping cuts listed in Section 4.1.

$m_{\tilde{t}_1}$ [GeV/c^2]	$m_{\tilde{\chi}_1^{\pm}}$ [GeV/c^2]	$m_{\tilde{\chi}_1^0}$ [GeV/c^2]	ϵ_{trig} $e^{\pm}$ decay channel	ϵ_{trig} $\mu^{\pm}$ decay channel
100	90	40	0.824±0.008	0.439±0.010
110	90	40	0.825±0.007	0.492±0.009
115	90	40	0.827±0.007	0.489±0.009
120	90	40	0.836±0.007	0.488±0.009

Table 4.8: Run 1B ECLB and MULB trigger efficiencies for $\tilde{t}_1\bar{\tilde{t}}_1$ in the $\tilde{t}_1 \to bl\tilde{\nu}$ decay scenario. Efficiencies are for events passing the stripping cuts listed in Section 4.1.

$m_{\tilde{t}_1}$ [GeV/c^2]	$m_{\tilde{\nu}}$ [GeV/c^2]	$\epsilon_{\text{trig}}(e^{\pm})$	$\epsilon_{\text{trig}}(\mu^{\pm})$
80	40	0.834±0.009	0.515±0.011
90	40	0.830±0.007	0.531±0.010
100	40	0.845±0.006	0.551±0.009
110	40	0.842±0.006	0.548±0.008
120	40	0.856±0.005	0.574±0.007
130	40	0.859±0.005	0.582±0.007
80	50	0.818±0.011	0.494±0.014
90	50	0.833±0.008	0.538±0.011
100	50	0.846±0.006	0.549±0.013
110	50	0.841±0.006	0.552±0.012
120	50	0.854±0.005	0.566±0.011
130	50	0.862±0.005	0.593±0.010

Table 4.9: Run 1B ECLB and MULB trigger efficiencies for Standard Model backgrounds listed by process. Efficiencies are for events passing the stripping cuts listed in Section 4.1.

background	$\epsilon_{\rm trig}(e^{\pm})$	$\epsilon_{\rm trig}(\mu^{\pm})$
$t\overline{t}$	0.838±0.008	0.507±0.011
$W^{\pm} \to e^{\pm}\nu$ + ≥2 jets [a]	0.788±0.005	
$W^{\pm} \to \mu^{\pm}\nu$ + ≥2 jets [a]		0.358±0.007
$W^{\pm} \to \tau^{\pm}\nu$ + ≥2 jets	0.811±0.020	0.386±0.025
$b\overline{b}$ [b]	0.641±0.096	0.365±0.053
$\gamma \to l^{+}l^{-}$ [b]	0.841±0.015	0.386±0.024
$Z \to \tau^{+}\tau^{-}$ + ≥ 1 jet [a]	0.789±0.017	0.399±0.021
$Z \to e^{+}e^{-}$ + ≥ 2 jets [a]	0.861±0.005	
$Z \to \mu^{+}\mu^{-}$ + ≥ 2 jets [a]		0.405±0.008
$t\overline{b}$ (from $W-g$ fusion)	0.809±0.013	0.412±0.015
$c\overline{c}$ [b]	0.514±0.161	0.416±0.154

[a] Determined from events with parton $p_T \geq 8.0$ GeV/c and $|\eta| \leq 3.5$.
[b] Determined from events with leptons with $p_T \geq 9.0$ GeV/c.

4.3 Drell-Yan and Z^0 reduction

To reduce the contribution to our data sample from Drell-Yan and Z^0 events, we looked for those events that decayed to either electron pairs or muons pairs. To do this, we identified events with two good leptons that were of the same type but opposite charge. These leptons needed to be isolated to ensure they were not the result of heavy quark decay.

For e^+e^- candidates, at least one electron must have been central (deposited its energy in the CEM) and passed the cuts listed in Table 4.1. To improve detector acceptance, the second electron could either have been in the central or plug regions. The plug electromagnetic calorimeter is shown in Fig. 2.2. Although the plug electromagnetic calorimeter increases the acceptance for electrons in η, it is not used to identify both electrons because it has a lower identification reliability. If the second electron was central, it must have passed the cuts listed in Table 4.1. If it was in the plug region, it must have passed the cuts listed in Table 4.10. For the $\chi^2_{3\times3}$ cut, we look at the lateral sharing of energy in three towers in η by three towers in ϕ around an electron cluster's center. The $\chi^2_{3\times3}$ cut is a comparison of this shape to the expectation from test beam data [41]. It is applied to plug electrons in lieu of the L_{SHR} cut because the plug electromagnetic calorimeter has no shower-maximum detector.

Table 4.10: Selection criteria for electrons in the plug region. The efficiencies listed are taken from Ref. [34]. The third column contains efficiencies determined from Run 1B data. The fourth column contains efficiencies obtained from Monte Carlo data reconstructed with QFL′.

Plug Electron Identification			
Variable	Cut	Efficiency (1B)	Efficiency (MC)
Hadron/EM calorimeter energy	≤ 0.1	0.996±0.002	0.999±0.001
$\chi^2_{3\times3}$	≤ 3.0	0.956±0.005	0.922±0.004
ϵ_{total}		0.952±0.005	0.921±0.004

The $\mu^+\mu^-$ candidate events must have had at least one muon from the CMU/-CMP or CMX which passed the cuts listed in Table 4.2. The second muon may have been CMU/CMP, CMX, or a minimum ionizing object which had a track and some calorimeter energy but which did not extrapolate to the muon chambers. These latter objects, mentioned in Section 4.1, are considered muon candidates. The second CMU/CMP or CMX muon must have passed the cuts listed in Table 4.2. The minimum ionizing object must have passed the cuts listed in Table 4.11. The cut on the impact parameter, d_0, ensures that this object was not a cosmic ray.

Table 4.11: Selection criteria for minimum ionizing objects lacking stubs in the muon chambers. These objects are considered muon candidates. The efficiencies listed are taken from Ref. [34]. The third column contains efficiencies determined from Run 1B data. The fourth column contains efficiencies obtained from Monte Carlo data reconstructed with QFL′.

Minimum Ionizing Object Identification			
Variable	Cut	Efficiency (1B)	Efficiency (MC)
EM calorimeter energy	≤ 2.0 GeV	0.960±0.009	0.990±0.003
Hadron calorimeter energy	≤ 6.0 GeV	0.984±0.006	0.990±0.003
d_0	≤ 0.5 cm	1.000±0.002	1.000±0.001
$\epsilon_{\rm total}$		0.945±0.011	0.980±0.004

The first filter used for removing Drell-Yan and Z^0 events looked for events with the two good leptons described above that satisfied the following:

1. two like type leptons of opposite charge
2. both leptons with corrected $E_T \geq 10$ GeV
3. lepton $\mathrm{Iso_{cal}}(\mathrm{R} = 0.4) \leq 4.0$ GeV or $\Delta R_{ll} < 0.4$
4. $|z_0^{l_1} - z_0^{l_2}| < 10$ cm

The third filter requirement in this list limits the calorimeter activity surrounding the lepton in an $\eta - \phi$ cone defined by $R \equiv \sqrt{\eta^2 + \phi^2} = 0.4$. This isolation requirement is waived if the two leptons are within that cone of each other. The fourth filter requirement ensures that the leptons are consistent with originating from the same $p\overline{p}$ interaction. This is achieved by requiring the lepton tracks cross the z axis within 10 cm of each other.

The second filter used looked for one good central lepton (CEM for the electrons and CMU/CMP or CMX for the muons) and an isolated second track that together reconstructed the Z^0 mass. This second filter removes Z^0 events in which the second lepton was not properly identified, but was obviously a Z^0 daughter [42]. The filter looked for

1. a lepton with corrected $E_T(p_T) \geq 10$ GeV
2. a second track $p_T \geq 20$ GeV
3. the second track and lepton have opposite charge

4. lepton $\mathrm{Iso_{cal}(R = 0.4)} \leq 4.0$ GeV

5. second track $\mathrm{Iso_{track}(R = 0.4)} \leq 2.0$ GeV

6. second track $d_0 \leq 0.5$ cm

7. $|z_0^l - z_0^{\mathrm{track}}| \leq 10$ cm

8. $M_{l\ \mathrm{track}} \geq 50\ \mathrm{GeV/c^2}$

The fourth and fifth filter requirements are that the lepton and second track have limited calorimeter activity surrounding them in an $\eta - \phi$ cone of 0.4. This isolation requirement is tighter for the second track to lower the chance of misidentification. The seventh filter requirement is that the leptons must be consistent with originating from the same $p\overline{p}$ interaction. The last filter requirement is that the lepton and second track reconstruct a mass large enough to be consistent with the Z^0 mass.

The Standard Model backgrounds pass these Z^0/γ reducing cuts with the efficiencies listed in Table 4.12. These efficiencies have been corrected for the overefficiency of QFL$'$ to identify leptons using the cuts listed in Tables 4.1, 4.10, 4.2, and 4.11. The efficiencies for the Z^0/γ reducing cuts on signal are shown in Table 4.13 for the $\tilde{t}_1 \to b\tilde{\chi}_1^{\pm}$ decay and Table 4.14 for the $\tilde{t}_1 \to bl\tilde{\nu}$ decay.

Table 4.12: Efficiencies for passing the Drell-Yan and Z^0 reduction filter for each Standard Model background process after stripping cuts have been applied. The efficiencies for electron and muon events are listed separately.

background	$\epsilon^{\mathrm{1B}}_{\mathrm{dilep}}(e^{\pm})$	$\epsilon^{\mathrm{1B}}_{\mathrm{dilep}}(\mu^{\pm})$
$t\overline{t}$	0.927±0.003	0.915 ±0.004
$W^{\pm} \to e^{\pm}(\mu^{\pm})\nu + \geq$2 jets	0.996±0.001	0.997±0.001
$W^{\pm} \to \tau^{\pm}\nu + \geq$2 jets	0.998±0.002	0.998±0.002
$b\overline{b}$	0.993±0.032	0.988±0.053
$\gamma \to l^+l^-$	0.645±0.021	0.354±0.022
$Z \to \tau^+\tau^- + \geq 1$ jet	0.942±0.011	0.959±0.009
$Z \to e^+e^-$ $(\mu^+\mu^-)+ \geq 2$ jets	0.569±0.007	0.592±0.008
$t\overline{b}$ (from $W - g$ fusion)	0.992±0.002	0.992±0.002
$c\overline{c}$	1.000±0.098	0.969± 0.079

Table 4.13: Efficiencies for passing the Z^0 and γ removal filter for $\tilde{t}_1\bar{\tilde{t}}_1$ events in the $\tilde{t}_1 \to b\tilde{\chi}_1^{\pm}$ decay scenario. Efficiencies are for events passing stripping cuts. The efficiencies for electron and muon events are listed separately.

$m_{\tilde{t}_1}$ [GeV/c^2]	$m_{\tilde{\chi}_1^{\pm}}$ [GeV/c^2]	$m_{\tilde{\chi}_1^0}$ [GeV/c^2]	$\epsilon^{\mathrm{1B}}_{\mathrm{dilep}}(e^{\pm})$	$\epsilon^{\mathrm{1B}}_{\mathrm{dilep}}(\mu^{\pm})$
100	90	40	0.927±0.006	0.944±0.005
110	90	40	0.923±0.006	0.920±0.005
115	90	40	0.923±0.005	0.931±0.005
120	90	40	0.923±0.005	0.924±0.005

Table 4.14: Efficiencies for passing the Z^0 and γ removal filter for $\tilde{t}_1\bar{\tilde{t}}_1$ events in the $\tilde{t}_1 \to bl\tilde{\nu}$ decay scenario. Efficiencies are for events passing stripping cuts. Electron and muon events were not separated for the efficiency measurement.

$m_{\tilde{t}_1}$ [GeV/c^2]	$m_{\tilde{\nu}}$ [GeV/c^2]	$\epsilon^{\mathrm{1B}}_{\mathrm{dilep}}$
80	40	0.879±0.006
90	40	0.849±0.005
100	40	0.836±0.005
110	40	0.818±0.005
120	40	0.803±0.005
130	40	0.798±0.005
80	50	0.901±0.007
90	50	0.879±0.006
100	50	0.849±0.005
110	50	0.828±0.005
120	50	0.821±0.005
130	50	0.801±0.005

4.4 SVX b-jet tagging

In the third stage of filtering, we pass events containing b quark jets. Two routines were developed at CDF for use in the discovery of the top quark, *SECVTX* and *jet probability* . Both routines identify jets from b quark decays by using the relatively long B meson lifetimes and the high precision of the SVX detector. We tried both routines and used only the one which achieved the best signal to $\sqrt{\text{background}}$ ratio. The more successful routine, SECVTX, had a signal/$\sqrt{\text{background}}$ which was 16% better than the other according to very preliminary background studies. We describe this routine first.

4.4.1 The SECVTX filter

One of the CDF routines that identifies jets from b quark decays, and the one we used in this analysis, is called SECVTX. This routine vertexes SVX tracks in order to identify a vertex displaced from the primary vertex. This secondary vertex is then checked to ensure it is consistent with originating from B meson decay. The routine follows the steps listed below.

The JETS bank is used to list jets in clusters of cone size 0.4 or 0.7 with $E_T \geq 7.0$ GeV.

A list is made of all the SVX tracks recording their track quality and the quality of their corresponding CTC tracks. These tracks are corrected for dE/dx.

For each jet, a list is made of the SVX tracks in a cone around its jet axis with z_0 within 5 cm and impact parameter, d, within 0.15 cm of the primary vertex. The impact parameter is defined as the point of closest approach to the primary vertex in the $r - \phi$ plane. The impact parameter is positive for a positively charged particle if the track bends around the beam axis and negative if it bends away. This sign convention is reversed for negatively charged particles.

For each jet above a user specified minimum E_T and below a max η, track quality cuts are made on each constituent track. The cuts are a loose p_T cut, $\chi^2/\text{DoF} < 6$, CTC track quality, and an impact parameter significance ($|d|/\sigma_d \geq 2.5$) cut. A list of passing SVX tracks is saved.

These tracks are sorted by quality based on p_T, d/σ_d, and CTC track quality.

Track pairs are looped over (in order of quality) to find a seed secondary vertex. The remaining tracks are looped over to see if their d is within 3 σ of the seed secondary vertex. Passing tracks are saved with the seed tracks as forming a potential secondary vertex.

If a vertex with 3 or more tracks is formed, all associated tracks are fit to a 3-D vertex. Tracks whose vertexing χ^2 is greater than 50 are dropped from the fit, one at a time, and the fit is repeated until all tracks have $\chi^2 < 50$ or no good vertex is found.

For a vertex with only 2 tracks, higher p_T, better CTC track quality, and $|d|/\sigma_d \geq 3.0$ are required. Associated tracks are fit to a 3-D vertex. Tracks whose vertexing χ^2 is greater than 50 are dropped from the fit, one at a time, and the fit is repeated until all tracks have $\chi^2 < 50$ or no good vertex is found.

L_{xy}, the distance between the primary and secondary vertices, must be greater than 2.5 cm. In addition, L_{xy}/σ must be greater than a user specified minimum.

A secondary vertex is not used if it is from a K_S or its pseudo-$c\tau$ is greater than 1 cm, which is not consistent with a b decay.[3] The K_S filter removes 2 track vertices with no net charge and a mass near the K_S mass.

We use the following parameters in the SECVTX filter:

- jet cone size = 0.7
- jet $E_T \geq 8$ GeV
- cone size for tracks to be vertexed = 0.7
- $|d|/\sigma_d \geq 2.5$ for each vertexed track for the first pass
- $|d|/\sigma_d \geq 3.0$ for each vertexed track for the second pass
- $L_{xy}/\sigma_{L_{xy}} \geq 2.0$

The SVX b-tagging efficiency has been studied extensively for $t\bar{t}$ discovery using the low p_T inclusive electron data. It was determined that the Monte Carlo and data tagging rates were different by $\epsilon_{b\ \mathrm{tag}}^{\mathrm{1B}}/\epsilon_{b\ \mathrm{tag}}^{\mathrm{QFL'}} = 1.06 \pm 0.06$ for events with heavy quark decays [26]. Therefore, we apply this data/Monte Carlo scale factor to the Monte Carlo tagging rates measured for events from heavy quark production. The Monte Carlo tagging rates for our heavy flavor Standard Model backgrounds are listed in Table 4.15. The tag rate listed for $b\bar{b}$ in Table 4.15 is for direct production only, but the actual tag rate used for our background prediction includes potential variations in the rate due to gluon splitting. From Table 4.15, we see that the passing rate for events with heavy quarks is $\approx 40\%$. A significant factor in this rate the

[3] Pseudo-$c\tau$ is defined as $L_{xy} \times \mathrm{mass}/p_T$.

fiducial acceptance of the SVX, which is 67% for events on average. The Monte Carlo tagging rates for $\tilde{t}_1 \to b\tilde{\chi}_1^{\pm}$ are listed in Table 4.17, and the rates for $\tilde{t}_1 \to bl\tilde{\nu}$ are listed in Table 4.16. As previously mentioned, we chose to use this routine to tag our signal events so these are the efficiencies used in rest of the analysis.

Table 4.15: SVX b jet tagging efficiencies for SECVTX for each heavy flavor process after stripping and Z^0/γ reduction cuts have been applied. These are the Monte Carlo tagging efficiencies to which we apply the data/Monte Carlo scale factor to bring the results into agreement with measured data.

background	$\epsilon_{b\ \mathrm{tag}}^{\mathrm{QFL}'}$
$t\bar{t}$	0.467±0.005
$b\bar{b}$ (for direct prod.)	0.327±0.017
$t\bar{b}$ (from $W-g$ fusion)	0.315±0.010
$c\bar{c}$ (for direct prod.)	0.024±0.024

Table 4.16: SVX b-jet tagging efficiencies from secondary vertex finding routine for $\tilde{t}_1\bar{\tilde{t}}_1$ events in the $\tilde{t}_1 \to b\tilde{\chi}_1^{\pm}$ decay scenario. Efficiencies were determined after stripping and Z^0/γ reduction cuts had been applied. The tagging routine used is SECVTX. These are the Monte Carlo tagging efficiencies to which we apply the data/Monte Carlo scale factor to bring the results into agreement with measured data.

$m_{\tilde{t}_1}$ [GeV/c^2]	$m_{\tilde{\chi}_1^{\pm}}$ [GeV/c^2]	$m_{\tilde{\chi}_1^0}$ [GeV/c^2]	$\epsilon_{b\ \mathrm{tag}}^{\mathrm{QFL}'}(e^{\pm})$	$\epsilon_{b\ \mathrm{tag}}^{\mathrm{QFL}'}(\mu^{\pm})$
100	90	40	0.157±0.008	0.134±0.008
110	90	40	0.268±0.009	0.283±0.009
115	90	40	0.306±0.009	0.344±0.009
120	90	40	0.336±0.009	0.365±0.009

Events that are not heavy quark production still have a probability of having some associated heavy flavor jets (for example, $W^{\pm}b\bar{b}$ and $W^{\pm}c\bar{c}$) and of having jets mistagged as b jets due to track measurement error. This track measurement error is not modeled by QFL′ so mistag rates can not be determined from Monte Carlo. To estimate the rate at which non-heavy flavor processes will be mistagged, we use the method outlined in Ref. [43]. In this method, the tagging rate is measured for a generic jet data set, which will have some contribution from heavy flavor. Therefore, some portion of the tags in this sample will be from heavy flavor and the rest will be

Table 4.17: SVX b-jet tagging efficiencies for $\tilde{t}_1\bar{\tilde{t}}_1$ events in the $\tilde{t}_1 \to bl\tilde{\nu}$ decay scenario. Efficiencies were determined after stripping and Z^0/γ reduction cuts had been applied. The tagging routine used is SECVTX. These are the Monte Carlo tagging efficiencies to which we apply the data/Monte Carlo scale factor to bring the results into agreement with measured data.

$m_{\tilde{t}_1}$ [GeV/c^2]	$m_{\tilde{\nu}}$ [GeV/c^2]	$\epsilon_{b\text{ tag}}^{\text{QFL}'}$
80	40	0.270±0.008
90	40	0.294±0.007
100	40	0.324±0.007
110	40	0.342±0.006
120	40	0.375±0.006
130	40	0.380±0.006
80	50	0.224±0.009
90	50	0.265±0.008
100	50	0.302±0.007
110	50	0.337±0.007
120	50	0.346±0.006
130	50	0.370±0.006

mistags. The ratio of heavy flavor tags to mistags in this generic jet data will be the same as in our non-heavy flavor Standard Model backgrounds ($W^{\pm}$ + jets, Z^0 + jets, and Drell-Yan).

The tag rate for generic jets is parameterized as a function of jet E_T and track multiplicity and stored in a matrix [44]. This mistag matrix was determined for jets with minimum E_T = 15 GeV, so the lowest E_T bin is 15-25 GeV. Since we allow SECVTX to vertex 8 GeV jets, we approximated the mistag rate by extending the lowest bin to 13-25 GeV. We do not extend the lowest bin to 8 GeV because tagging efficiency falls off as jet E_T is lowered (see Fig. 4.1) and we would be overestimating the fake tag rate. We applied this matrix applied to our data sample after Z^0/γ event reduction cuts to get a rate based on the jet energies in our sample. The mistag rate determined with this method is 1.5% which we apply to our $W^{\pm}$ + jets, Z^0 + jets, and Drell-Yan Monte Carlo predictions. There is a quoted 13% systematic uncertainty on this number [43].

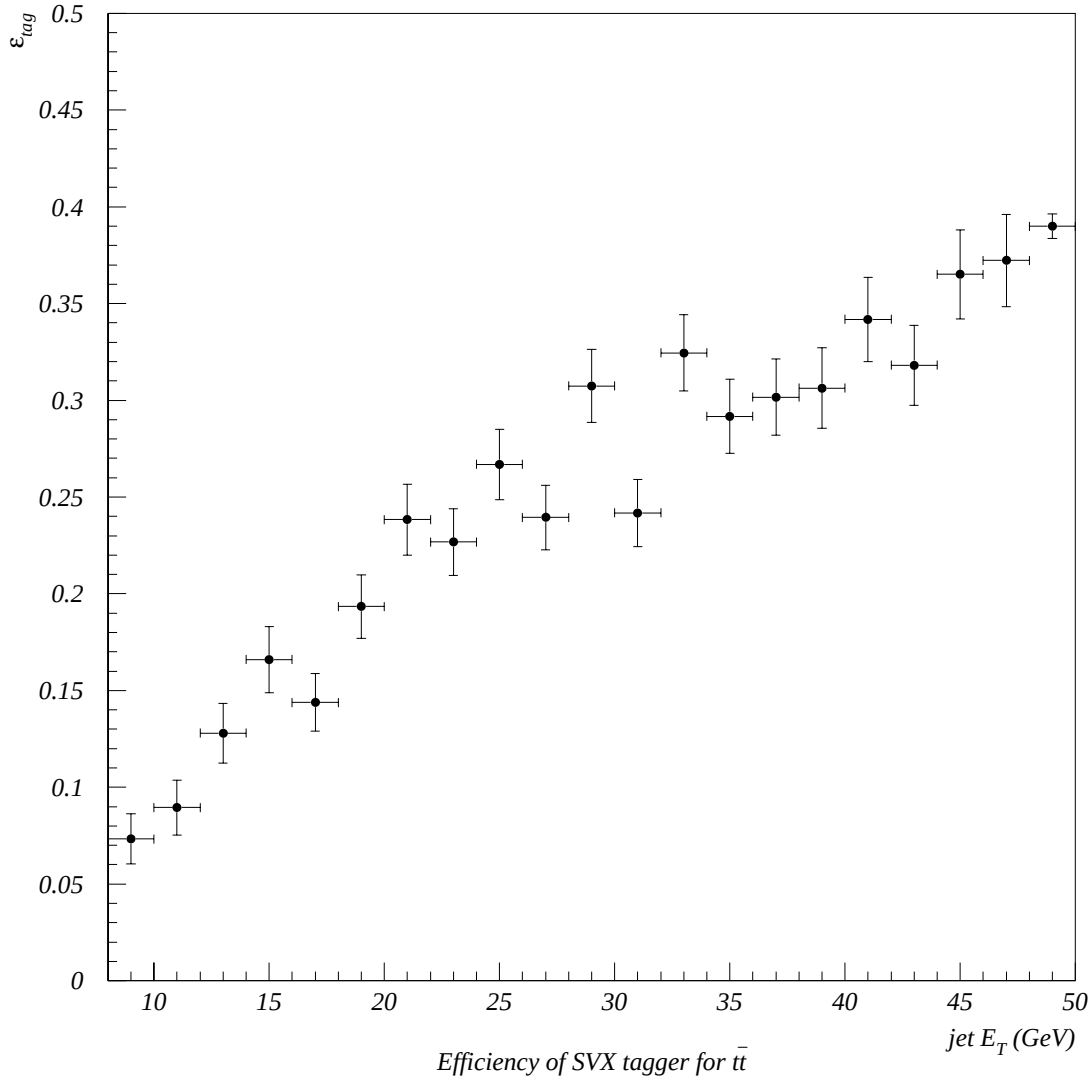

Figure 4.1: The SECVTX b jet tagging efficiency as a function of jet E_T for simulated top quark events. The shape of this distribution is due to the exponential lifetimes and the finite vertex resolution. The distribution plateaus above 50 GeV.

4.4.2 The Jet Probability filter

A second routine used by CDF to identify b jets is called *jet probability*. This routine uses a track's impact parameter to determine the probability that the track is consistent with originating from the primary vertex [45]. In this routine only, the sign of a track's impact parameter is positive if the track's point of closest approach to the primary vertex is on the same side of the vertex as the jet. This is different from the normal CDF convention described in the previous section. With this definition, a track originating from a heavy quark decay will have a positive impact parameter. Negative impact parameters are the result of track mismeasurement. In the absence of particle lifetime effects, the impact parameter distributions are solely a result of the SVX resolution function and are distributed symmetrically around zero. To determine the SVX resolution function, an inclusive jet sample with jet $E_T \geq 50$ GeV was used. This sample had only a small excess of events with positive impact parameters. The resolution function was the distribution SVX tracks from the inclusive jet sample with negative impact parameters.

The *jet probability* routine works as follows [46]:

Tracks originating from the primary vertex will have signed impact parameters consistent with the resolution of the SVX. Tracks originating from decays of long-lived particles will, in general, have larger positive impact parameters.

Comparing the signed impact parameter significances, d/σ_d, for each SVX track to the SVX resolution function yields a probability, P_i, that the track is consistent with originating from the primary vertex.

The track probabilities for tracks associated with a given jet are combined to give the probability, P_{jet}, that the jet is consistent with containing only primary tracks:

$$P_{jet} = \Pi \sum_{k=0}^{N-1} \frac{(-\ln \Pi)^k}{k!}$$

where $\Pi \equiv P_1 P_2 \ldots P_N$.

Tracks from K^0 and Λ decays are vetoed to minimize their contribution to P_{jet}.

We use the following parameters in the *jet probability* filter:

- jet cone size = 0.7
- track $p_T \geq 1.0$ GeV
- $|z_{\text{track}} - z_{\text{prim.vertex}}| \leq 5.0$ cm

- Minimum number of SVX hits = 2
- impact parameter ≤ 0.1 cm

The *jet probability* b-tagging efficiency has been studied for $t\bar{t}$ discovery and other supersymmetry searches at CDF. It was determined that the Monte Carlo and data *jet probability* tagging rates were different by $\epsilon_{b\ \mathrm{tag}}^{1\mathrm{B}}/\epsilon_{b\ \mathrm{tag}}^{\mathrm{QFL}'} = 0.88 \pm 0.12$ [47].

The efficiencies for Standard Model backgrounds to pass the *jet probability* filter are listed in Table 4.18. The efficiencies listed are for QFL$'$ and need to have the scale factor applied to bring them into agreement with measurements to data. Since no *jet probability* mistagging matrix is available at CDF, we applied this algorithm to both heavy flavor and non-heavy flavor Standard Model background Monte Carlos. Comparing Table 4.18 to Table 4.15, we still see the affect of the fiducial acceptance of the SVX, 67%, but we also see an increase in background efficiencies for events with tau leptons. Although the signal selection efficiencies for *jet probability*, listed in Table 4.19, are higher than those for SECVTX, from Table 4.16, we chose not to use this filter because of the increased backgrounds it accepts.

Table 4.18: SVX b jet tagging efficiencies from *jet probability* routine for each process after stripping and Z^0/γ reduction cuts have been applied. These efficiencies are shown for comparison with Table 4.15 but are not used in this analysis.

background	$\epsilon_{b\ \mathrm{tag}}^{\mathrm{QFL}'}$
$t\bar{t}$	0.530±0.008
$W^{\pm} \to e^{\pm}(\mu^{\pm})\nu$ + ≥2 jets	0.030±0.002
$W^{\pm} \to \tau^{\pm}\nu$ + ≥2 jets	0.085±0.010
$b\overline{b}$	0.400±0.073
$\gamma \to l^+l^-$	0.091±0.011
$Z \to \tau^+\tau^-$ + ≥ 1 jet	0.205±0.012
$Z \to e^+e^-(\mu^+\mu^-)$ + ≥ 2 jets	0.027±0.002
$t\overline{b}$ (from $W-g$ fusion)	0.403±0.011
$c\overline{c}$	0.224±0.051

Table 4.19: SVX b-jet tagging efficiencies from *jet probability* routine for $\tilde{t}_1\bar{\tilde{t}}_1$ events in the $\tilde{t}_1 \to b\tilde{\chi}_1^{\pm}$ decay scenario. Efficiencies were determined after stripping and Z^0/γ reduction cuts had been applied. These efficiencies are shown for comparison with Table 4.16 but are not used in this analysis.

$m_{\tilde{t}_1}$ [GeV/c^2]	$m_{\tilde{\chi}_1^{\pm}}$ [GeV/c^2]	$m_{\tilde{\chi}_1^0}$ [GeV/c^2]	$\epsilon_{b\ \mathrm{tag}}^{\mathrm{QFL}'}$
100	90	40	0.236±0.007
110	90	40	0.386±0.007

4.5 Unmodeled processes

We stated in Section 3.2 that QFL′ is not able to model some of the backgrounds we expected to find in our data sample. These Standard Model backgrounds not modeled by Monte Carlo are:

- $b\overline{b}$ and $c\overline{c}$ with fake leptons,
- light quarks with fake leptons, and
- light quarks with real leptons.

We called this collection of processes "fake leptons", since the first process listed will dominate after tagging.

We determined the number of these events remaining after tagging by looking in a low $\not\!\!E_T$ region ($15 \leq \not\!\!E_T \leq 20$ GeV) which is dominated by $b\overline{b}$, $c\overline{c}$, and light quarks. We use a fake lepton sample shown to us by Manfred Paulini to determine the efficiency of this $15 \leq \not\!\!E_T \leq 20$ GeV cut and to determine the best cuts to reduce this background. A description of this fake lepton sample can be found in Ref. [48]. The method they used was to reverse some of the good lepton identification cuts from Section 4.1. They derived one sample of fake electrons and two samples of fake muons in the following way:

1. fake electrons from Run 1B:

   HAD/EM cut was inverted (HAD/EM ≥ 0.4), and the dE/d χ^2 had to be inconsistent with the electron hypothesis by three standard deviations ($\chi^2_{\mathrm{d}E/\mathrm{d}x} > 9$).

2. fake muons from stream C:

   CMU muon track matching had to be negative ($\chi^2_z(CMU) < 0$). This is a characteristic of a punch through pion. Punch through causes the muon chamber ADC's to saturate and fail to provide the timing information used to determine the z position of the muon chamber hit.

3. fake muons from stream C:

   CMU muons without CMP confirmation but whose tracks extrapolate to the CMP.

To make sure this sample contained nothing but fake leptons, we required no good leptons with $p_T \geq 10$.

Table 4.20: Number of predicted Standard Model backgrounds versus data in the region $15 \leq \not\!\!E_T \leq 20$ GeV after b jet tagging. Fake leptons are normalized to data minus Standard Model backgrounds in this low $\not\!\!E_T$ region after tagging. The predicted number of signal events for $m_{\tilde{t}_1} = 100$ GeV/c^2 in the $\tilde{t}_1 \to b\tilde{\chi}_1^{\pm}$ decay scenario is shown for comparison to be negligible in this $\not\!\!E_T$ region.

process	Number of tagged events in $15 \leq \not\!\!E_T \leq 20$
$\tilde{t}_1$ (100)$\to b\tilde{\chi}_1^{\pm}$	1.10
$b\bar{b}$	73.9
$t\bar{t}$	1.22
$Z, \gamma \to l^+l^-$	4.43
$W^{\pm} \to e(\mu)^{\pm}\nu$ + $\geq$2 jets	5.72
combined Standard Model processes	85.3
data	221

This sample gave us our fake lepton event distributions and our $\not\!\!E_T$ region cut efficiency. 70% of these fake lepton events lie in the region $15 \leq \not\!\!E_T \leq 20$ GeV. In this low $\not\!\!E_T$ region, we normalized the number of fake lepton events to the number of tagged data minus the number of predicted Standard Model backgrounds. The numbers of predicted Standard Model backgrounds come from the efficiencies listed in the preceding sections, the cross sections from Section 3.2, and the integrated luminosities for our data samples from Section 2.3. The Standard Model predictions and the number of actual data are shown in Table 4.20. The fake lepton event normalization is 221 data - 85.3 Standard Model events = 136. Then we extrapolated to the entire $\not\!\!E_T$ region: 136/0.70=194 tagged fake lepton events.

4.6 Reduction of $b\bar{b}$ and light quark backgrounds

After b-jet tagging, the remaining data are primarily from $b\bar{b}$, $c\bar{c}$, and light quarks (fake lepton events). Among the possible cuts, raising the minimum $\not\!\!E_T$ gave the highest signal/$\sqrt{\text{background}}$. This was already hinted to in the previous section where a low $\not\!\!E_T$ region was used to isolate these events. Fig. 4.2 shows the distributions of $\not\!\!E_T$ for backgrounds and signal in the $\tilde{t}_1 \to b\tilde{\chi}_1^{\pm}$ decay scenario. Plotted in Fig. 4.3 is signal/$\sqrt{\text{background}}$ versus minimum $\not\!\!E_T$ for signal and background events. The best choice for a minimum $\not\!\!E_T$ cut is the maximum of the plot of signal/$\sqrt{\text{background}}$, which is at $\not\!\!E_T \geq 25$ GeV.

Another cut which is useful for removing $b\bar{b}$ and fake lepton events is a mini-

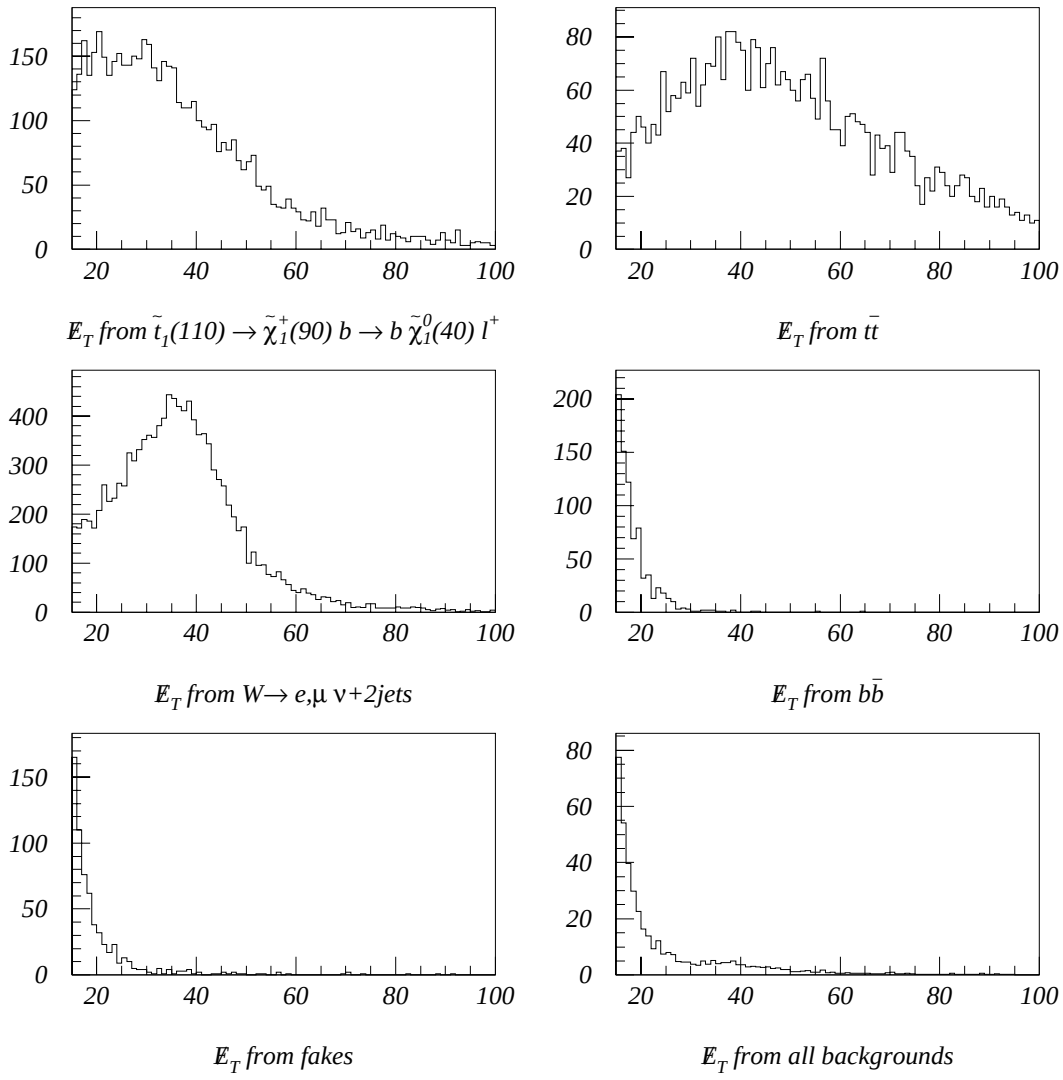

Figure 4.2: $\not\!\!E_T$ distributions (unnormalized) for $\tilde{t}_1$ of mass 110 GeV/c^2 in the $\tilde{t}_1 \to b\tilde{\chi}_1^{\pm}$ decay scenario and prominent backgrounds after b-jet tagging.

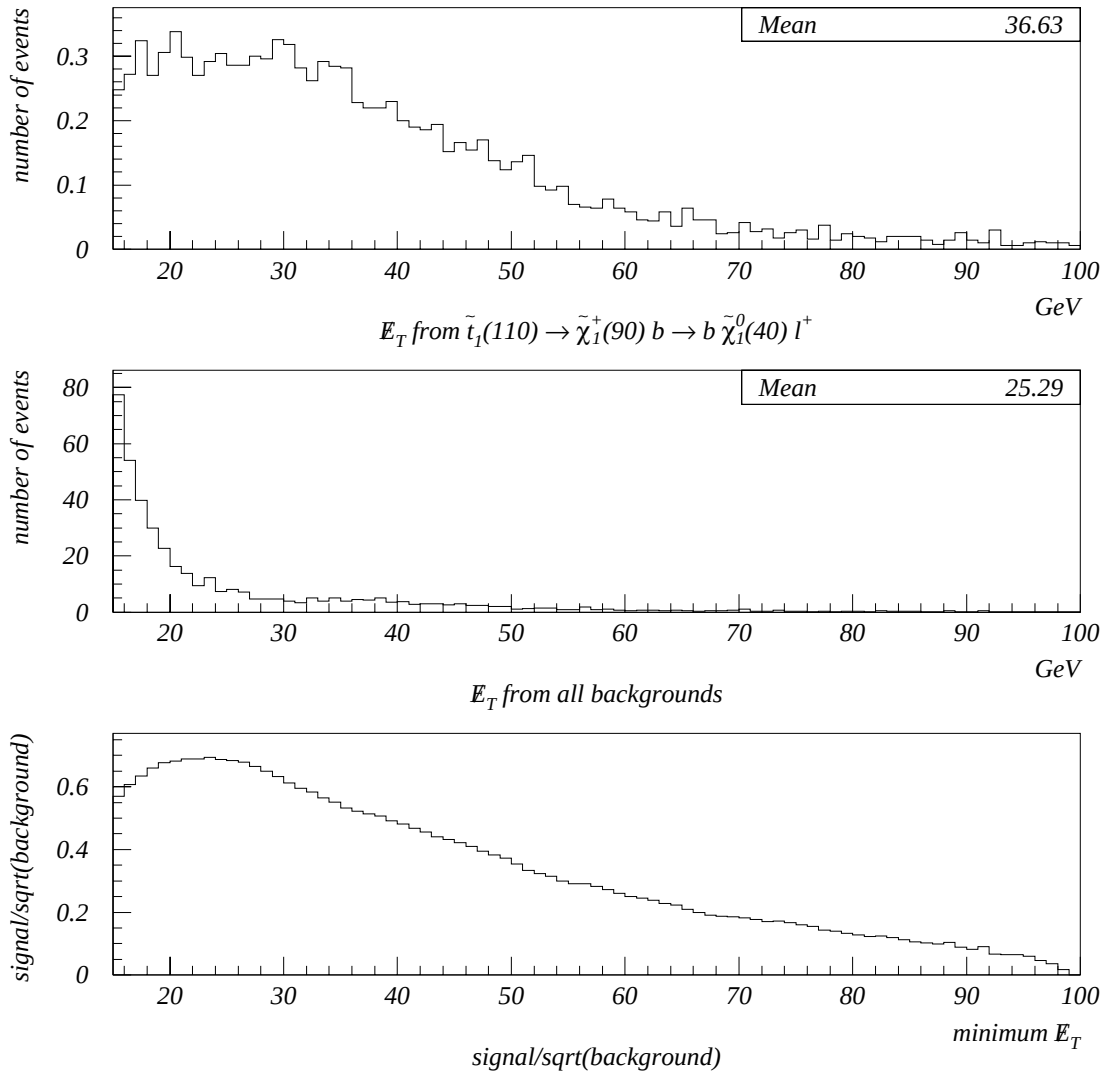

Figure 4.3: The top two plots show the $\not\!\!E_T$ distributions for $\tilde{t}_1$ of mass 110 GeV/c^2 and all backgrounds after b-jet tagging. All distributions have been normalized to the number of events expected after tagging in 88.59 (ECLB) and 87.43 (MULB) pb^{-1}. The bottom plot shows signal/$\sqrt{\text{background}}$ versus $\not\!\!E_T$ for a minimum $\not\!\!E_T$ cut. This motivates our choice of $\not\!\!E_T$ $\geq$25 GeV.

mum $\Delta\phi(\not\!\!E_T$, near jet). This is because for $b\overline{b}$ and fake lepton events, the $\not\!\!E_T$ often come from jet energy mismeasurement resulting in $\not\!\!E_T$ which is associated with some jet. Fig. 4.4 shows these distributions for signal ($\tilde{t}_1 \rightarrow b\tilde{\chi}_1^{\pm}$ decay scenario) and background. We chose a cut at $\Delta\phi(\not\!\!E_T$, near jet) $\geq$0.5.

We looked for an additional cut to reduce $b\overline{b}$ and fake lepton events further, such as lepton p_T or $p_T^{\rm rel}$ minima, but found nothing that could do this without decreasing the overall signal to background ratio. This is a result of $m_{\tilde{t}_1}$ being in between the top and bottom quark masses. A cut that lowers the signal to background ratio of one of these backgrounds does so at the expense of increasing it for the other.

The combined efficiencies for the $\not\!\!E_T \geq 25$ GeV and $\Delta\phi(\not\!\!E_T$, nearest jet) ≥ 0.5 cuts are listed in Table 4.21 for signal in the $\tilde{t}_1 \rightarrow b\tilde{\chi}_1^{\pm}$ decay scenario as a function of $m_{\tilde{t}_1}$. These efficiencies are listed in Table 4.22 for signal in the $\tilde{t}_1 \rightarrow bl\tilde{\nu}$ decay scenario as a function of $m_{\tilde{t}_1}$ and $m_{\tilde{\nu}}$. The Standard Model background efficiencies are listed in Table 4.23.

Table 4.21: Efficiencies for $\tilde{t}_1\bar{\tilde{t}}_1$ events in the $\tilde{t}_1 \rightarrow b\tilde{\chi}_1^{\pm}$ decay scenario to pass $\not\!\!E_T \geq$ 25 GeV and $\Delta\phi(\not\!\!E_T$, nearest jet) ≥ 0.5. Efficiencies were determined after stripping cuts were applied.

$m_{\tilde{t}_1}$ [GeV/c^2]	$m_{\tilde{\chi}_1^{\pm}}$ [GeV/c^2]	$m_{\tilde{\chi}_1^0}$ [GeV/c^2]	$\epsilon_{b\bar{b}\ \text{reduc.}}^{\text{1B}}$
100	90	40	0.556±0.007
110	90	40	0.564±0.006
115	90	40	0.554±0.007
120	90	40	0.558±0.006

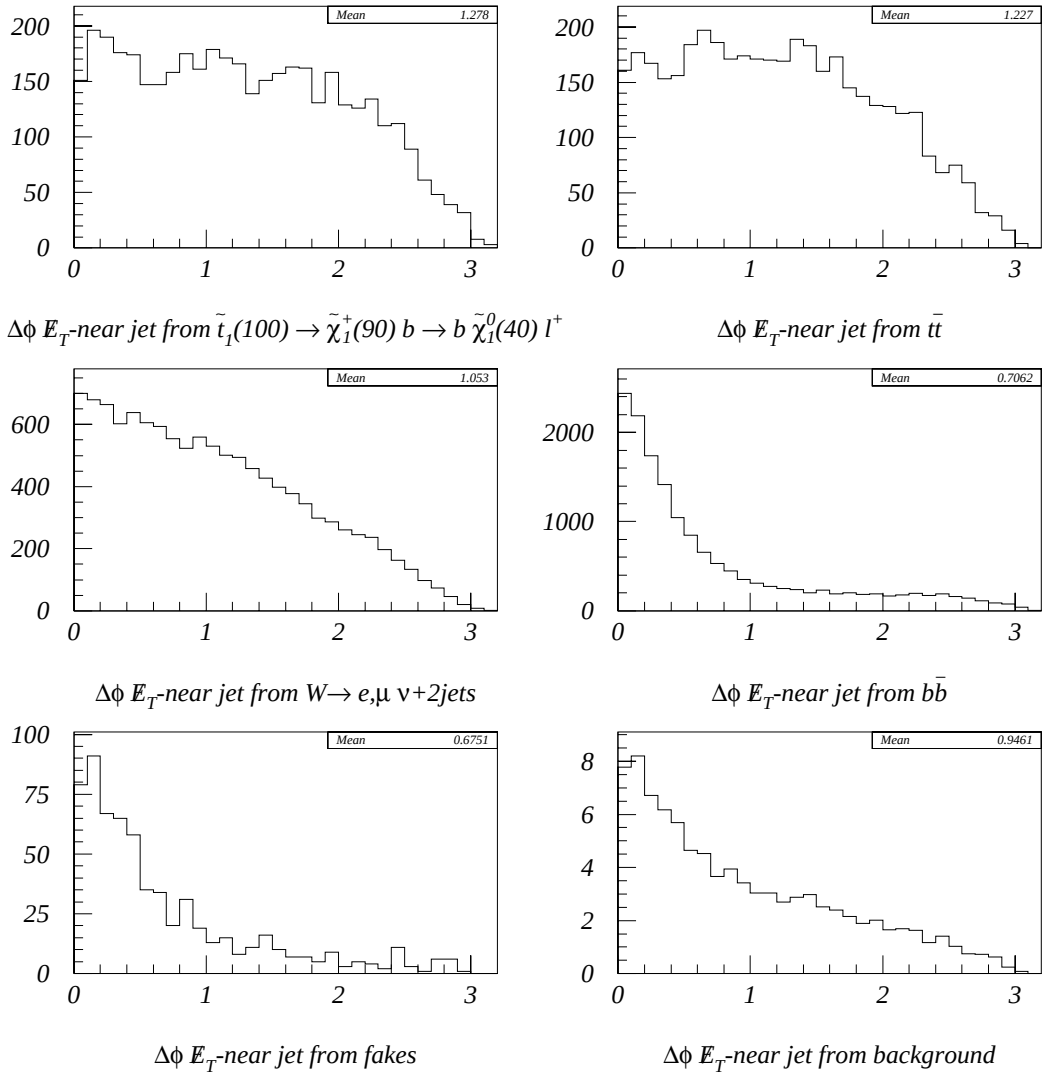

Figure 4.4: $\Delta\phi$(MET, near jet) distributions for $\tilde{t}_1$ of mass 100 GeV/c^2 and prominent backgrounds after b-jet tagging. The sixth plot shows the combined backgrounds normalized to the number of events expected after tagging in 88.59 (ECLB) and 87.43 (MULB) pb^{-1}.

Table 4.22: Efficiencies for $\tilde{t}_1\bar{\tilde{t}}_1$ events in the $\tilde{t}_1 \to bl\tilde{\nu}$ decay scenario to pass $\not\!\!E_T \geq$ 25 GeV and $\Delta\phi(\not\!\!E_T$, nearest jet$) \geq 0.5$. Efficiencies were determined after stripping cuts were applied.

$m_{\tilde{t}_1}$ [GeV/c^2]	$m_{\tilde{\nu}}$ [GeV/c^2]	$\epsilon_{bb\ \text{reduc.}}^{\text{1B}}$
80	40	0.452±0.017
90	40	0.524±0.013
100	40	0.564±0.010
110	40	0.598±0.009
120	40	0.629±0.008
130	40	0.640±0.008
80	50	0.434±0.022
90	50	0.484±0.016
100	50	0.544±0.012
110	50	0.583±0.010
120	50	0.612±0.009
130	50	0.632±0.008

Table 4.23: Efficiencies for passing $\not\!\!E_T \geq 25$ GeV and $\Delta\phi(\not\!\!E_T$, nearest jet$) \geq 0.5$ for each background process after stripping cuts have been applied.

background	$\epsilon_{bb\ \text{reduc.}}^{\text{1B}}$
$t\bar{t}$	0.714±0.006
$W^{\pm} \to e^{\pm}(\mu^{\pm})\nu$ + ≥2 jets	0.592±0.004
$W^{\pm} \to \tau^{\pm}\nu$ + ≥2 jets	0.515±0.017
$b\bar{b}$	0.062±0.006
$\gamma \to l^+l^-$	0.112±0.007
$Z \to \tau^+\tau^-$ + ≥ 1 jet	0.262±0.012
$Z \to e^+e^-$ $(\mu^+\mu^-)$+ ≥ 2 jets	0.221±0.003
$t\bar{b}$ (from $W-g$ fusion)	0.689±0.010
$c\bar{c}$	0.043±0.019
fake lepton events	0.06 ±0.007

4.7 Signal and background predictions

Every search for new physics must first demonstrate that the known physics is understood and reproducible. A powerful way of demonstrating that we understand the known physics is by making Standard Model predictions and showing that they agree with observation. We do this in this section by looking in regions of phase space where the $\tilde{t}_1$ contribution is expected to be negligible. Before we do this we will summarize the selection criteria for signal and show the number of predicted signal and Standard Model events after all selection criteria.

4.7.1 Summary of selection efficiencies from simulation

The cumulative selection efficiencies for the $\tilde{t}_1 \to b\tilde{\chi}_i^{\pm}$ decay scenario are the products of the efficiencies from Tables 4.4, 4.7, 4.13, 4.16, and 4.21 for each $\tilde{t}_1$ mass. These cumulative selection efficiencies for $\tilde{t}_1 \to b\tilde{\chi}_i^{\pm}$ are plotted as a function of $\tilde{t}_1$ mass in Fig. 4.5. Similarly for the $\tilde{t}_1 \to bl\tilde{\nu}$ decay scenario, the cumulative selection efficiencies are the products of the efficiencies from Tables 4.5, 4.8, 4.14, 4.17, and 4.22 for each $\tilde{t}_1$ mass and $\tilde{\nu}$ mass. The cumulative selection efficiencies for $\tilde{t}_1 \to bl\tilde{\nu}$ are plotted as a function of $\tilde{t}_1$ mass in Figs. 4.6 and 4.7 for $m_{\tilde{\nu}}$=40 and 50 GeV/c^2, respectively. All cumulative efficiencies plotted do include Monte Carlo correction factors.

The cumulative selection efficiencies for the Standard Model backgrounds from Tables 4.6, 4.12, 4.15, and 4.23 are multiplied by the cross sections from Section 3.2 and the integrated luminosities for our data samples from Section 2.3 to give a prediction of the number of expected backgrounds. These are listed by process in Table 4.24. The predicted numbers of $\tilde{t}_1 \to b\tilde{\chi}_i^{\pm}$ events for $m_{\tilde{t}_1}$= 100 and 110 GeV/c^2 are listed for comparison. The predicted numbers of signal events are made using the NLO theoretical cross sections from Table 1.5.

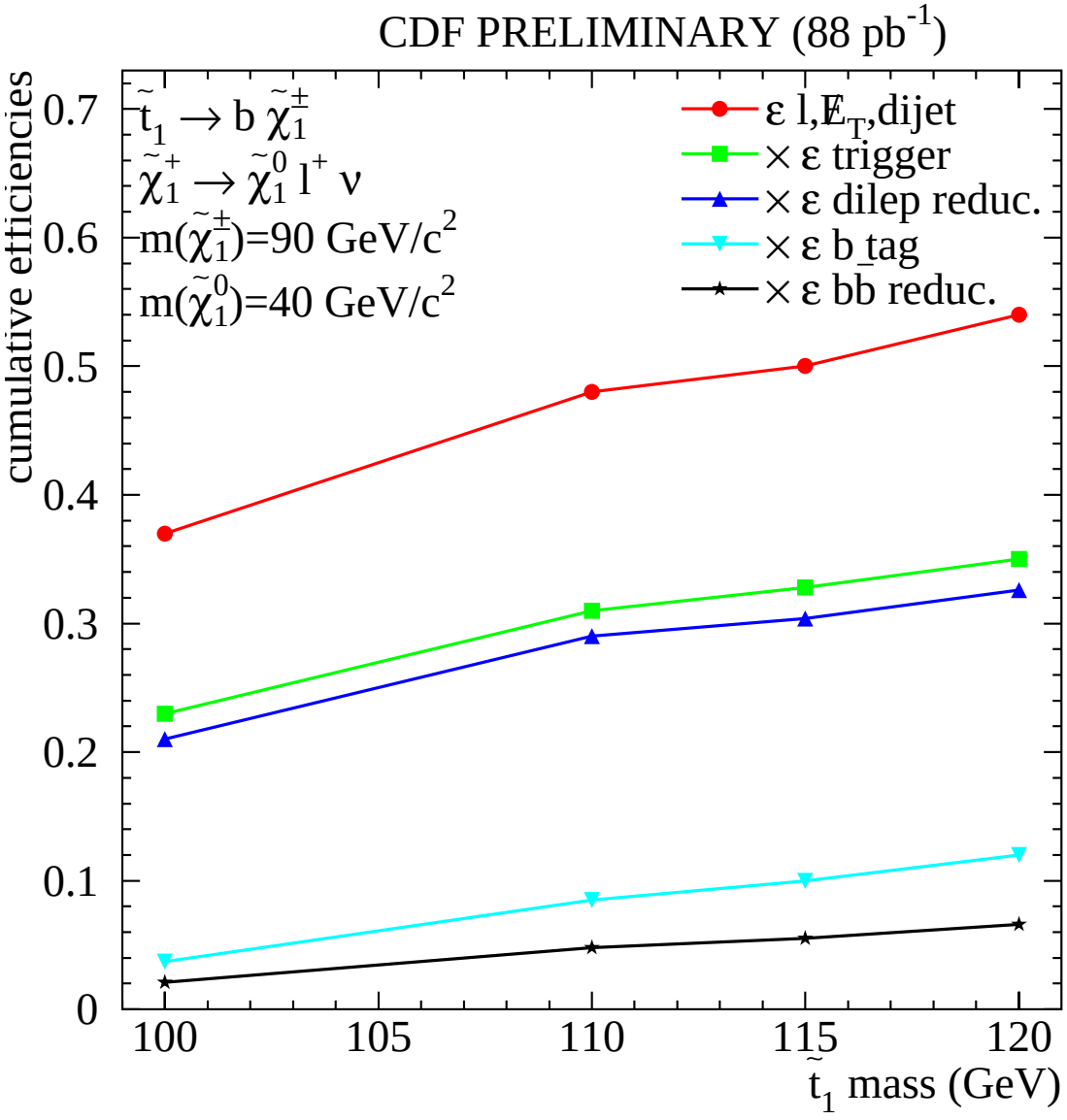

Figure 4.5: Cumulative selection efficiencies for $\tilde{t}_1 \rightarrow b\tilde{\chi}_1^{\pm}$ as a function of $m_{\tilde{t}_1}$. Efficiencies include Monte Carlo correction factors which bring QFL′ into agreement with measured efficiencies.

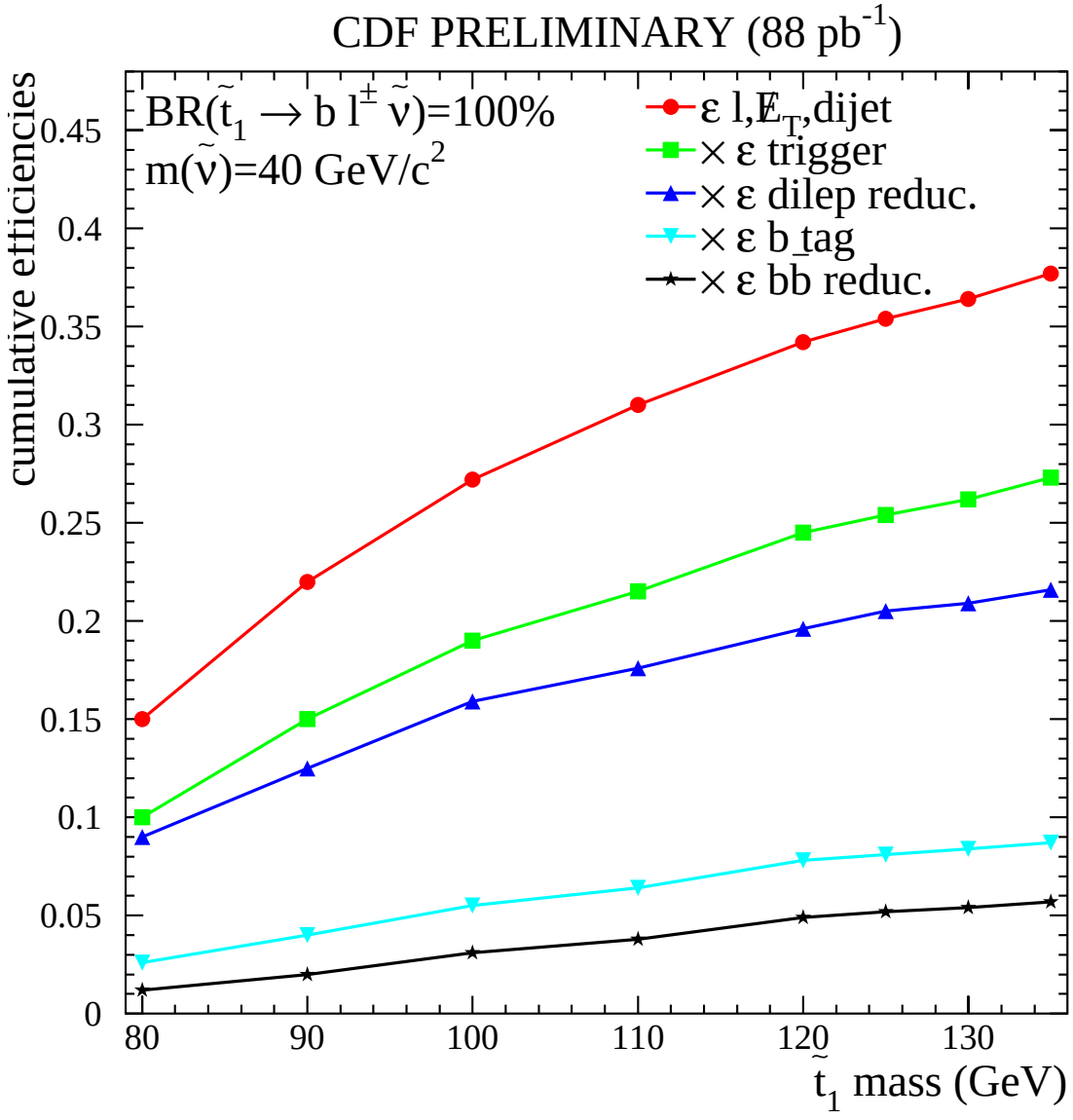

Figure 4.6: Cumulative selection efficiencies for $\tilde{t}_1 \rightarrow bl\tilde{\nu}$ as a function of $m_{\tilde{t}_1}$ for $m_{\tilde{\nu}}$=40 GeV/c^2. Efficiencies include correction factors which bring Monte Carlo into agreement with measured efficiencies.

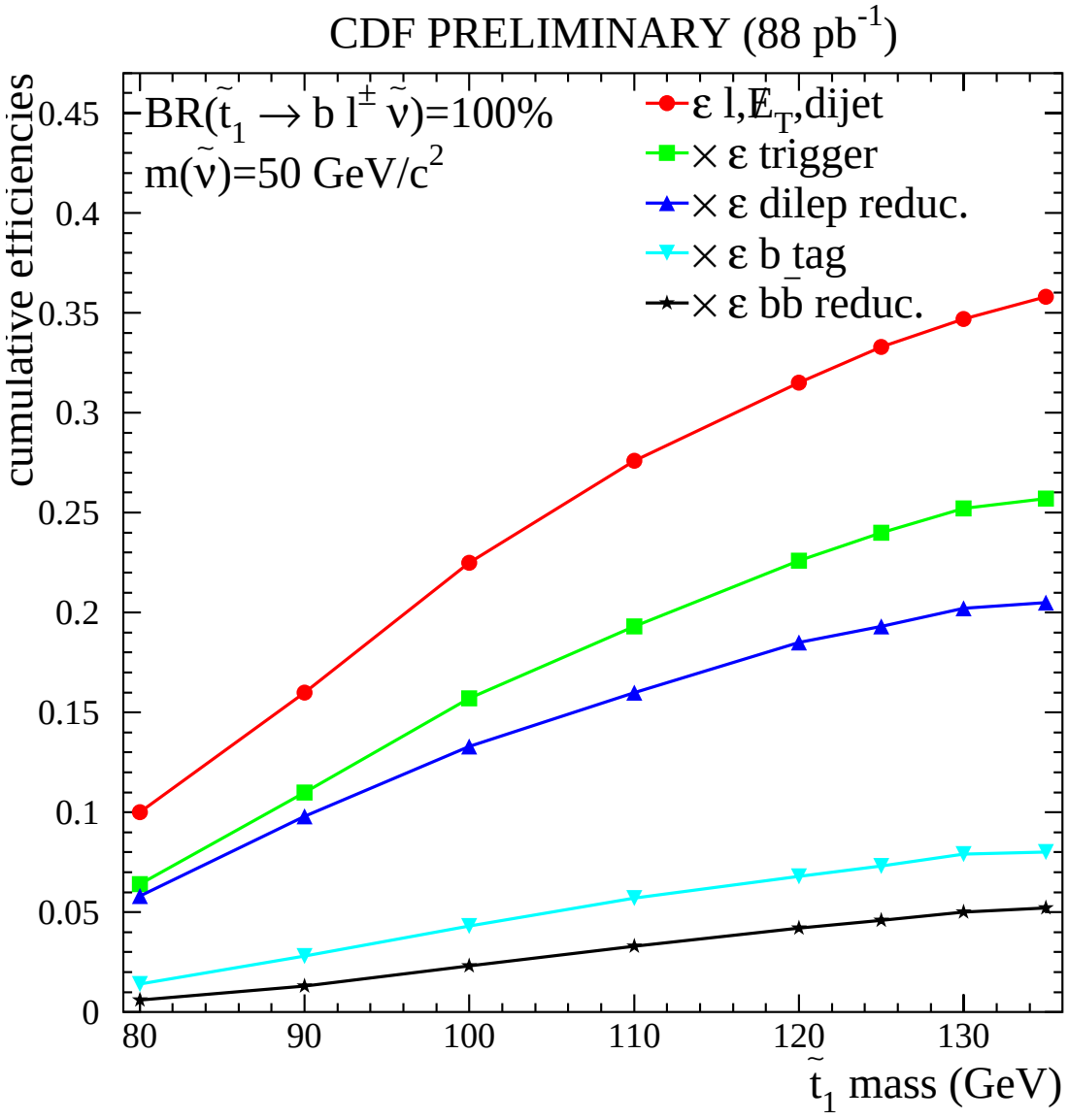

Figure 4.7: Cumulative selection efficiencies for $\tilde{t}_1 \rightarrow bl\tilde{\nu}$ as a function of $m_{\tilde{t}_1}$ for $m_{\tilde{\nu}}$=50 GeV/c^2. Efficiencies include correction factors which bring Monte Carlo into agreement with measured efficiencies.

Table 4.24: Numbers of expected events after all selection cuts listed by process. Errors listed are uncorrelated only. The predicted numbers of signal events are made using the NLO theoretical cross sections from Table 1.5.

CDF PRELIMINARY (88 pb^{-1})

process	number of tagged events with $\not\!\!E_T \geq 25$ and $\Delta\phi$ ($\not\!\!E_T$, near jet) $\geq$0.5 (uncorrelated errors only)
$\tilde{t}_1$ (100)$\rightarrow b\tilde{\chi}_i^{\pm}$	4.4$\pm$0.2
$\tilde{t}_1$ (110)$\rightarrow b\tilde{\chi}_i^{\pm}$	6.4$\pm$0.2
$t\bar{t}$	17.8$\pm$4.1
$W^{\pm} \rightarrow e(\mu)^{\pm}\nu$ + $\geq$2 jets	44.5$\pm$3.9
$W^{\pm} \rightarrow \tau^{\pm}\nu$ + $\geq$2 jets	2.6$\pm$0.2
$b\bar{b}$	5.8$\pm$0.6
$\gamma \rightarrow l^+l^-$	0.4$\pm$0.04
$Z \rightarrow \tau^+\tau^-$ + $\geq$ 1 jet	0.4$\pm$0.04
$Z \rightarrow e^+e^-(\mu^+\mu^-)$ + $\geq$ 2 jets	1.4$\pm$0.1
$t\bar{b}$ (from $W-g$ fusion)	1.6$\pm$0.1
$c\bar{c}$	0.06$\pm$0.02
fake leptons	11.6$\pm$1.3
background total	86.2$\pm$5.2

4.7.2 Cross checks on background normalizations

In this section, we demonstrate that our Standard Model predictions for $b\bar{b}$, $t\bar{t}$, Z^0 + jets, and γ + jets agree with observation under some set of cuts, so that we have confidence in their overall normalizations. The greatest uncertainty for all Standard Model backgrounds are their cross sections. So the demonstrated agreement between prediction and observation serves as a cross check on these measured or calculated cross sections.

Cross check on $b\bar{b}$ and $t\bar{t}$ normalizations

The normalizations of the number of $b\bar{b}$ and $t\bar{t}$ were verified by counting the number of events with two SECVTX tagged b jets, or double tagged events. The efficiencies for all other standard model processes for double b tagging are negligible. If the double tagged events are separated into a low $\not\!\!E_T$ region ($15 \leq \not\!\!E_T \leq 20$ GeV) and a high $\not\!\!E_T$ region ($\not\!\!E_T \geq 20$ GeV), the number of $b\bar{b}$ and $t\bar{t}$ can be verified independently. Table 4.25 shows the number of predicted $b\bar{b}$ and $t\bar{t}$ in Run 1B after all selection cuts, scale factors, and trigger efficiencies have been applied. The number of signal events from the $\tilde{t}_1 \to b\tilde{\chi}_1^{\pm}$ decay scenario are shown in Table 4.25 to be negligible. This number is for comparison and is not included in the total. The number of signal events from the $\tilde{t}_1 \to bl\tilde{\nu}$ decay scenario is shown for comparison as well, but is not negligible for double tagged events. To compare the $b\bar{b}$ normalization to data in a region free from $\tilde{t}_1 \to bl\tilde{\nu}$ signal, we applied an additional cut to the low $\not\!\!E_T$, double tagged sample. This cut is lepton $p_T \leq 15$ GeV/c and is shown in Table 4.26. To compare the $t\bar{t}$ normalization to data in a region free from $\tilde{t}_1 \to b\tilde{\nu}$ signal, we applied the additional cut of $H_T \geq 250$ GeV to the high $\not\!\!E_T$, double tagged sample. This result is also shown in Table 4.26. Good agreement is demonstrated in both Tables between prediction and observation.

Cross check on Z^0 and Drell-Yan normalizations

The normalizations of the number of Z^0 and Drell-Yan can be verified by comparing the number of stripped events that fail the Z^0/γ reduction cuts to the predicted number from Monte Carlo. This is shown in Table 4.27 which contains results from Table 4.28. For electrons, the predicted number in good agreement with data. For muons, the predicted number is in acceptable agreement with data, if we consider that the numbers of these types of events are greatly reduced after tagging.

Table 4.25: The number of predicted and actual double SVX b jet tagged events after triggering, stripping, and Z^0/γ reduction cuts have been applied. The numbers of double tagged events are divided into two regions in $\not\!\!E_T$ in order to separate $b\bar{b}$ and $t\bar{t}$. The number of signal events from the $\tilde{t}_1 \to b\tilde{\chi}_1^{\pm}$ decay scenario is shown to be negligible for comparison and is not included in the total. The number of signal events from the $\tilde{t}_1 \to b\tilde{\nu}$ decay scenario is shown for comparison as well, but is not negligible for double tagged events.

	Number of double tagged events			
process	$15 \leq \not\!\!E_T \leq 20$		$\not\!\!E_T \geq 20$	
	electron	muon	electron	muon
$\tilde{t}_1(100) \to b\tilde{\chi}_1^{\pm}$	0.09	0.04	0.36	0.17
$\tilde{t}_1(100) \to bl\tilde{\nu}$	1.20	0.81	4.63	3.15
$t\bar{t}$	0.24	0.15	4.60	2.91
$b\bar{b}$	6.23	1.91	1.70	0.52
total	6.5	2.0	6.3	3.4
data	6	2	4	3

Table 4.26: The number of predicted and actual double SVX b jet tagged events after triggering, stripping and Z^0/γ reduction cuts have been applied. The numbers of double tagged events are divided into two regions in $\not\!\!E_T$ in order to separate $b\bar{b}$ and $t\bar{t}$. An additional selection requirement was applied to the low $\not\!\!E_T$ region to reduce the signal contribution from $\tilde{t}_1 \to bl\tilde{\nu}$. The selection requirement is lepton $p_T \leq 15$ GeV/c. A different additional selection requirement was applied to the high $\not\!\!E_T$ region to reduce the signal contribution. The cut is $H_T \geq 250$ GeV. H_T is defined as the sum of the transverse energy in an event from the highest p_T lepton, $\not\!\!E_T$, and all jets of at least 8 GeV. The number of signal events are shown to be negligible for comparison and are not included in the total.

	Number of double tagged events			
process	$15 \leq \not\!\!E_T \leq 20$ lepton $p_T \leq 15$		$\not\!\!E_T \geq 20$ $H_T \geq 250$	
	electron	muon	electron	muon
$\tilde{t}_1(100) \to bl\tilde{\nu}$	0.16	0.11	0.63	0.43
$t\bar{t}$	0.01	0.01	2.71	1.72
$b\bar{b}$	3.80	1.17	0.06	0.02
total	3.8	1.2	2.8	1.7
data	4	2	2	0

Table 4.27: Comparison of the predicted number of events removed by Z^0/γ reduction cuts and the actual number. The discrepancy between the muon prediction and observation is acceptable considering these events have a negligible contribution to our final data sample (see Table 4.24.)

	Standard Model Background prediction from Monte Carlo		Low p_T inclusive lepton data	
	electron	muon	electron	muon
events removed by Z^0/γ reduction	374.6±23.05	173.6±11.03	393	124

4.8 Summary of selection requirements applied to data

Having verified that our Standard Model predictions for $b\bar{b}$, $t\bar{t}$, Z^0 + jets, and γ + jets agree with observation, we can summarize our background predictions and compare them to observation. Table 4.28 shows there is good agreement between modeled backgrounds and data after each of the first three filters. The predicted number of modeled Standard Model events after b tagging is 214. The predicted contribution from fake lepton events is 194. The total number of predicted events is 408 which is in excellent agreement with the 394 events in the data.

Table 4.28: Remaining events in data and Monte Carlo after stripping, Z^0/γ reduction, and b jet tagging. Results include trigger efficiencies and all scale factors. The fake lepton event estimation was made by subtracting the Monte Carlo predictions from data in a low $\not\!\!E_T$ region after b-jet tagging. Therefore, we do not show a fake lepton prediction prior to b jet tagging.

Cut	SM Background events from Monte Carlo		Fake leptons	Low p_T inclusive lepton data	
	electron	muon		electron	muon
stripping cuts	5,253	2,074		9,400	3,899
Z^0/γ reduction	4,878	1,900		9,007	3,776
b tagging	144.1	70.2	194	275	119

Figs. 4.8 and 4.9 show the $\not\!\!E_T$ distributions for all background processes before and after b jet tagging, respectively. In Fig. 4.8, the fake lepton event normalization is the number of data minus Standard Model backgrounds before tagging. The good agreement between data and Monte Carlo predictions in Figs. 4.8 and 4.9 is a good cross check on the fake lepton event normalization. Figs. 4.10 and 4.11 show the transverse mass distributions for all background processes before and after b jet tagging, respectively. Transverse mass is the invariant mass reconstructed from the $\not\!\!E_T$ and the lepton and has a peak around 70 GeV/c^2 from $W^{\pm}$ events. The fake lepton event distribution shown in Fig. 4.10 has a peak at low M_T which is the result of not requiring isolated leptons in the fake lepton sample. If fake leptons are required to be isolated, the peak is greatly reduced, but the sample has low statistics. To correct for this, we normalize the fake lepton event distribution with $M_T > 5$ to the number predicted. The good agreement in Figs. 4.10 and 4.11 between data and Monte Carlo predictions provides a good cross check on the $W^{\pm}$ normalization. Figs. 4.12 and 4.13 compare the background predictions with data for lepton p_T before and after

tagging, respectively. The fake lepton event normalization in Fig. 4.12, as in Fig. 4.8, is the number of data minus Standard Model backgrounds before tagging.

The number of expected backgrounds after all filtering, Table 4.24, are compared with the data remaining from our sample after all filtering in Table 4.29. All errors in Table 4.29 include the errors of cross section and cross section scale factors as well as the statistical errors. We see no excess of data in our sample and so will set upper limits for signal cross sections in the next chapter.

Table 4.29: Comparison of predicted backgrounds to data after selection cuts.

CDF PRELIMINARY (88 pb^{-1})

process	number of tagged events with $\not\!\!E_T \geq 25$ and $\Delta\phi$ ($\not\!\!E_T$, near jet) $\geq$0.5 (uncorrelated errors only)
$t\bar{t}$	17.8±4.1
$W^{\pm} \to e(\mu)^{\pm}\nu$ + $\geq$2 jets	44.5±3.9
$W^{\pm} \to \tau^{\pm}\nu$ + $\geq$2 jets	2.6±0.2
$b\bar{b}$	5.8±0.6
$\gamma \to l^+l^-$	0.4±0.04
$Z \to \tau^+\tau^-$ + $\geq$ 1 jet	0.4±0.04
$Z \to e^+e^-(\mu^+\mu^-)$ + $\geq$ 2 jets	1.4±0.1
$t\bar{b}$ (from $W-g$ fusion)	1.6±0.1
$c\bar{c}$	0.06±0.02
fake leptons	11.6±1.3
background total	86.2±5.2
data	81

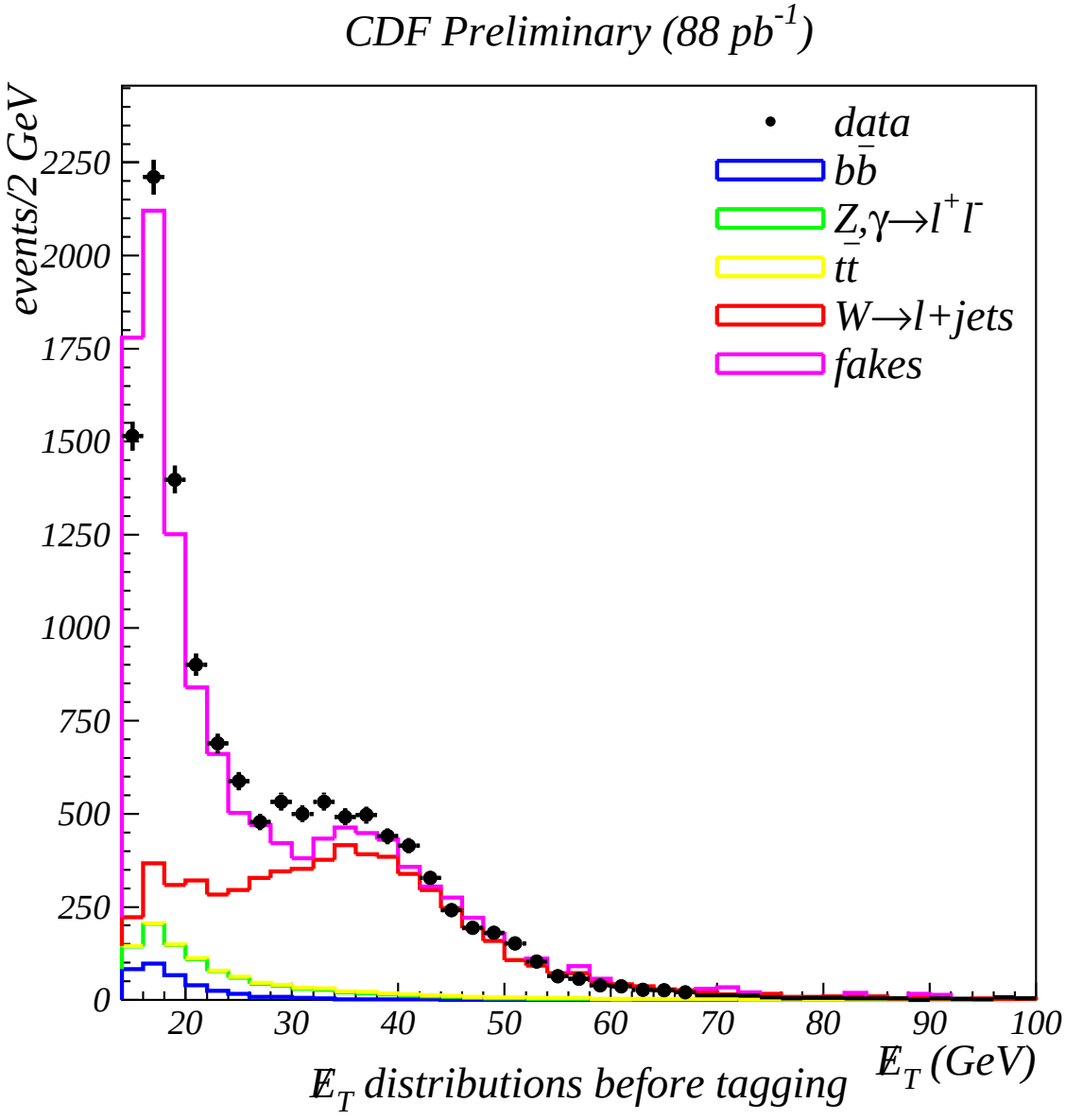

Figure 4.8: Comparison of data to normalized $\not\!\!E_T$ distributions for backgrounds after Z^0/γ event reduction.

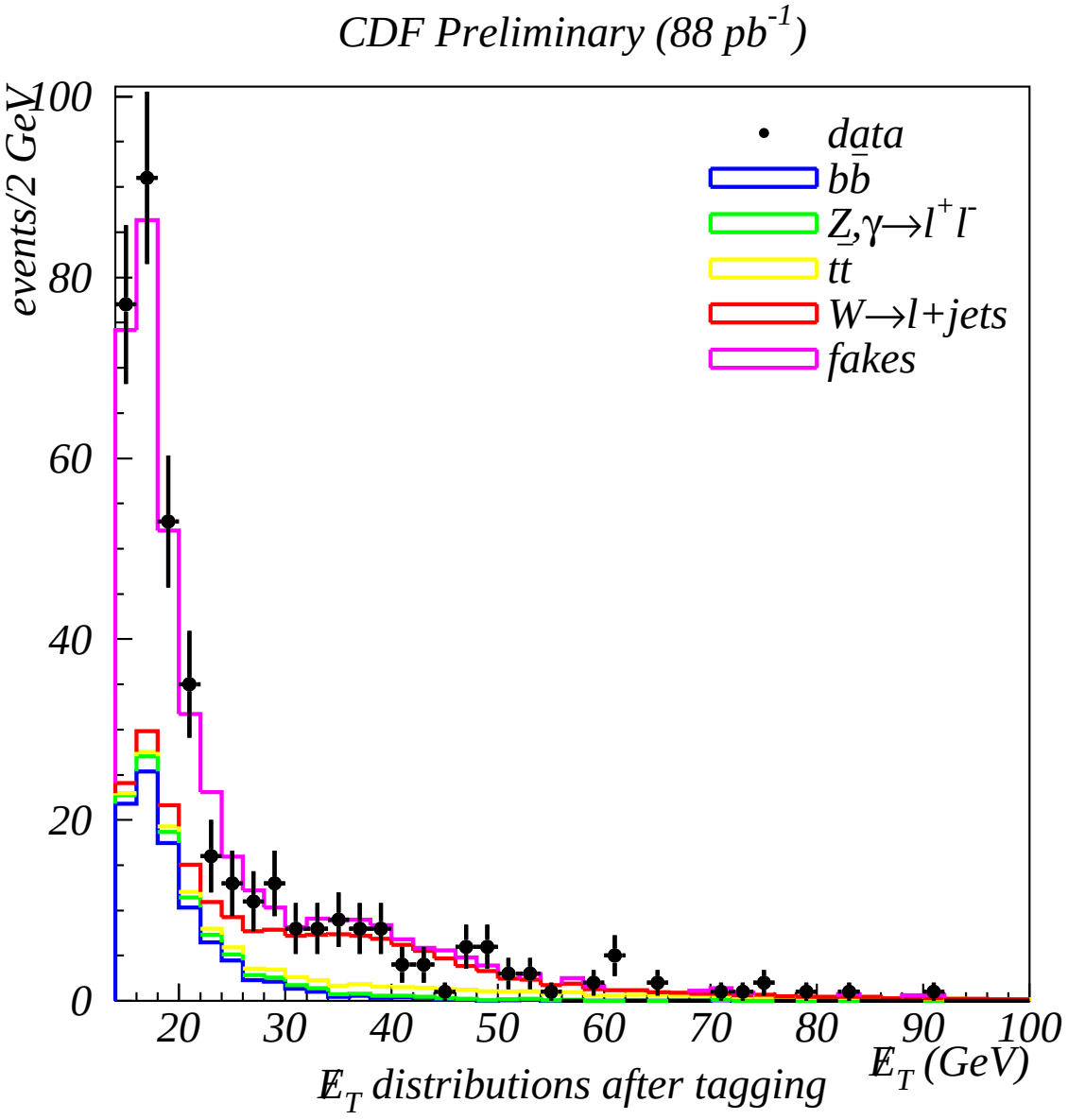

Figure 4.9: Comparison of data to normalized $\not\!\!E_T$ distributions for backgrounds after b-jet tagging.

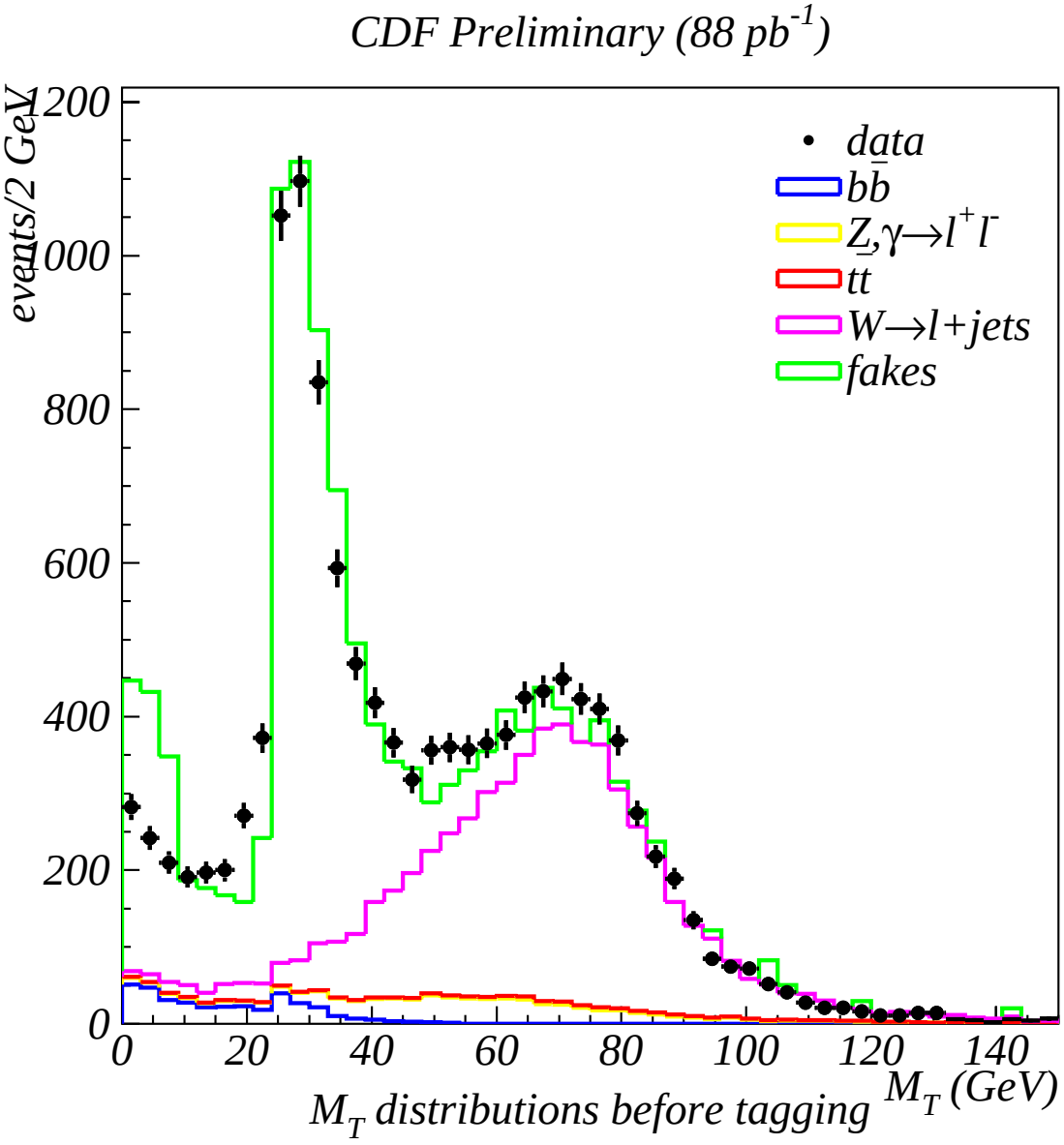

Figure 4.10: Comparison of data to normalized M_T distributions for backgrounds after Z^0/γ event reduction. The fake lepton event distribution shown has a peak at low M_T which is the result of not requiring isolated leptons in the fake lepton sample. If fake leptons are required to be isolated, the peak is greatly reduced, but the sample has low statistics. To correct for this, we normalize the fake lepton event distribution with $M_T > 5$ to the number predicted.

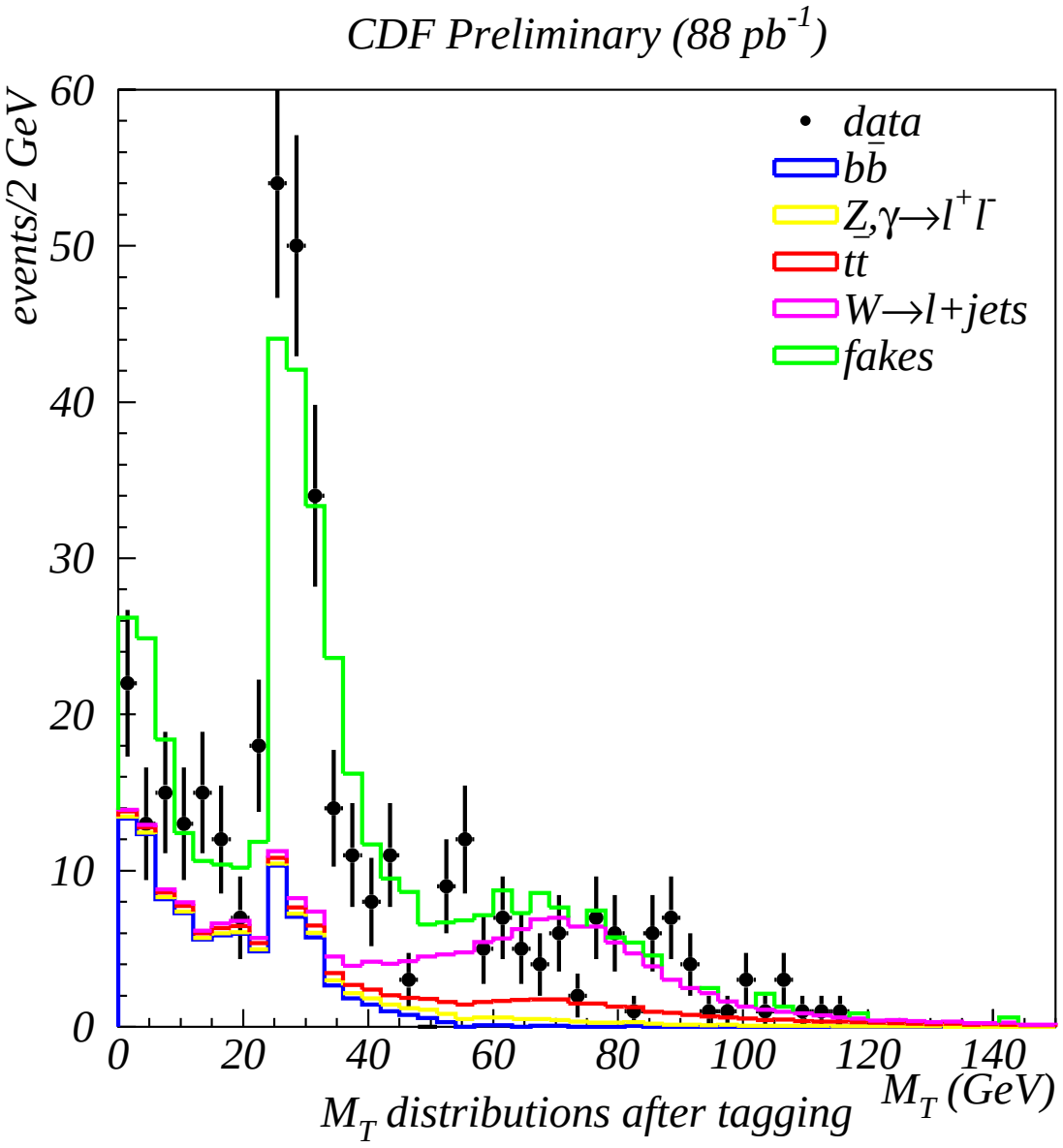

Figure 4.11: Comparison of data to normalized M_T distributions for backgrounds after b-jet tagging. The fake lepton event distribution has been normalized as in Fig. 4.10.

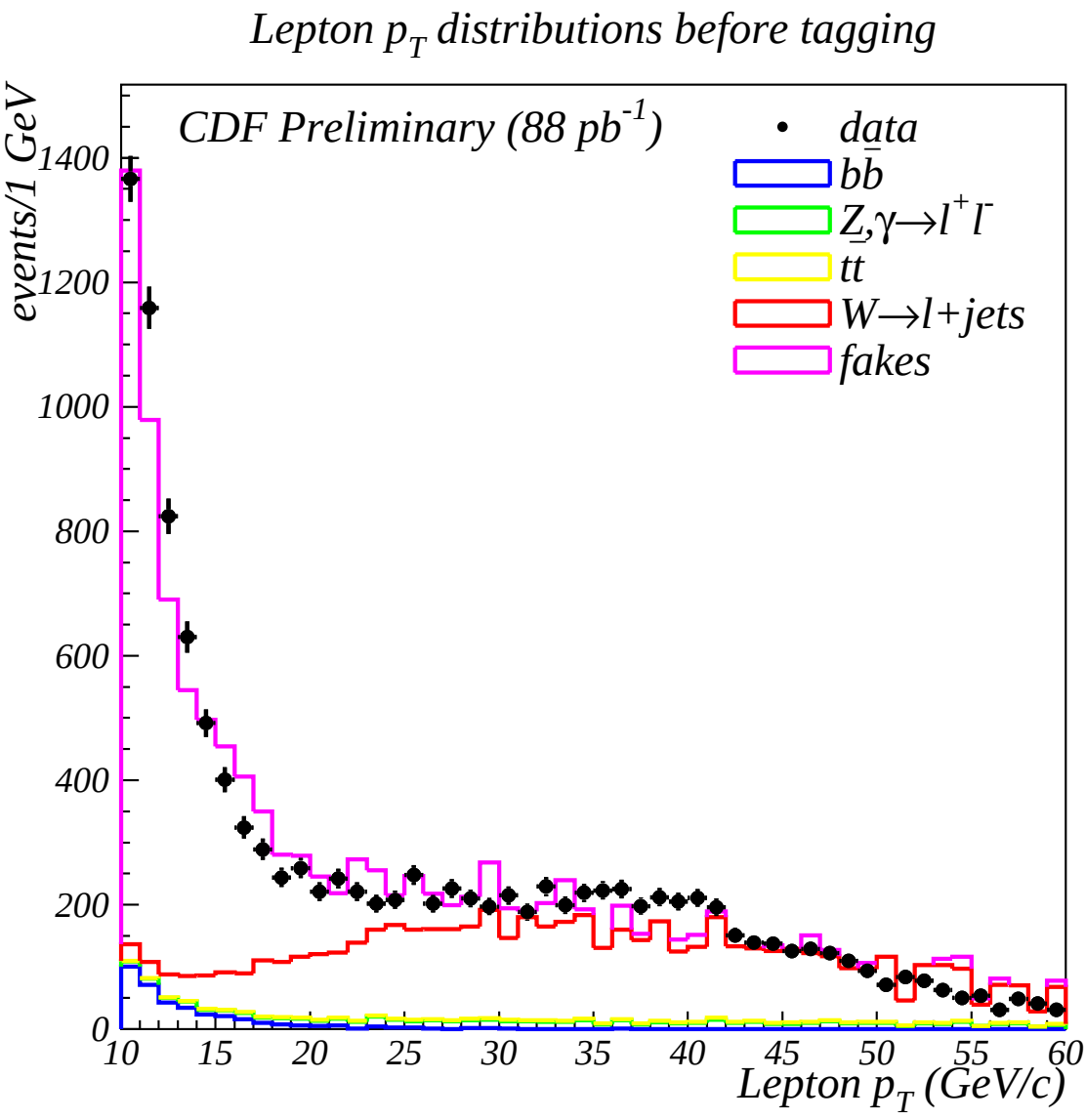

Figure 4.12: Comparison of data to normalized lepton p_T distributions for backgrounds after Z^0/γ event reduction.

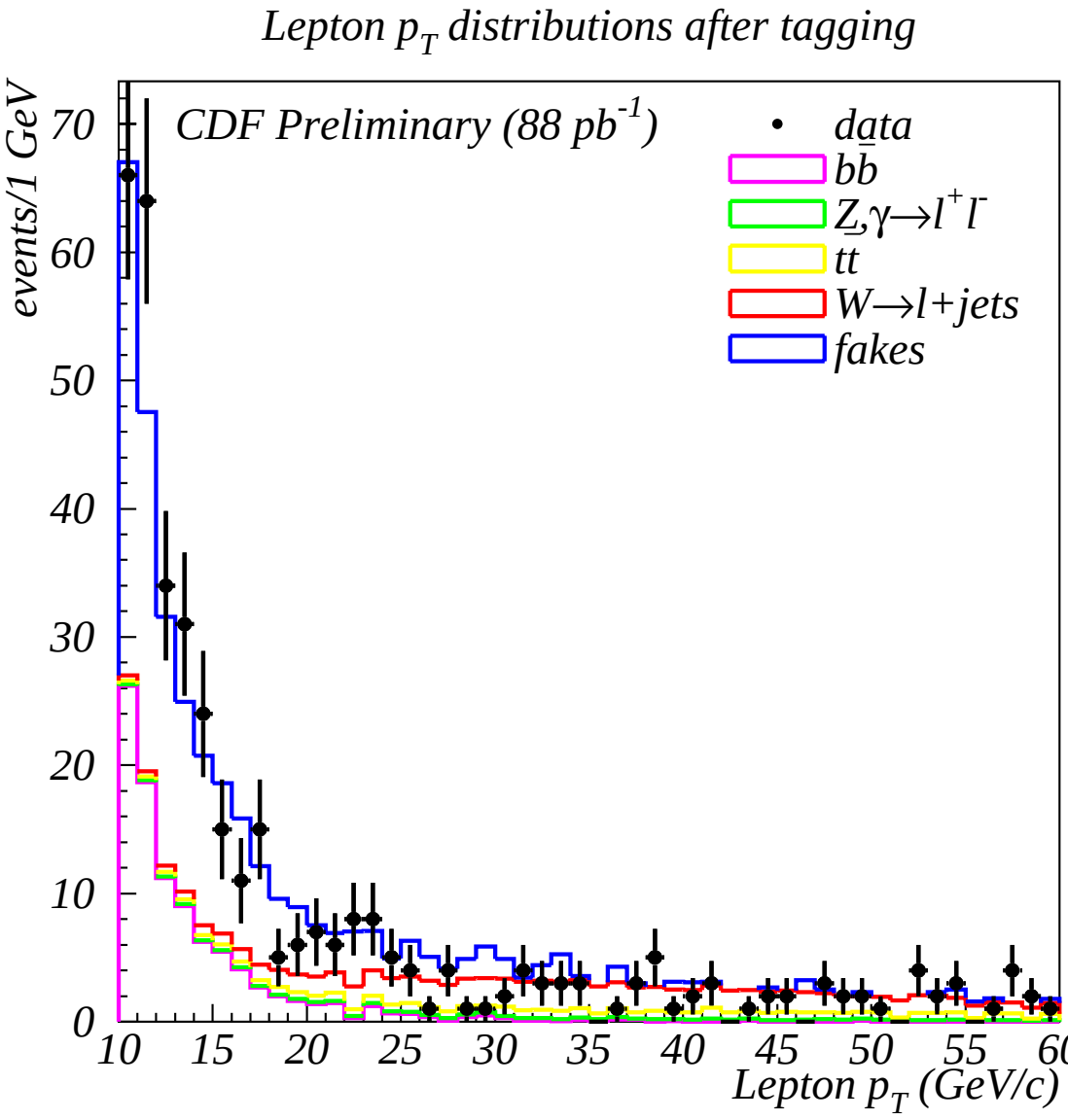

Figure 4.13: Comparison of data to normalized lepton p_T distributions for backgrounds after b-jet tagging.

Chapter 5

Determining the Numbers of Signal Events

After determining that we see no excess in the data compared to our Standard Model background prediction, shown in Table 4.29, we can set upper limits on the number of observed events for our signal as a function of $\tilde{t}_1$ mass. These can be translated in to upper limits on the $\tilde{t}_1\bar{\tilde{t}}_1$ production cross section as a function of $m_{\tilde{t}_1}$ by inverting Eq. 3.1 or Eq. 3.2, depending on the decay scenario. In these equations, we use the cumulative selection efficiencies from Figs. 4.5, 4.6, and 4.7. When calculating upper limits on the cross sections, the statistical and systematic uncertainties on the integrated luminosities and the cumulative efficiencies must be taken into account. The systematic uncertainties are addressed in the following section. After this, we discuss the method used to extract the upper limits on the number of observed signal events.

5.1 Systematic uncertainties

The sources of systematic uncertainties for this analysis are common to most CDF analyses. We list here these sources and the methods we used to estimate their effects.

integrated luminosity The CDF luminosity is calculated using Eq. 2.2 with N equal to the number of BBC interactions and σ equal to the BBC cross section. The errors on this luminosity calculation include effects from the measurement of σ_{BBC}, variations in the calculation from run to run, and variations in the calculation due to changes in the instantaneous luminosity. The total uncertainty in the integrated luminosity is $\pm 4.1\%$ [49].

parton distribution function The geometrical acceptance times stripping efficiency, $(A \times \epsilon_{\rm strip})$, determined from Monte Carlo has a slight dependence on the parton distribution function (PDF) used in event generation. We determined this uncertainty by generating three Monte Carlo signal samples in which only the PDF was varied. The PDF's used were CTEQ3L (used in Tables 4.4 and 4.5), GRV94HO, and MRSG. The uncertainty, defined as the largest fraction difference in $(A \times \epsilon_{\rm strip})$ achieved between the three PDF's, is $\pm 2.6\%$.

initial and final state radiation When a gluon is radiated in either the initial or final state of an interaction, the event kinematics may be affected. The modeling of initial and final state radiation is not well understood in the Monte Carlo. Therefore, we estimate the systematic effects of initial and final state radiation on $(A \times \epsilon_{\rm strip})$ using the method from Ref. [50]. We generated three samples of signal events for a given $\tilde{t}_1$ mass using PYTHIA : (1) both initial and final state radiation on, (2) only initial state radiation on, and (3) all radiation off. The effect from initial state radiation is determined by comparing samples (2) and (3). Similarly, the effect from final state radiation is determined by comparing samples (1) and (3). The equations for computing the uncertainties assume symmetric effects and uniform distributions [50]:

$$\left(\frac{\delta\epsilon}{\epsilon}\right)_{\rm init\ state\ rad} = \frac{2\ |\epsilon_2 - \epsilon_3|}{\sqrt{12}\ \epsilon_1},$$

and

$$\left(\frac{\delta\epsilon}{\epsilon}\right)_{\rm final\ state\ rad} = \frac{2\ |\epsilon_1 - \epsilon_3|}{\sqrt{12}\ \epsilon_1},$$

where the subscript denotes the sample number and ϵ_i is short for $(A \times \epsilon_{\rm strip})_i$. Since we expect initial and final state radiation effects to be dependent on $m_{\tilde{t}_1}$, we repeated this procedure for each mass considered. The uncertainties for each $\tilde{t}_1$ mass are listed in Table 5.1 for $\tilde{t}_1 \to b\tilde{\chi}_1^{\pm}$ and Table 5.2 for $\tilde{t}_1 \to bl\tilde{\nu}$.

trigger efficiencies The overall trigger efficiencies from Monte Carlo, described in detail in Section 4.8, can be summarized as the product of the trigger efficiencies from Levels 1, 2, and 3 as determined by the average lepton p_T of a process. There is a systematic uncertainty in our overall trigger efficiencies due to the uncertainties of the individual Level 1, 2, and 3 trigger efficiencies. We determined this systematic by raising all Level 3 trigger efficiencies by 1σ and determining the new overall trigger efficiency. Then, with the Level 3 efficiencies returned to their normal values, we raised all Level 2 trigger efficiencies by 1σ and determined the new overall trigger efficiency. The differences in overall trigger

efficiencies between normal and raised values for both Level 3 and Level 2 triggers were added in quadrature to get the systematic uncertainty. We repeated this procedure for each $\tilde{t}_1$ mass considered. The results are listed in Table 5.1 for $\tilde{t}_1 \to b\tilde{\chi}_1^{\pm}$ and Table 5.2 for $\tilde{t}_1 \to bl\tilde{\nu}$.

lepton identification and isolation The lepton identification and isolation cut efficiencies for $Z^0 \to l^+l^-$ events are listed in Tables 4.1, 4.2, and 4.3 for both Run 1B and Monte Carlo. We insert the ratios of these Run 1B/Monte Carlo efficiencies into Eq. 4.1 to scale our Monte Carlo results for other processes. The Run 1B/Monte Carlo scale factors for the combined lepton identification and isolation cuts are:

$$\left(\frac{\epsilon^{\mathrm{1B}}}{\epsilon^{\mathrm{QFL'}}}\right)_{\mathrm{ID}} (e^{\pm}) = 0.860 \pm 0.012$$

and

$$\left(\frac{\epsilon^{\mathrm{1B}}}{\epsilon^{\mathrm{QFL'}}}\right)_{\mathrm{ID}} (\mu^{\pm}) = 0.912 \pm 0.011.$$

Their fractional uncertainty on $(A \times \epsilon_{\mathrm{strip}})^{\mathrm{1B}}$ is 1.4%.

SECVTX scale factor The SECVTX tagging efficiency determined from Monte Carlo must also be scaled to reach agreement with measurement. The Monte Carlo efficiency is different from data due to errors in things such as the b lifetime, the b decay branching ratios to charged particles, and the SVX simulation in QFL′. The b tagging efficiency in data was measured using an inclusive electron sample. The resulting scale factor is $\epsilon_{b\ \mathrm{tag}}^{\mathrm{1B}}/\epsilon_{b\ \mathrm{tag}}^{\mathrm{QFL'}} = 1.06 \pm 0.06$ [26], for a 5.7% systematic uncertainty.

jet energy scale The jet energy scale systematic, or the error in the overall calorimetry calibration, was determined using the standard CDF practice of varying the jet energies by ±5% in Monte Carlo and determining the difference in $(A \times \epsilon_{\mathrm{strip}})$. The results are listed in Table 5.1 for $\tilde{t}_1 \to b\tilde{\chi}_1^{\pm}$ and Table 5.2 for $\tilde{t}_1 \to bl\tilde{\nu}$.

underlying events The underlying event systematic takes into account particles produced from the color flow from the initial to the final state. The underlying event systematic primarily effects jet energies. We determine this systematic using the standard CDF practice of turning the underlying event correction on and then off in the jet energy correction routine and taking half the difference. The results are listed in Table 5.1 for $\tilde{t}_1 \to b\tilde{\chi}_1^{\pm}$ and Table 5.2 for $\tilde{t}_1 \to bl\tilde{\nu}$.

The combined systematic uncertainties from all the above sources are listed in Table 5.1 for $\tilde{t}_1 \to b\tilde{\chi}_1^{\pm}$ and Table 5.2 for $\tilde{t}_1 \to bl\tilde{\nu}$.

Table 5.1: Systematic uncertainties for $\tilde{t}_1\bar{\tilde{t}}_1$ in the $\tilde{t}_1 \to b\tilde{\chi}_1^{\pm}$ decay scenario. The error quoted is the fractional change in the geometrical acceptance times efficiency, $(A \times \epsilon_{\rm strip})$. All masses are in GeV/c^2. The total systematic uncertainty includes uncertainties not listed: integrated luminosity, PDF, lepton id, and SECVTX scale factor. We note that the underlying event systematic is inversely proportional to $m_{\tilde{t}_1}$. Since the b jet energy is proportional to $m_{\tilde{t}_1}$, the jet requirement gets less efficient for lighter $m_{\tilde{t}_1}$ and is more sensitive to calorimeter activity created by underlying events.

			fractional uncertainties						
$m_{\tilde{t}_1}$	$m_{\tilde{\chi}_1^{\pm}}$	$m_{\tilde{\chi}_1^0}$	initial state radiation	final state radiation	trigger ($e^{\pm}$)	trigger ($\mu^{\pm}$)	underlying event	jet E_T	total
100	90	40	±1.56%	±3.16%	±2.01%	±6.05%	±6.2%	±5.1%	±13%
110	90	40	±2.17%	±1.47%	±1.94%	±5.58%	±2.5%	±2.2%	±11%
115	90	40	±1.39%	±2.33%	±1.95%	±5.56%	±1.7%	±1.5%	±10%
120	90	40	±0.70%	±3.73%	±1.91%	±5.44%	±1.3%	±1.1%	±10%

Table 5.2: Systematic uncertainties for $\tilde{t}_1\bar{\tilde{t}}_1$ in the $\tilde{t}_1 \to bl\tilde{\nu}$ decay scenario. The error quoted is the fractional change in the geometrical acceptance times efficiency, $(A \times \epsilon_{\rm strip})$. All masses are in GeV/c^2. The total systematic uncertainty includes uncertainties not listed: integrated luminosity, PDF, lepton id, and SECVTX scale factor. We use the uncertainties for $m_{\tilde{t}_1}$= 120 GeV/c^2 for all higher masses investigated in this decay scenario.

		fractional uncertainties						
$m_{\tilde{t}_1}$	$m_{\tilde{\nu}}$	initial state radiation	final state radiation	trigger ($e^{\pm}$)	trigger ($\mu^{\pm}$)	underlying event	jet E_T	total
80	40	±5.3%	±4.0%	±1.8%	±4.4%	±2.2%	±2.4%	±12%
90	40	±3.7%	±4.6%	±1.8%	±4.5%	±1.9%	±1.7%	±11%
100	40	±1.7%	±1.4%	±1.9%	±4.6%	±1.7%	±1.1%	±10%
110	40	±2.2%	±1.8%	±1.8%	±4.8%	±1.3%	±0.9%	±10%
120	40	±2.2%	±3.1%	±1.8%	±4.8%	±1.0%	±0.6%	±10%
80	50	±7.0%	±1.0%	±1.8%	±4.6%	±3.0%	±2.6%	±12%
90	50	±3.9%	±2.4%	±1.8%	±4.5%	±2.6%	±1.8%	±11%
100	50	±3.6%	±2.5%	±1.8%	±4.5%	±1.7%	±1.3%	±10%
110	50	±2.1%	±2.3%	±1.8%	±4.6%	±1.2%	±1.1%	±10%
120	50	±1.6%	±2.9%	±1.7%	±4.7%	±0.9%	±0.8%	±10%

5.2 Unbinned likelihood fit

The number of events in our final data sample is listed in Table 4.29 along with the expected Standard Model contributions. We determined the 95% C.L. upper limit on the number of signal events in this sample for a Poisson counting experiment in which the number of observed events, the expected number of background events, and their errors are included in the counting [51]. We calculate the 95% C.L. upper limit with this method to be 34.7 $\tilde{t}_1\bar{\tilde{t}}_1$ events.

To achieve a better limit, we took advantage of the shape differences between signal and background kinematic distributions by performing an unbinned maximum likelihood fit to one (or two) of these distributions. The list of potential fitting distributions includes:

- H_T (the sum of lepton E_T, $\not\!\!E_T$, and jet E_T for all jets passing jet2 strip cuts),
- M_T (the invariant mass reconstructed by the lepton and $\not\!\!E_T$),
- jet multiplicity,
- $\Delta\phi$(jet1,jet2) (the ϕ difference between the two highest E_T jets),
- $\Delta\phi$(lepton,$\not\!\!E_T$),
- lepton $p_T^{\rm rel}$ (the momentum of the lepton transverse to the direction of the nearest of the two leading jets),
- and lepton p_T.

These distributions are shown in Figs. 5.1 through 5.7 for signal ($\tilde{t}_1 \to b\tilde{\chi}_1^{\pm}$) and three significant backgrounds, $b\bar{b}$, $t\bar{t}$, and $W^{\pm} \to e(\mu)^{\pm}\nu$ + jets.

When narrowing the list of distributions to consider for the fit, we needed to reduce, as much as possible, the number of background processes input to the fitting routine from the ten listed in Table 4.29. One way to do this was to simply ignore the less significant contributors. Another way is to attempt to represent a combination of processes with the same fitting distribution such that the fit value returned would be the sum of these processes.

We observed that most of the $b\bar{b}$ potential fitting distributions are very similar to those from fake lepton events (see Fig. 5.8). In fact, we expect the fake lepton event sample to be dominated by b quark events after b jet tagging. The only fake lepton event distribution that does not closely resemble $b\bar{b}$ is the $\Delta\phi$(lepton,$\not\!\!E_T$) distribution. The statistics in the M_T distribution for fake lepton events are too low to be reliable, so no comparison between $b\bar{b}$ and fake lepton events could be made for it. Therefore,

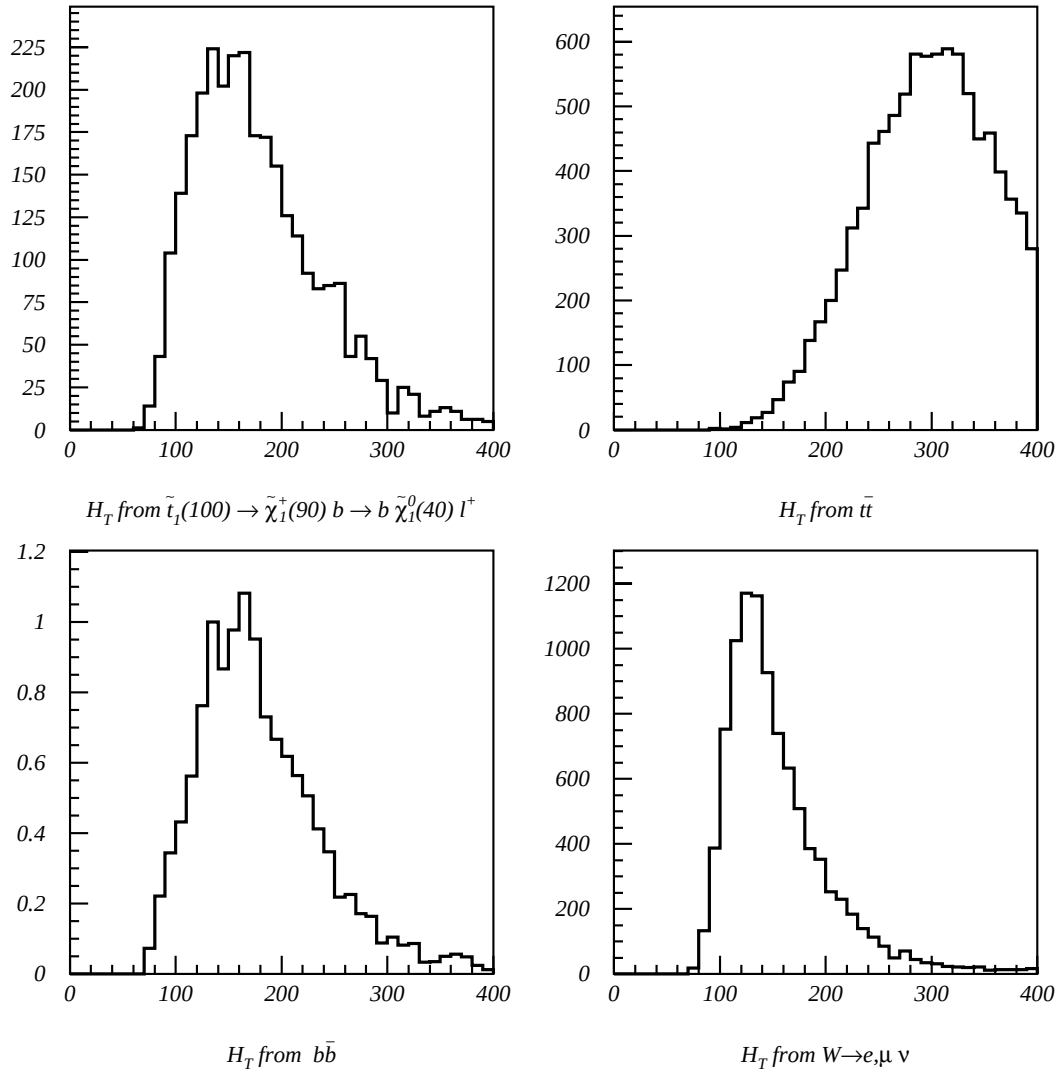

Figure 5.1: H_T distributions for $\tilde{t}_1$ of mass 100 GeV/c^2 and three significant remaining backgrounds (see Table 4.29) after signal selection.

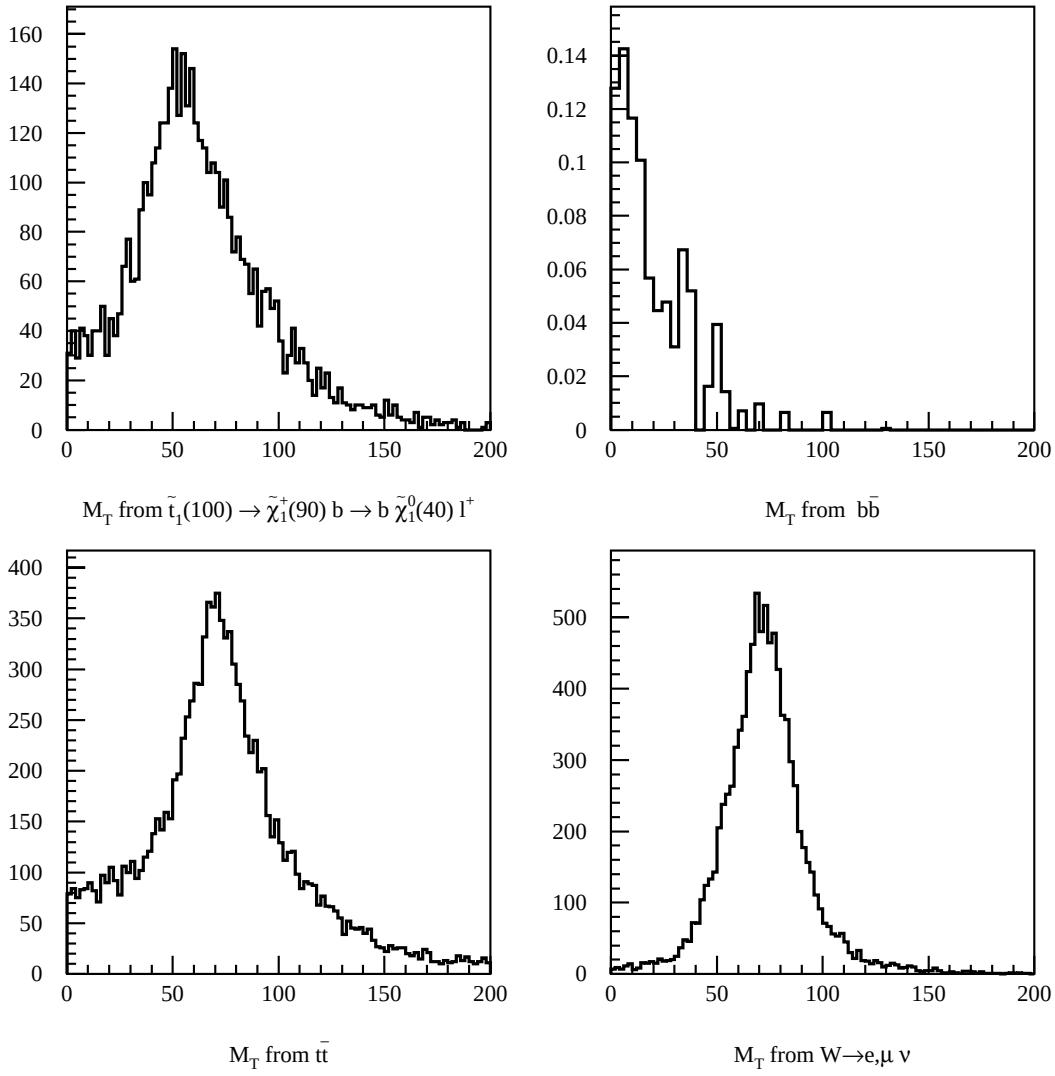

Figure 5.2: M_T distributions for $\tilde{t}_1$ of mass 100 GeV/c^2 and three significant remaining backgrounds (see Table 4.29) after signal selection.

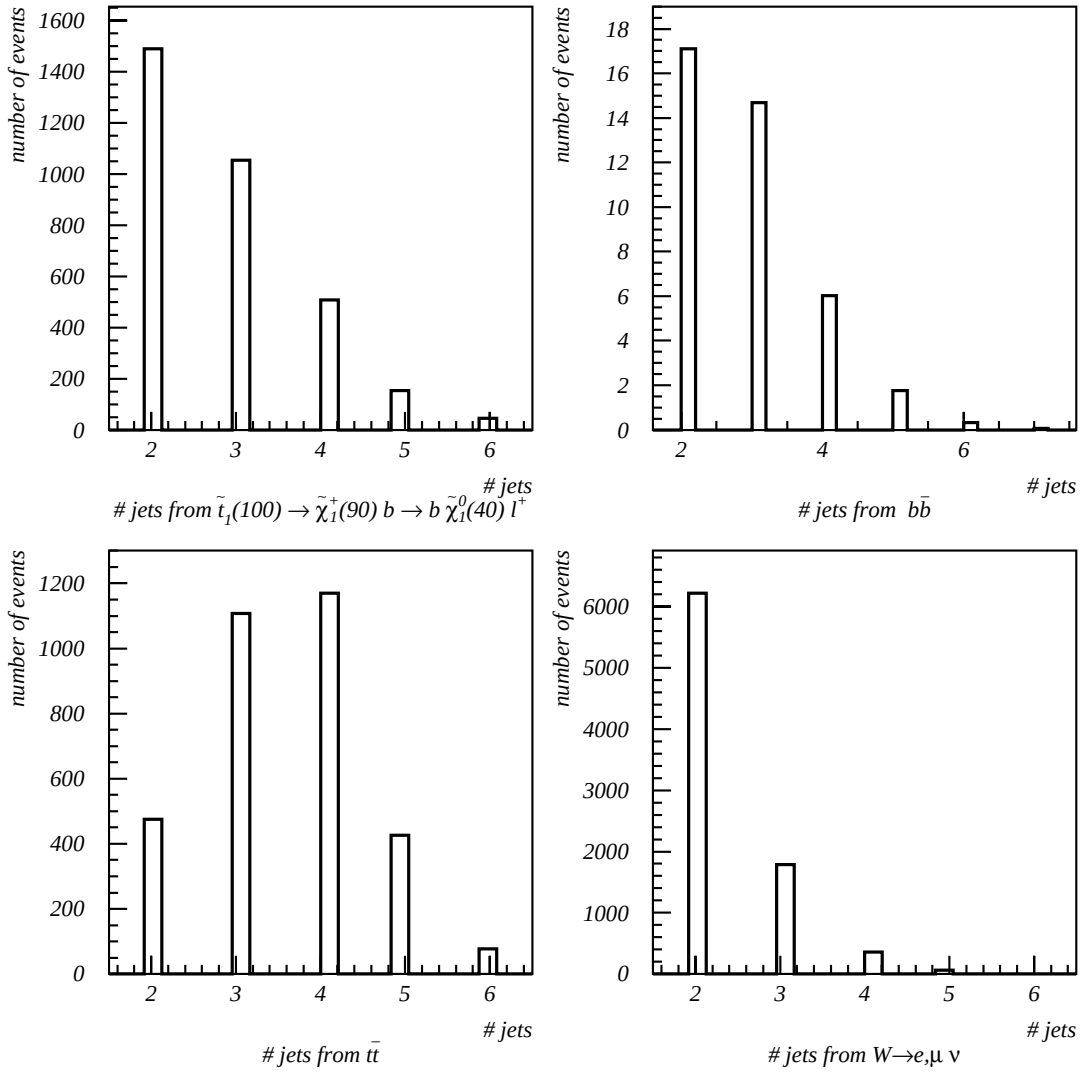

Figure 5.3: Jet multiplicity distributions for $\tilde{t}_1$ of mass 100 GeV/c^2 and three significant remaining backgrounds (see Table 4.29) after signal selection.

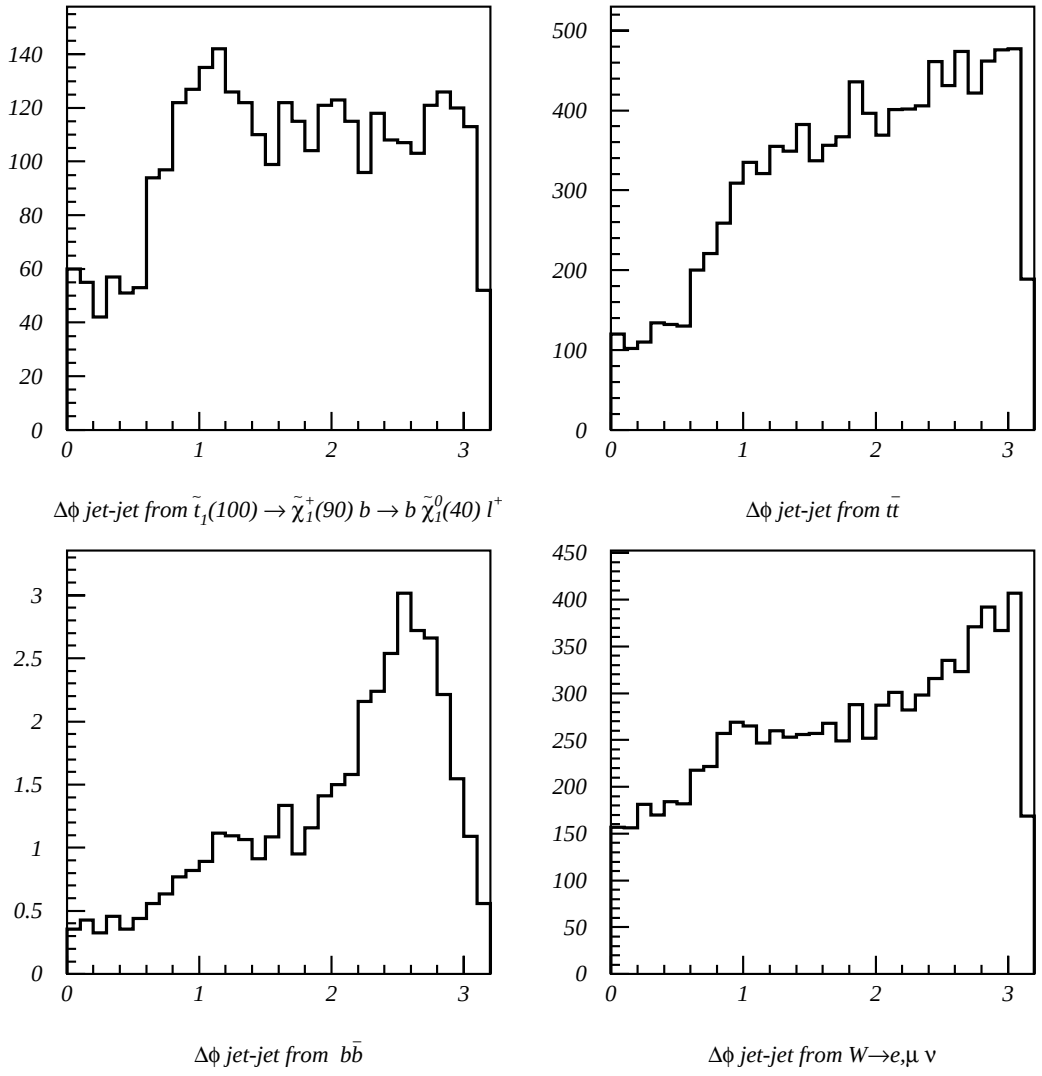

Figure 5.4: $\Delta\phi$(jet1,jet2) distributions for $\tilde{t}_1$ and three significant remaining backgrounds (see Table 4.29) after signal selection.

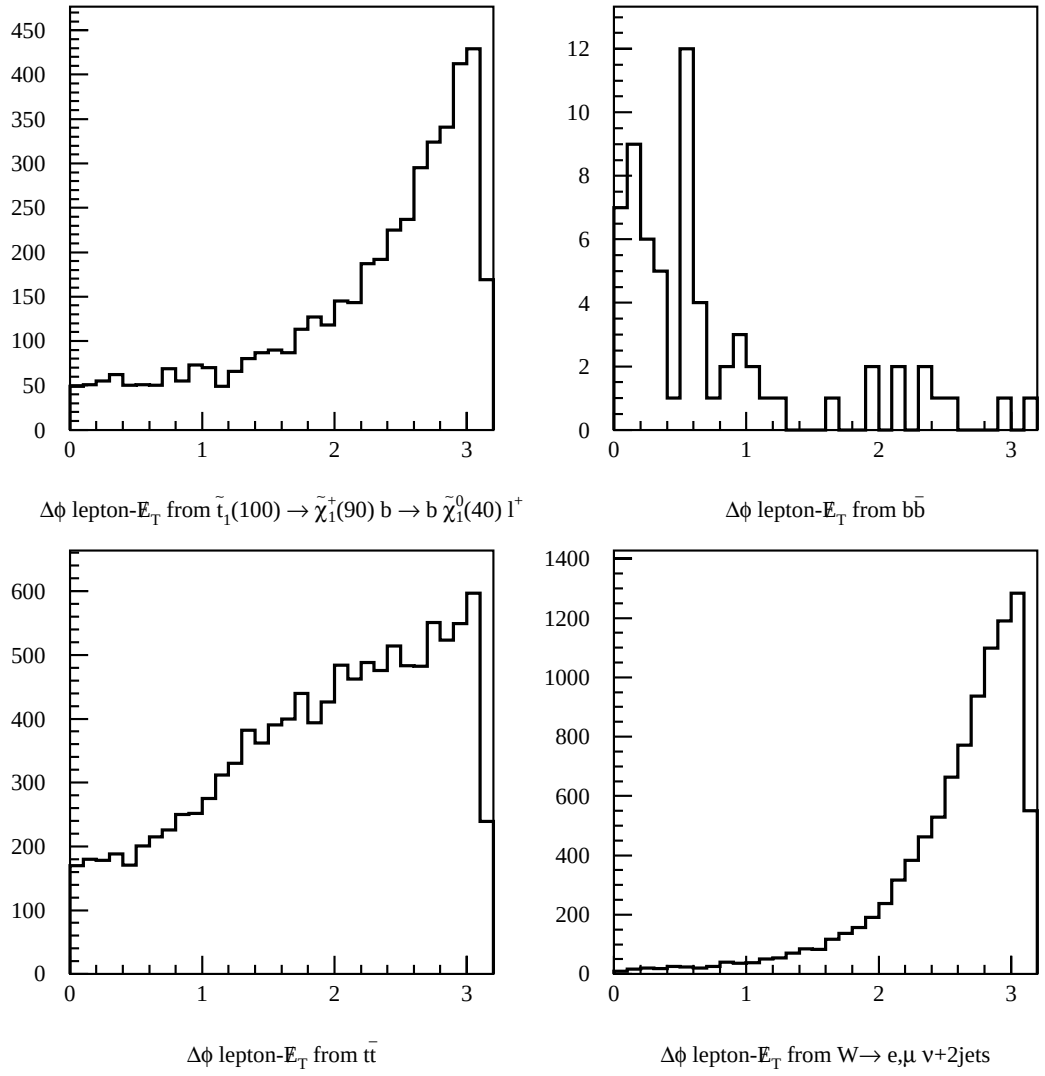

Figure 5.5: $\Delta\phi(\text{lepton},\not\!\!E_T)$ distributions for $\tilde{t}_1$ and three significant remaining backgrounds (see Table 4.29) after signal selection.

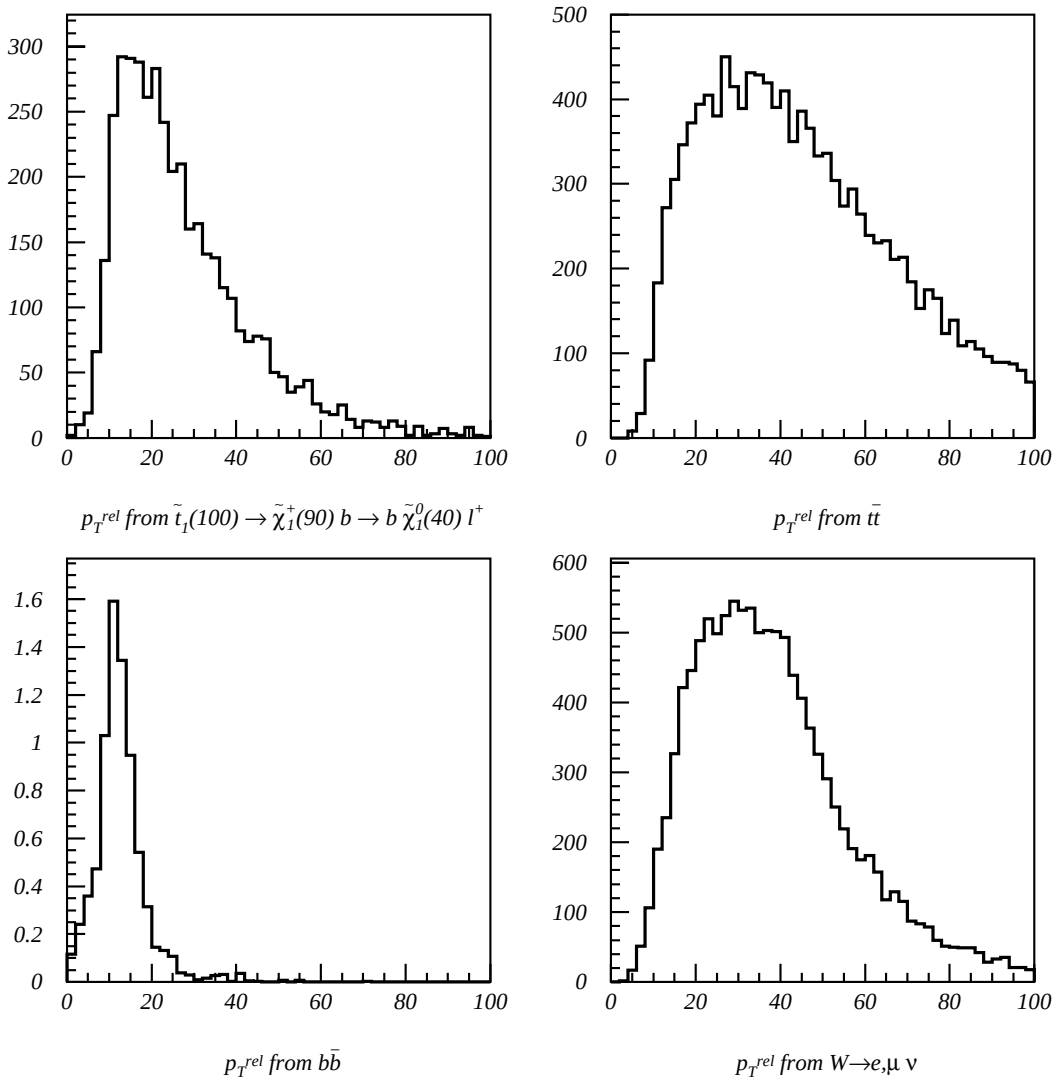

Figure 5.6: Lepton $p_T^{\rm rel}$ distributions for $\tilde{t}_1$ and three significant remaining backgrounds (see Table 4.29) after signal selection.

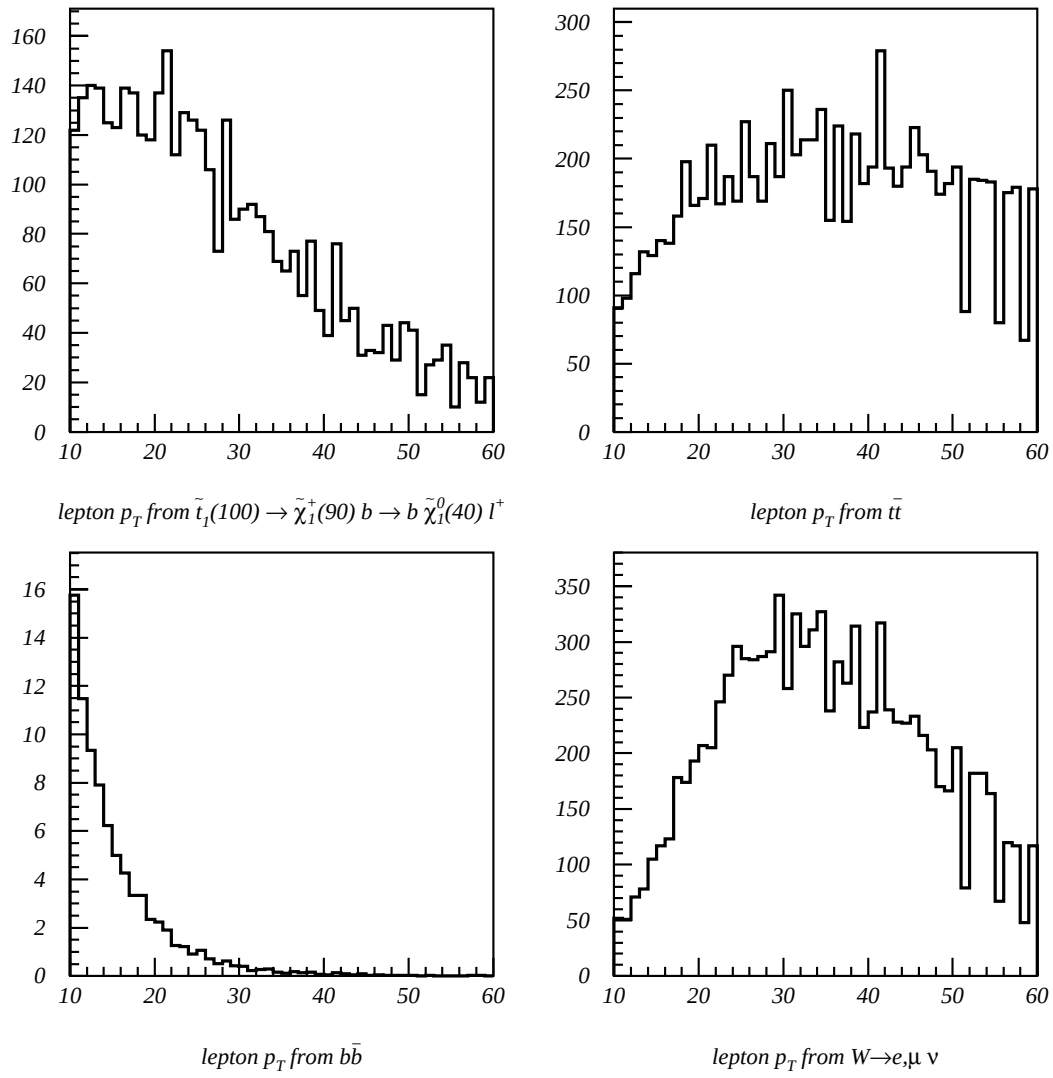

Figure 5.7: Lepton p_T distributions for $\tilde{t}_1$ and three significant remaining backgrounds (see Table 4.29) after signal selection.

we eliminated $\Delta\phi$(lepton,$\not\!\!E_T$) and M_T from the list of potential fitting distributions in order to combine the predicted numbers of $b\overline{b}$ and fake lepton events for fitting.

Rather than disregard the small contributions to the data from $Z \to e^+e^-(\mu^+\mu^-)$ and $W^\pm \to \tau^\pm$, we checked the feasibility of combining them with $W^\pm \to e(\mu)^\pm\nu$ for fitting. Ignoring the distributions ruled out by the $b\overline{b}$ and fake lepton event combination, we compared the other potential fitting distributions for $W^\pm \to e(\mu)^\pm\nu$, $Z \to e^+e^-(\mu^+\mu^-)$, and $W^\pm \to \tau^\pm$, shown in Figs. 5.9 and 5.10. The agreement between $W^\pm \to \tau^\pm\nu$ and $W^\pm \to e(\mu)^\pm$ is good for all but the lepton distributions. The $Z \to e^+e^-(\mu^+\mu^-)$ and $W^\pm \to e(\mu)^\pm\nu$ agreement is better for leptons, but worse for jet multiplicity. We concluded that the agreement is reasonable considering the small additional contributions from $Z \to e^+e^-(\mu^+\mu^-)$ and $W^\pm \to \tau^\pm$, and no further fitting distributions were eliminated from the list.

The remaining potential fitting distributions were

- H_T,
- jet multiplicity,
- $\Delta\phi$(jet1,jet2),
- lepton $p_T^{\rm rel}$,
- and lepton p_T,

and the fitted background processes were $b\overline{b}$, $t\overline{t}$, and $W^\pm \to e(\mu)^\pm\nu$ + jets. The fitting distributions for signal versus these combined, normalized backgrounds are shown in Figs. 5.11 and 5.12.

To decide which of these distributions had the best signal sensitivity, we used the Kolmogorov statistic. The Kolmogorov statistic is the maximum value of the absolute difference between two cumulative distribution functions. Therefore, we are interested in distributions which give the largest Kolmogorov statistic between signal and the combined backgrounds. (We combine the backgrounds according to their predicted values in Table 4.29, with fake lepton events included in the $b\overline{b}$ normalization and all vector bosons included in the $W^\pm \to e(\mu)^\pm\nu$ normalization.) Table 5.3 shows the Kolmogorov statistic between $\tilde{t}_1 \to b\tilde{\chi}_1^\pm$ and combined backgrounds for H_T, jet multiplicity, lepton p_T, $\Delta\phi$(jet1-jet2), and lepton p_T^{rel}. Table 5.4 shows the Kolmogorov statistic between $\tilde{t}_1 \to bl\tilde{\nu}$ and combined backgrounds for the same distributions. We found best fitting distribution overall is H_T.[1] However, to improve

[1]For $m_{\tilde{t}_1}$ <100 GeV/c^2 in the $\tilde{t}_1 \to bl\tilde{\nu}$ decay scenario, lepton p_T or p_T^{rel} are more discriminating than H_T. However, since LEP2 has excluded most of the region below $m_{\tilde{t}_1}$ =100 GeV/c^2, we concluded that H_T is the best fitting choice.

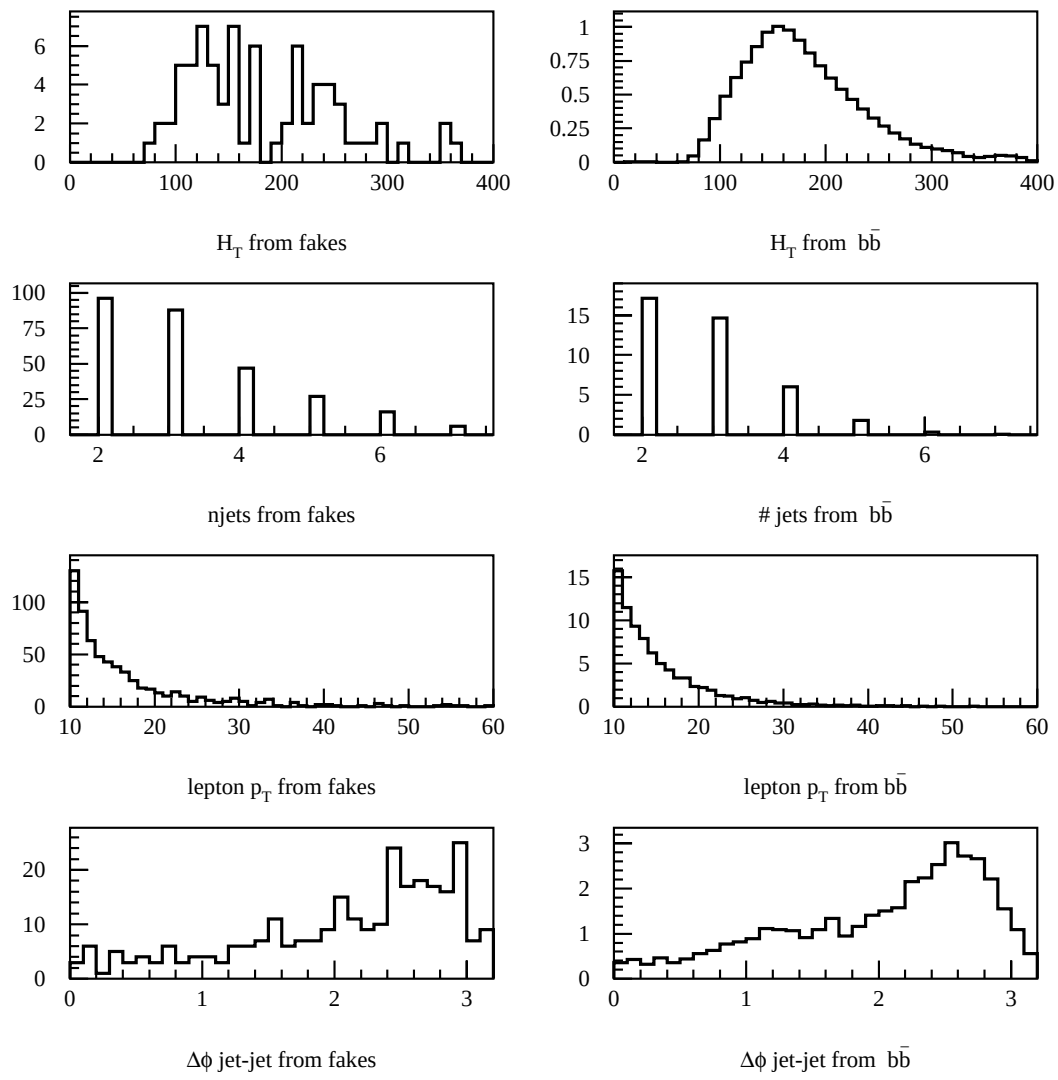

Figure 5.8: Comparison of H_T, jet multiplicity, lepton p_T, and $\Delta\phi$(jet1,jet2) distributions for $b\overline{b}$ and fake lepton events. All fitting distributions for $b\overline{b}$ and fake lepton events are similar. Therefore, the $b\overline{b}$ distributions are used for both in the fit.

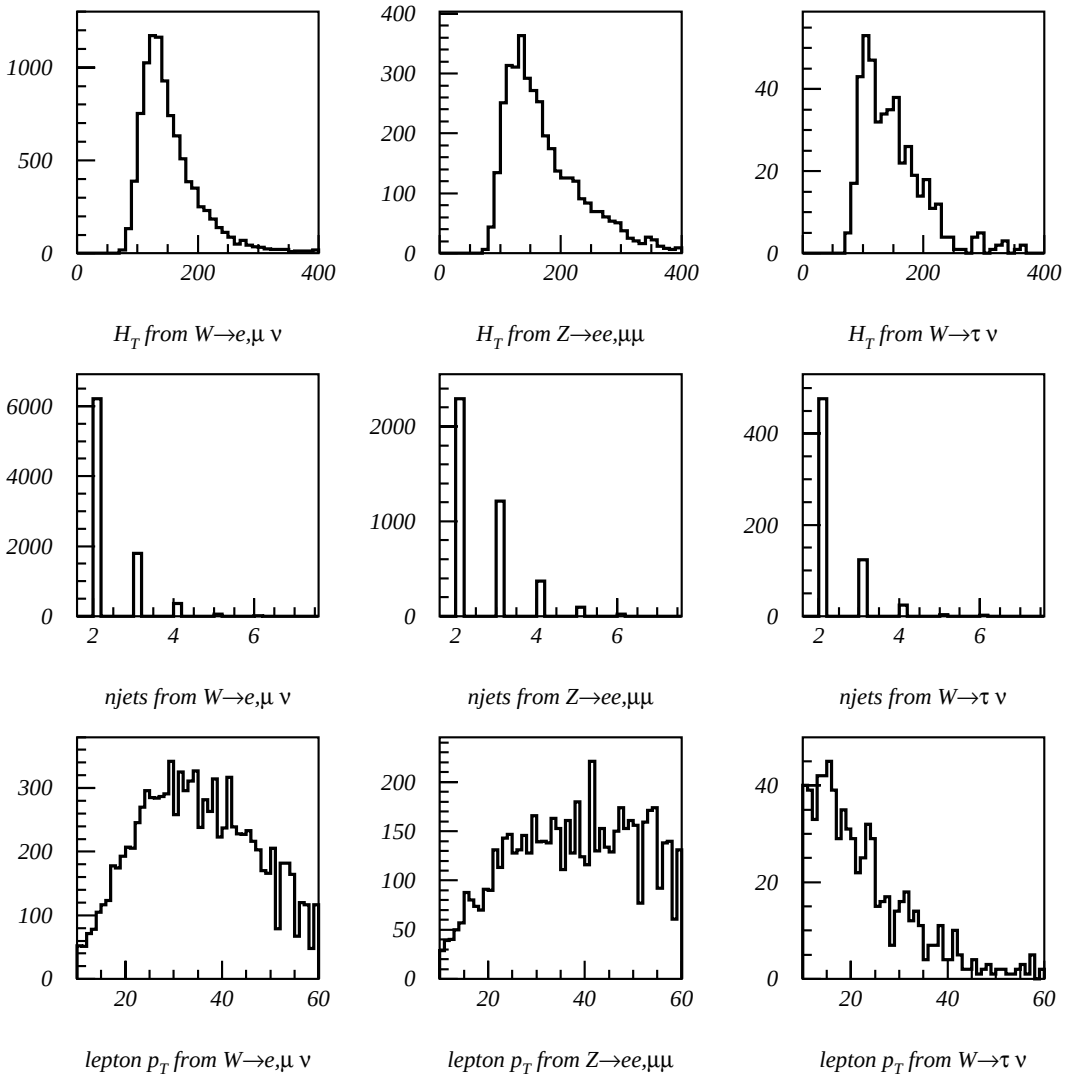

Figure 5.9: Comparison of H_T, jet multiplicity, and lepton p_T distributions for W and Z. Distributions are similar and are combined for fitting.

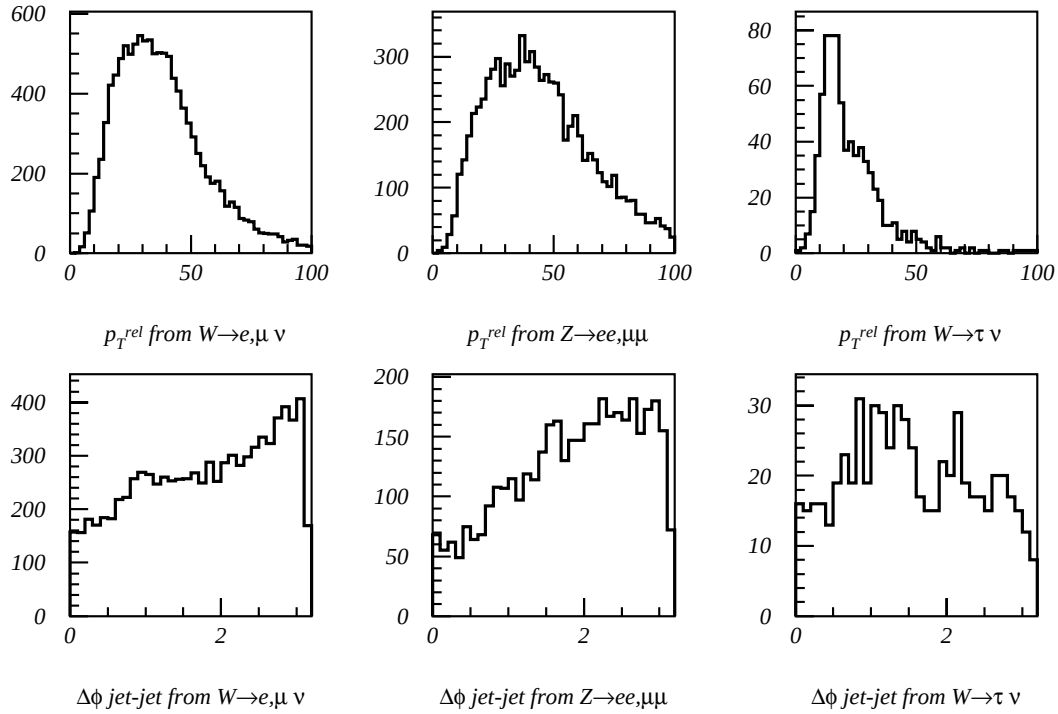

Figure 5.10: Comparison of $\Delta\phi$ (jet1-jet2) and lepton $p_T^{\rm rel}$ distributions for W and Z. Distributions are similar and are combined for fitting.

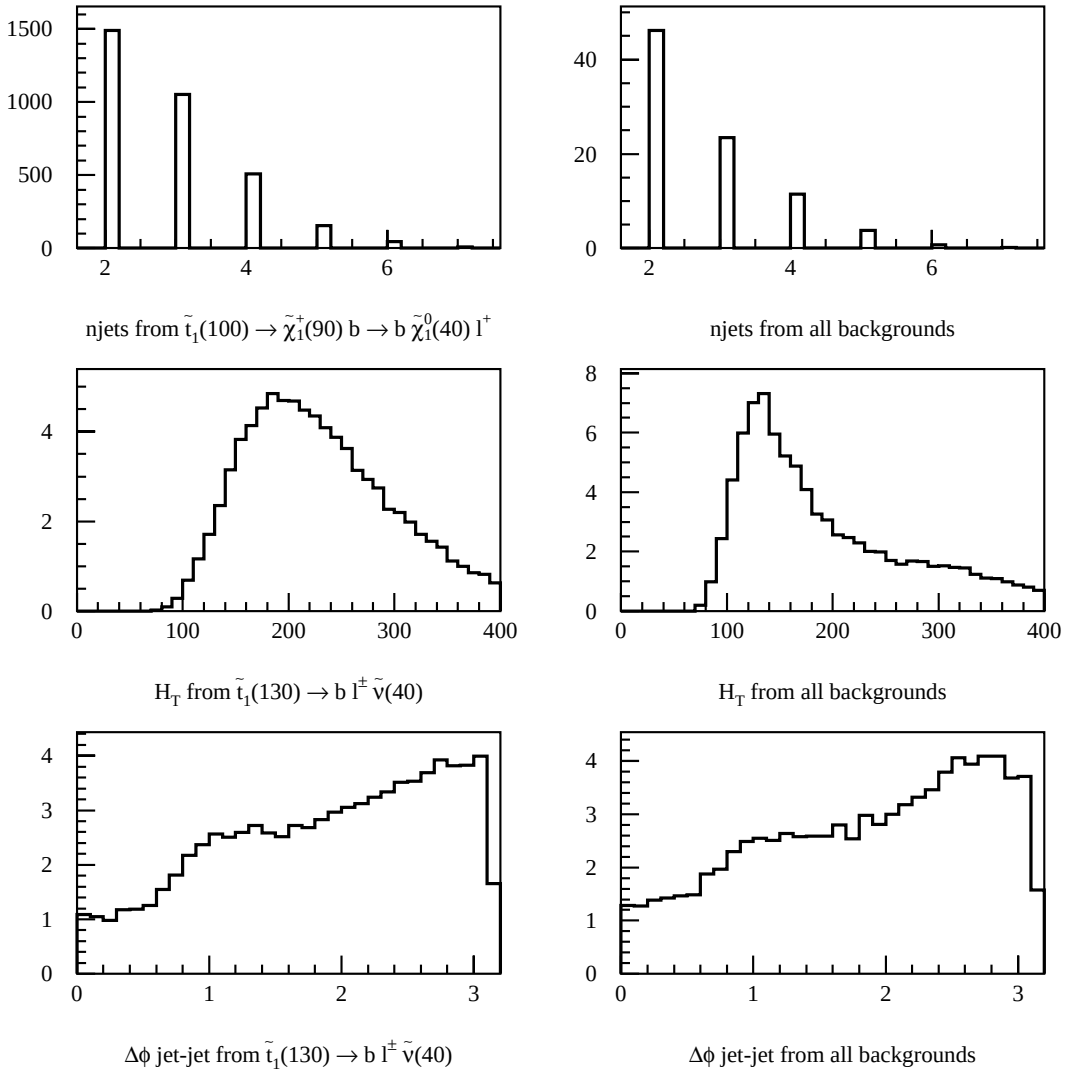

Figure 5.11: Comparison of signal and combined normalized background distributions (top, bottom, and W) after signal selection. Shown are jet multiplicity, H_T, and $\Delta\phi$(jet1,jet2).

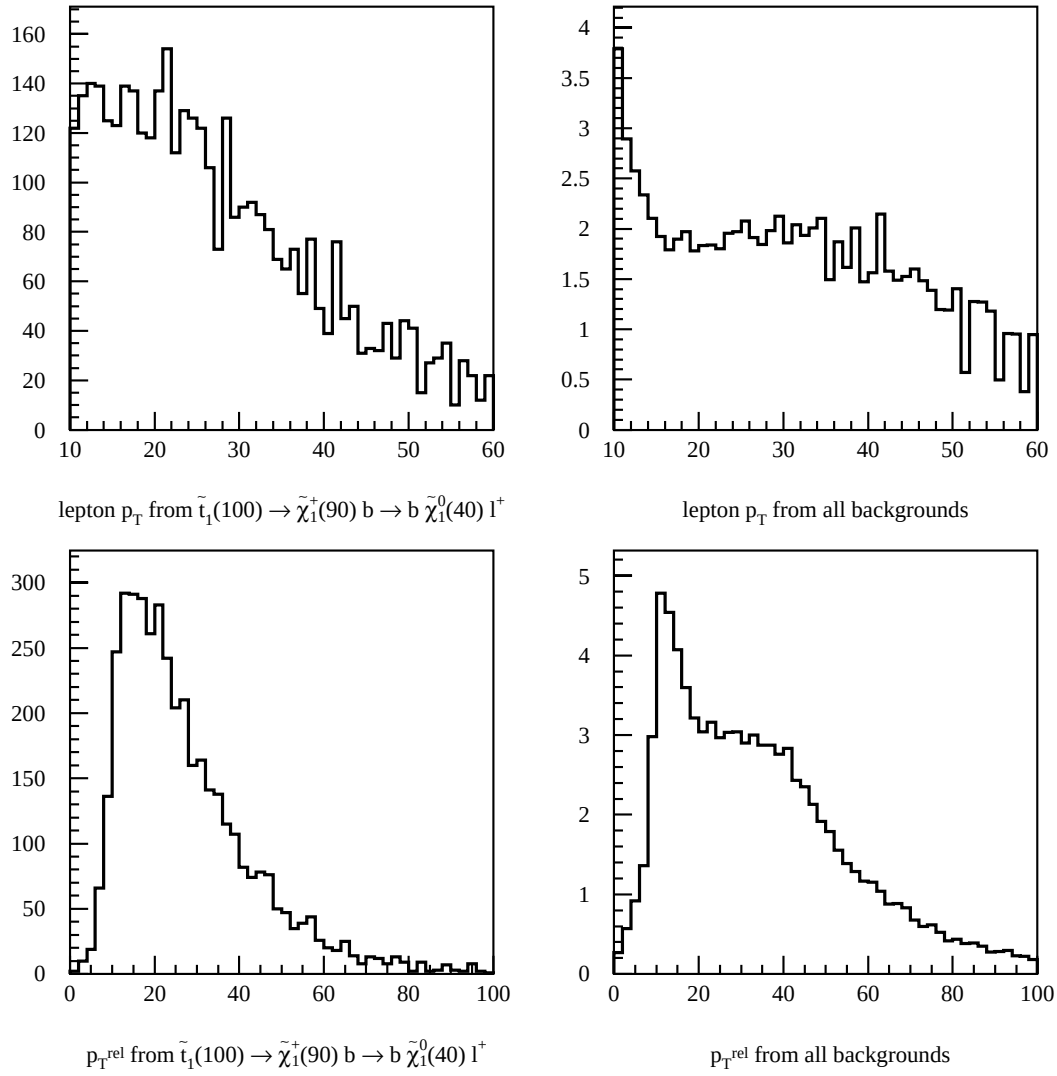

Figure 5.12: Comparison of signal and combined normalized background distributions (top, bottom, and W) after signal selection. Shown are lepton p_T and $p_T^{\rm rel}$.

our sensitivity between signal and $b\overline{b}$ specifically, since the $b\overline{b}$ H_T distribution most closely resembles signal, we looked at performing a two dimensional likelihood fit to the product of the H_T distribution and another, uncorrelated distribution. The only fitting distribution uncorrelated to H_T is an angular distribution, of which only $\Delta\phi$(jet1,jet2) remains. The Kolmogorov statistic between $\tilde{t}_1 \to b\tilde{\chi}_1^{\pm}$ and $b\overline{b}$ is low for H_T (0.04), but good for $\Delta\phi$(jet1,jet2) at 0.20, so we performed a two dimensional likelihood fit to H_T and $\Delta\phi$(jet1,jet2) for $\tilde{t}_1 \to b\tilde{\chi}_1^{\pm}$. However, the Kolmogorov statistic between $\tilde{t}_1 \to bl\tilde{\nu}$ and $b\overline{b}$ is *good* for H_T (0.233), but not for $\Delta\phi$(jet1,jet2) (0.095), so a one dimensional fit is used for $\tilde{t}_1 \to bl\tilde{\nu}$.

Table 5.3: Kolmogorov statistic between $\tilde{t}_1 \to b\tilde{\chi}_1^{\pm}$ (with $m_{\tilde{t}_1} = 100$) and combined backgrounds for the potential fitting distributions.

fitting distribution	Kolmogorov statistic
H_T	0.304
jet multiplicity	0.082
$\Delta\phi$(jet1,jet2)	0.020
lepton p_T^{rel}	0.180
lepton p_T	0.144

Table 5.4: Kolmogorov statistic between $\tilde{t}_1 \to bl\tilde{\nu}$ (with $m_{\tilde{t}_1} = 120$) and combined backgrounds for the potential fitting distributions.

fitting distribution	Kolmogorov statistic
H_T	0.235
jet multiplicity	0.155
$\Delta\phi$(jet1,jet2)	0.026
lepton p_T^{rel}	0.088
lepton p_T	0.052

The likelihood equation that we maximize in the unbinned fits to H_T or H_T and $\Delta\phi$(jet1,jet2) is

$$\begin{aligned}\mathcal{L}(N_{\tilde{t}_1}, N_t, N_W, N_b) &= \left(\prod_{i=1}^{N_{obs}} \frac{N_{\tilde{t}_1} f_{\tilde{t}_1}(x_i) + N_t f_t(x_i) + N_W f_W(x_i) + N_b f_b(x_i)}{N_{\rm TOT}}\right) \\ &\times \exp\left(\frac{-(N_{\rm TOT} - N_{obs})^2}{2N_{obs}}\right) \exp\left(\frac{-(N_t - \overline{N_t})^2}{2\sigma_t^2}\right) \\ &\times \exp\left(\frac{-(N_W - \overline{N_W})^2}{2\sigma_W^2}\right) \exp\left(\frac{-(N_b - \overline{N_b})^2}{2\sigma_b^2}\right)\end{aligned}$$

where the N_a ($a = t, \tilde{t}_1, b, W$) are the numbers of events returned from the fit, $N_{\rm TOT} = N_{\tilde{t}_1} + N_t + N_W + N_b$, x_i is the value of the kinematic variable for the ith event, and the $f_a(x)$ are the fitting distributions. To improve the fit we include the Gaussian constraints on the numbers of backgrounds to be consistent with their predicted means from Table 4.29 and $N_{\rm TOT}$ to be consistent with the number of observed events, N_{obs}. We used the CERN library routine HSMOOF [52] to smooth the H_T distributions prior to fitting, to minimize the effects of statistical fluctuations among adjacent histogram bins. The original and smoothed H_T distributions for signal ($\tilde{t}_1 \to bl\tilde{\nu}$) and backgrounds are shown in Fig. 5.13. In the method of maximum likelihood we maximize this probability distribution, or minimize the negative log likelihood function,

$$-\frac{\partial \ln \mathcal{L}}{\partial N_a} = 0. \tag{5.1}$$

To find a solution to Eq. 5.1, we used the CERN library program MINUIT [53].

To verify that our fitting routine was functioning properly, we performed a pull. For a pull, a large number of simulated data sets, or pseudo-experiments, are created and then processed by the fitting routine so that the performance of the fitter on average may be evaluated. Our simulated data sets were created from the fitting distributions for signal, $t\bar{t}$, $b\bar{b}$, and W. The number of events input for each background process was taken from a Poisson random number generator with mean equal to the number of expected events from Table 4.24. We included signal in these data sets to verify that we are sensitive to its presence. The number of signal events input was taken from a Poisson random number generator with mean equal to 10.

For each pseudo-experiment, we performed the fit and calculated the appropriate pull equation:

$$\text{pull} = \frac{N_s^{\rm fit} - \overline{N}_s}{\Delta N_s}, \tag{5.2}$$

where $N_s^{\rm fit}$ is the number of signal events returned from the fit, $\overline{N}_s$ is the mean number of signal events input into the Poisson random number generator, and ΔN_s

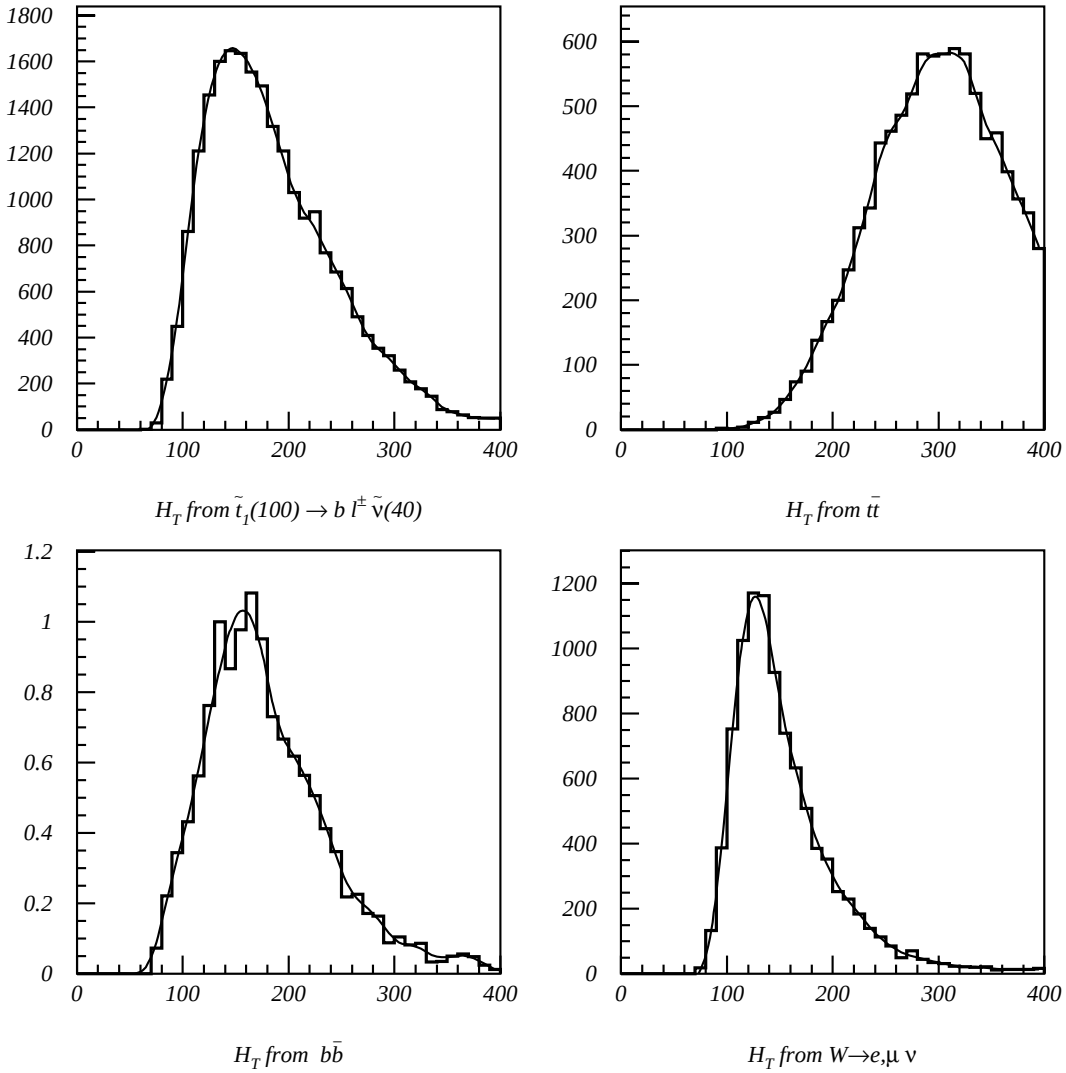

Figure 5.13: H_T distributions for $\tilde{t}_1 \to bl\tilde{\nu}$ ($m_{\tilde{t}_1} = 100$ GeV/c^2) and remaining backgrounds after signal selection. The smooth line superimposed on each histogram is the result of the smoothing routine HSMOOF [52] on the histogram.

is the error returned from the fit when the number of input events equaled the means. The histogram of the values returned for Eq. 5.2 should be a Gaussian about 0 with mean near 1 if the fitting routine is functioning properly. The results from our pull, shown in Fig. 5.14, show that our fitter is reliable.

The numbers of events returned from the two dimensional fit to data for $\tilde{t}_1 \to b\tilde{\chi}_1^{\pm}$ (with $m_{\tilde{t}_1} = 115$ GeV/c^2) are plotted in Fig. 5.15. The number of events returned from the likelihood fit to data for $\tilde{t}_1 \to bl\tilde{\nu}$ (with $m_{\tilde{t}_1} = 100$ GeV/c^2) is plotted in Fig. 5.16.

The $\tilde{t}_1\bar{\tilde{t}}_1$ cross section is calculated by solving Eqs. 3.1 and 3.2 for $\sigma_{\tilde{t}_1\bar{\tilde{t}}_1}$:

$$\sigma_{\tilde{t}_1\bar{\tilde{t}}_1} = \frac{N_{\tilde{t}_1\bar{\tilde{t}}_1}}{\int \mathcal{L}dt \; \epsilon_{\text{selection cuts}}}, \tag{5.3}$$

where $N_{\tilde{t}_1\bar{\tilde{t}}_1}$ is the number of signal events returned from the fit and $\epsilon_{\text{selection cuts}}$ includes all selection requirement efficiencies, the geometrical acceptance, and any applicable branching ratios. The error on the cross section is determined by adding the errors on $N_{\tilde{t}_1\bar{\tilde{t}}_1}$ and the errors on $(\int \mathcal{L}dt \times \epsilon_{\text{selection cuts}})$ in quadrature. The errors on the number of events returned from the fit are typically quite large compared to the means, but we have determined that adding errors in quadrature is appropriate for Eq. 5.3. See Appendix B for a complete derivation of this result. To get the 95% C.L. limits on N_{obs} and $\sigma_{\tilde{t}_1\bar{\tilde{t}}_1}$, we use the Particle Data Group method to calculate the upper limit on a Gaussian distributed variable with mean near zero [54].

The 95% C.L. limits on $N_{\tilde{t}_1\bar{\tilde{t}}_1}$ and $\sigma_{\tilde{t}_1\bar{\tilde{t}}_1}$ from a fit of H_T and $\Delta\phi$(jet1,jet2) to data for $\tilde{t}_1 \to b\tilde{\chi}_1^{\pm}$ with $m_{\tilde{t}_1}$= 100, 110, 115, and 120 GeV/c^2 are listed in Table 5.5. The $\sigma_{\tilde{t}_1\bar{\tilde{t}}_1}$ limits are also plotted in Fig. 5.17. The NLO theoretical prediction for $\sigma_{\tilde{t}_1\bar{\tilde{t}}_1}$ is shown in Fig. 5.17 for comparison [7].

The 95% C.L. limits on $N_{\tilde{t}_1\bar{\tilde{t}}_1}$ and $\sigma_{\tilde{t}_1\bar{\tilde{t}}_1}$ from a fit of H_T to data for $\tilde{t}_1 \to bl\tilde{\nu}$ are listed in Table 5.6. The cross sections fall not only as a function of $m_{\tilde{t}_1}$ but also as a function of $m_{\tilde{\nu}}$ because selection efficiencies are proportional to $m_{\tilde{t}_1}$ and $m_{\tilde{\nu}}$. The limits on $\sigma_{\tilde{t}_1\bar{\tilde{t}}_1}$ are also plotted in Fig. 5.18 for $m_{\tilde{\nu}}$= 40 and 50 GeV/c^2. Fig. 5.19 shows the 95% C.L. limits on $\sigma_{\tilde{t}_1\bar{\tilde{t}}_1}$ for $m_{\tilde{\nu}}$= 45 GeV/c^2. Those combinations of $m_{\tilde{t}_1}$ and $m_{\tilde{\nu}}$ for which the 95% C.L. limit on $\sigma_{\tilde{t}_1\bar{\tilde{t}}_1}$ is less than the NLO theoretical prediction (for renormalization scale, μ, $= m_{\tilde{t}_1}$) are excluded. The resulting excluded region in the plane of $m_{\tilde{t}_1}, m_{\tilde{\nu}}$ is shown in Fig. 5.20.

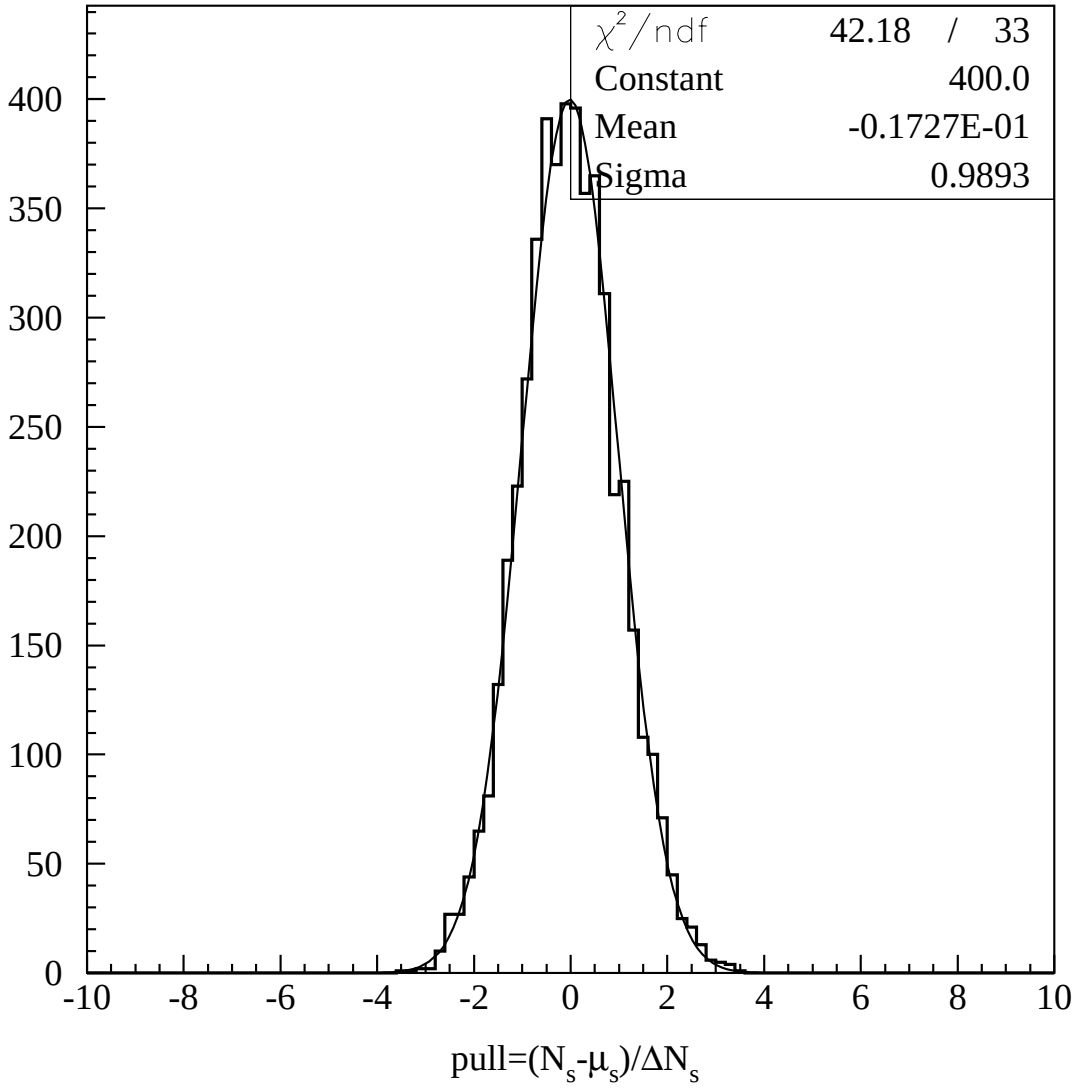

Figure 5.14: Test of reliability of likelihood fit routine. The test is described in the text. The value of $m_{\tilde{t}_1}$ used in the test was 120 GeV/c^2.

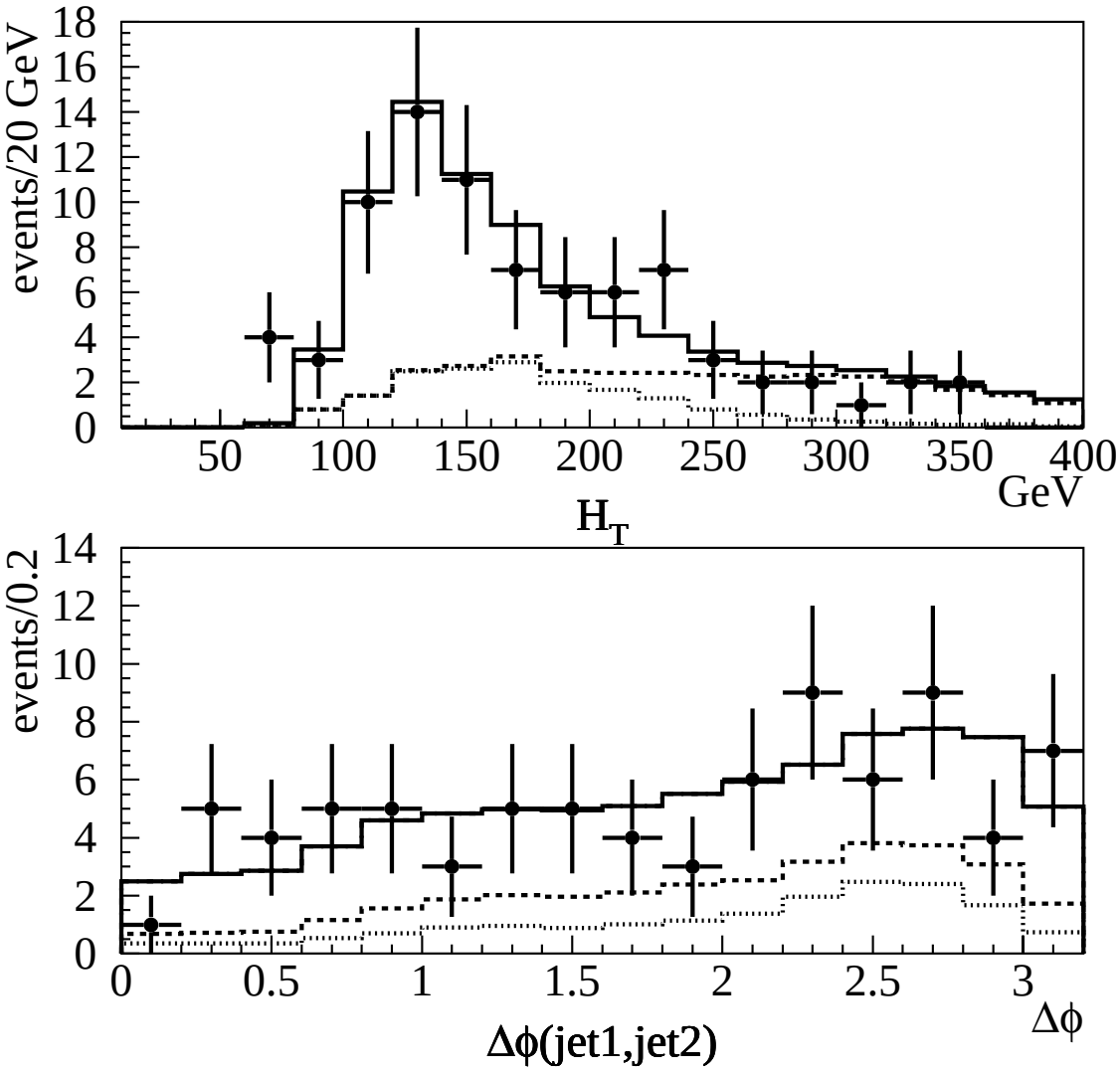

Figure 5.15: Unbinned likelihood fit results for the combination of H_T and $\Delta\phi$(jet1,jet2) for $\tilde{t}_1(115) \to b\tilde{\chi}_1^{\pm}$. The histograms reflect the number of each process returned from the fit. The contribution from $b\overline{b}$ is plotted with a dotted line. The contribution from $t\overline{t}$ is added to that from $b\overline{b}$ and plotted with a dashed line. The contribution from $W^{\pm}$ + jets is added to the dashed histogram and plotted with a solid line. There is no significant contribution from signal.

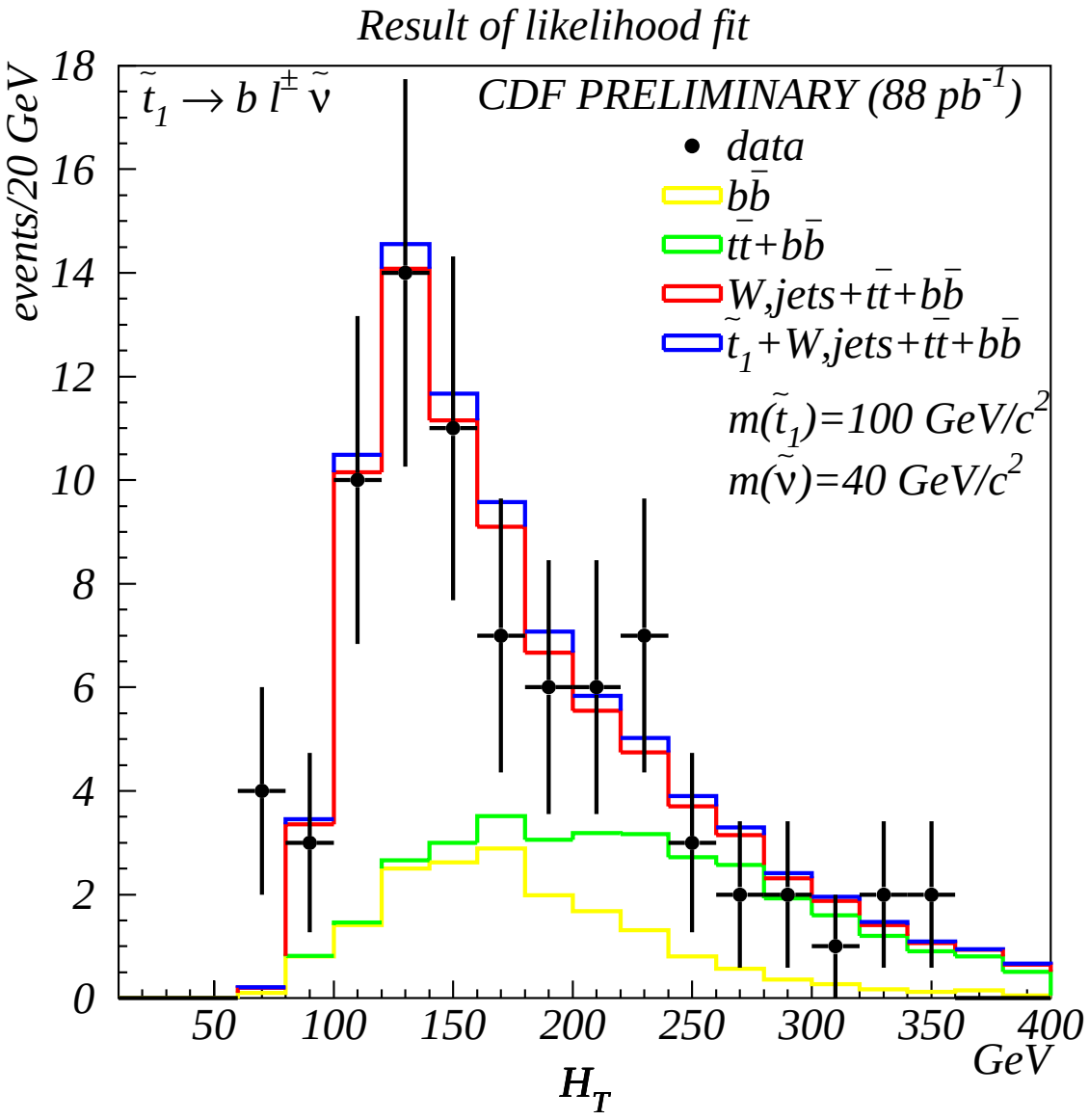

Figure 5.16: Result of unbinned likelihood fit to H_T for $\tilde{t}_1 \rightarrow bl\tilde{\nu}$ (with $m_{\tilde{t}_1} = 100$ GeV/c^2). The histograms reflect the number of each process returned from the fit. The contribution from $b\bar{b}$ is plotted in yellow. The contribution from $t\bar{t}$ is added to that from $b\bar{b}$ and plotted in green, and so on for each succeeding fitted process.

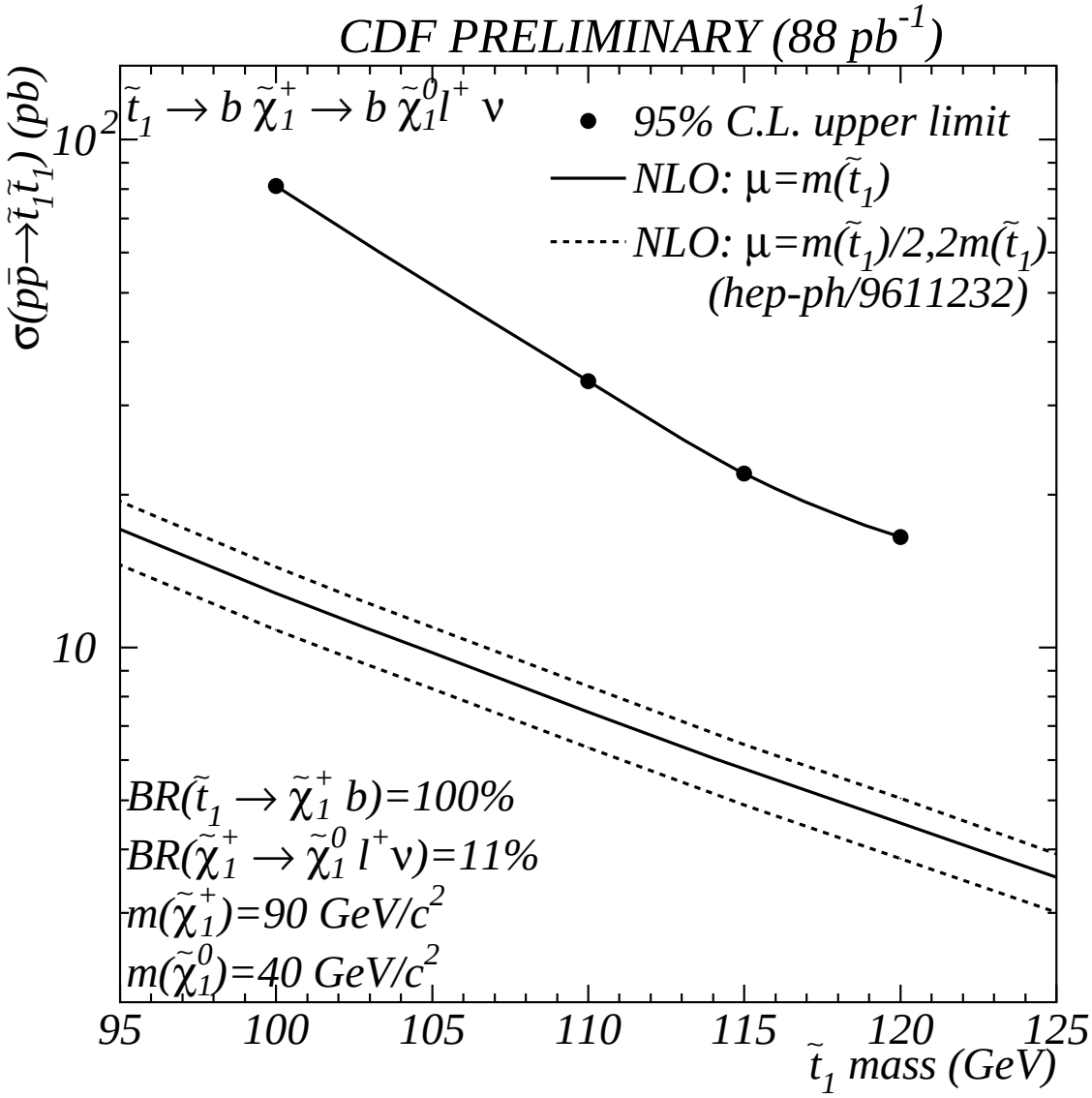

Figure 5.17: 95% C.L. cross section limit as a function of $\tilde{t}_1$ mass for the $\tilde{t}_1 \to b\tilde{\chi}_1^\pm$ decay scenario with $m_{\tilde{\chi}_1^\pm} = 90$ GeV/c^{2}and $m_{\tilde{\chi}_1^0} = 40$ GeV/c^2.

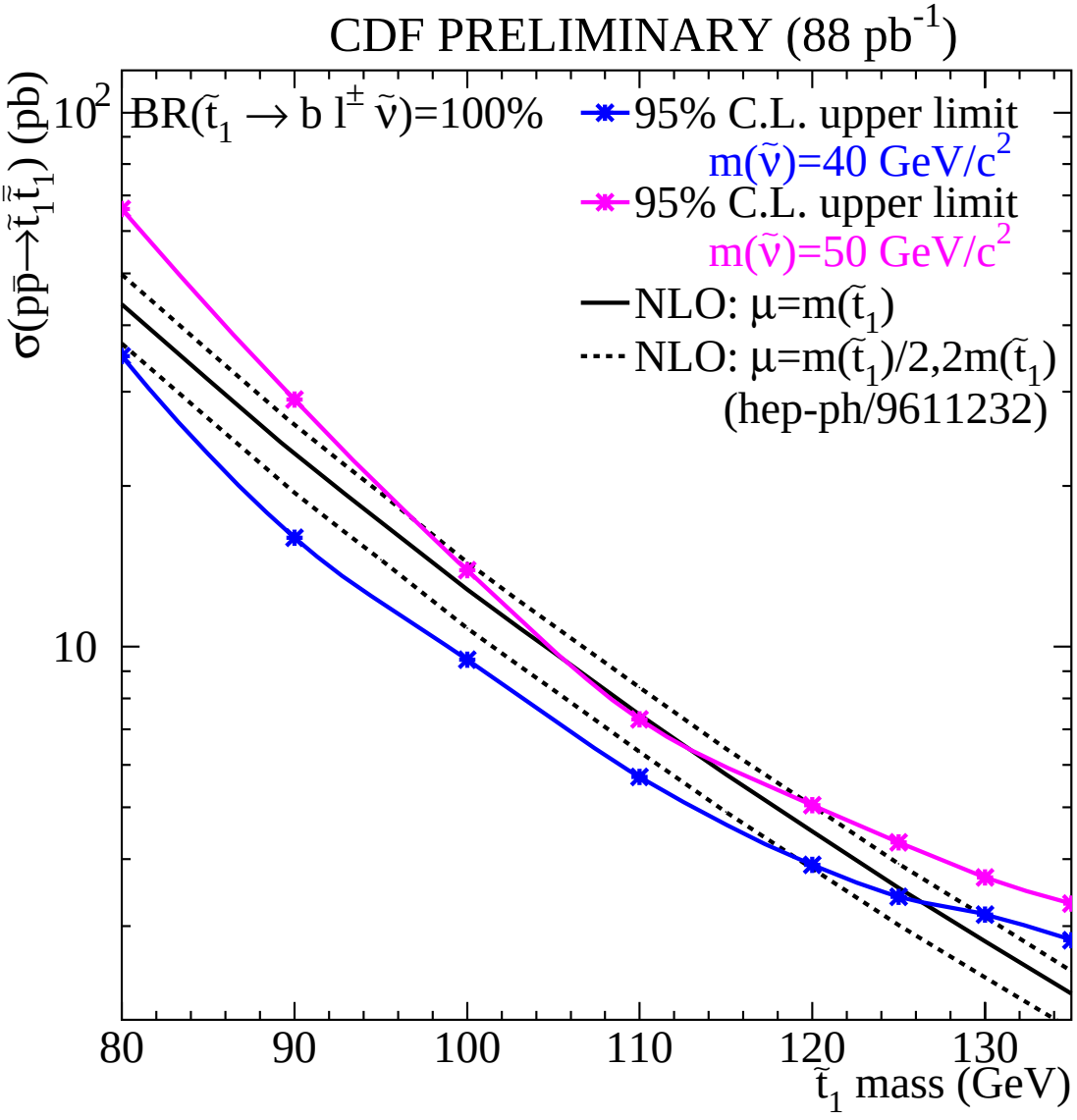

Figure 5.18: 95% C.L. cross section limit as a function of $\tilde{t}_1$ mass for the $\tilde{t}_1 \to bl\tilde{\nu}$ decay scenario with $m_{\tilde{\nu}} = 40$ and 50 GeV/c^2.

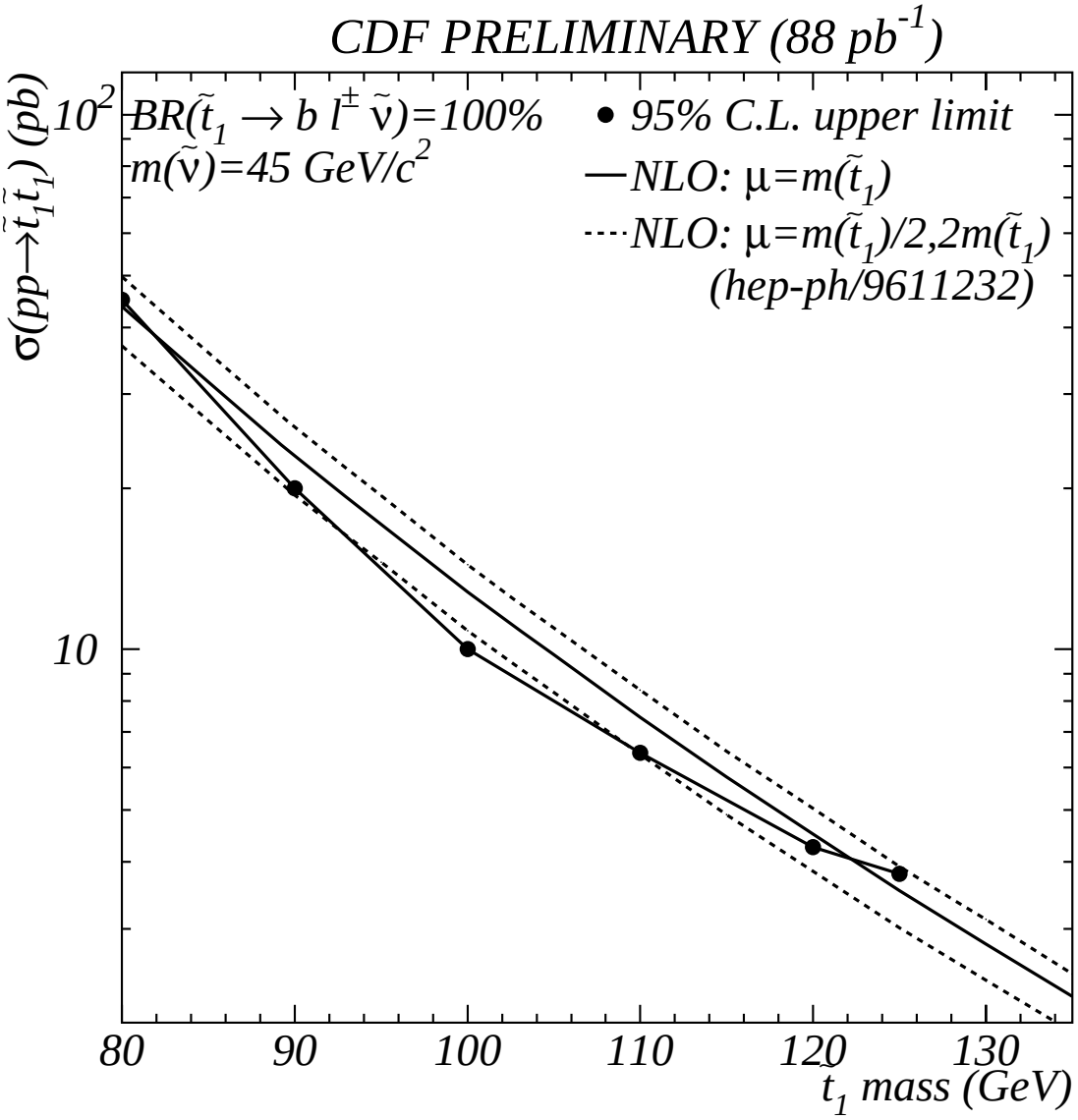

Figure 5.19: 95% C.L. cross section limit as a function of $\tilde{t}_1$ mass for the $\tilde{t}_1 \to bl\tilde{\nu}$ decay scenario with $m_{\tilde{\nu}} = 45$ GeV/c^2.

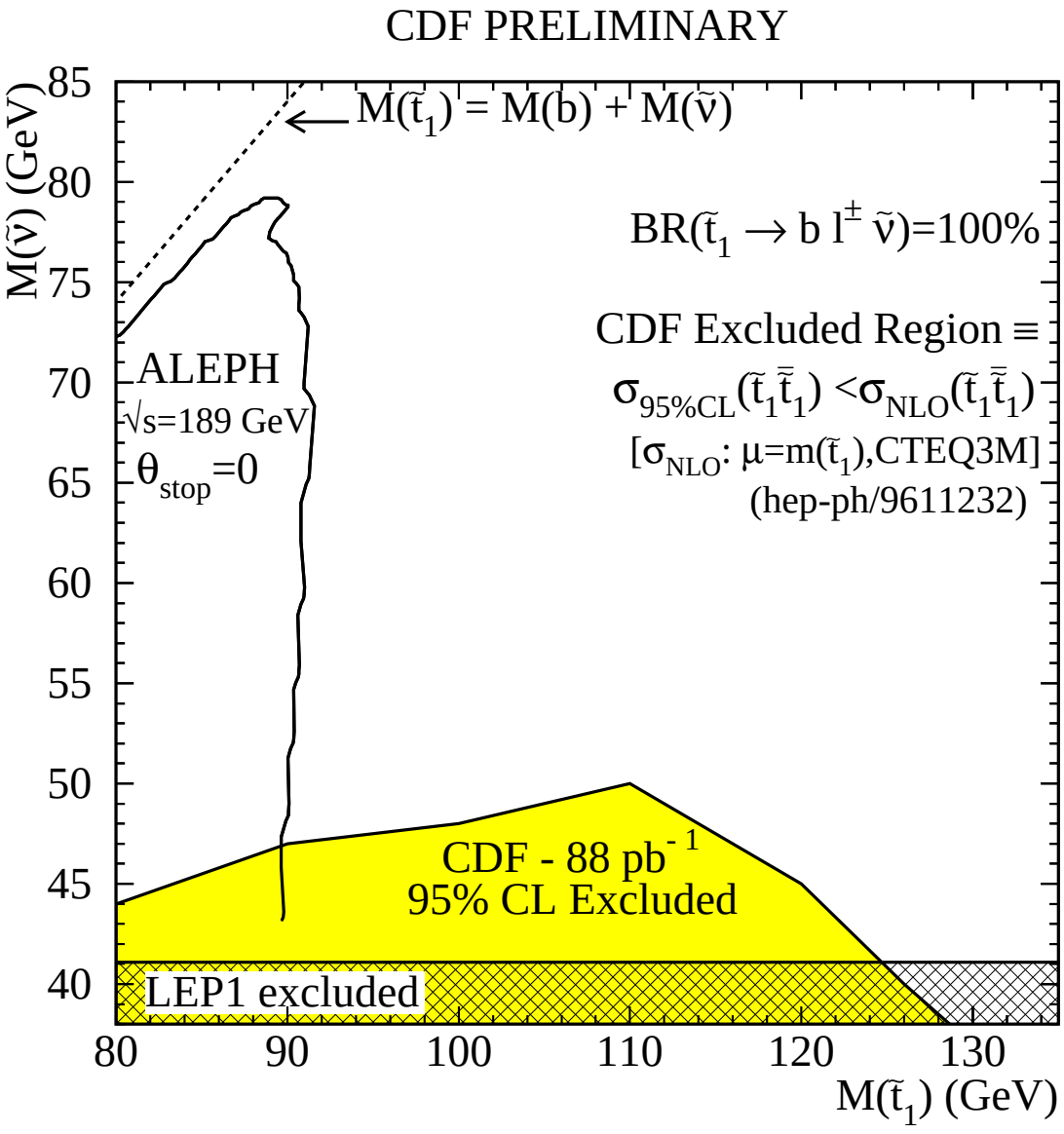

Figure 5.20: 95% C.L. excluded region in $m_{\tilde{t}_1}, m_{\tilde{\nu}}$.

Table 5.5: Cross section limits for $\tilde{t}_1\bar{\tilde{t}}_1$ in the $\tilde{t}_1 \to b\tilde{\chi}_1^{\pm}$ decay scenario at the 95% confidence level. The selection efficiencies listed are the cumulative efficiencies for all the selection cuts. The cross section limits are functions of the integrated luminosity (88 pb^{-1}). The differences in $N_{\tilde{t}_1\bar{\tilde{t}}_1}$ from the fit are a result of the changing H_T shape with $m_{\tilde{t}_1}$.

CDF PRELIMINARY (88 pb^{-1})

for $\mathcal{B}(\tilde{t}_1 \to b\tilde{\chi}_1^{\pm}) = 100\%$ and $\mathcal{B}(\tilde{\chi}_1^{+} \to l^{+}\nu\ \tilde{\chi}_1^{0}) = 11\%$

$m_{\tilde{t}_1}$ (GeV/c^2)	selection efficiency (%)	$N_{\tilde{t}_1\bar{\tilde{t}}_1}$ from fit	95% C.L. limit for $N_{\tilde{t}_1\bar{\tilde{t}}_1}$	95% C.L. limit for $\sigma_{\tilde{t}_1\bar{\tilde{t}}_1}$ (pb)	theoretical $\sigma_{\tilde{t}_1\bar{\tilde{t}}_1}$ (pb)
100	1.86±0.09±0.22	7.15±10.47	27.6	81.0	12.78
110	4.67±0.15±0.42	4.84±10.87	26.1	33.5	7.46
115	5.71±0.16±0.52	-0.28±11.72	23.0	22.0	5.76
120	6.69±0.18±0.63	-2.65±11.60	20.2	16.5	4.51

Table 5.6: Cross section limits for $\tilde{t}_1\bar{\tilde{t}}_1$ in the $\tilde{t}_1 \to bl\tilde{\nu}$ decay scenario at the 95% confidence level. Masses are in units of GeV/c^2. The selection efficiencies listed are the cumulative efficiencies for all the selection cuts. The cross section limits are functions of the integrated luminosity (88 pb^{-1}). The differences in $N_{\tilde{t}_1\bar{\tilde{t}}_1}$ from the fit are a result of the changing H_T shape with $m_{\tilde{t}_1}$.

for $\mathcal{B}(\tilde{t}_1 \to bl^{\pm}\tilde{\nu}) = 100\%$

$m_{\tilde{t}_1}$	$m_{\tilde{\nu}}$	selection efficiency (%)	$N_{\tilde{t}_1\bar{\tilde{t}}_1}$ from fit	95% C.L. limit for $N_{\tilde{t}_1\bar{\tilde{t}}_1}$	95% C.L. limit for $\sigma_{\tilde{t}_1\bar{\tilde{t}}_1}$ (pb)	theoretical $\sigma_{\tilde{t}_1\bar{\tilde{t}}_1}$ (pb)
80	40	1.17±0.05±0.13	15.1±9.76	34.2	35.0	43.74
90	40	2.04±0.06±0.21	7.10±11.2	29.0	16.3	22.97
100	40	3.08±0.08±0.26	3.54±11.2	25.5	9.46	12.78
110	40	3.81±0.09±0.32	-1.47±10.4	18.9	5.69	7.46
120	40	4.91±0.11±0.43	-1.94±9.59	17.0	3.94	4.51
125	40	5.20±0.11±0.47	-2.36±9.19	15.7	3.44	3.53
130	40	5.40±0.11±0.47	-2.92±9.02	14.9	3.15	2.81
135	40	5.67±0.11±0.50	-3.44±8.73	13.9	2.82	2.24
80	50	0.59±0.03±0.07	15.6±9.41	34.1	66.4	43.74
90	50	1.34±0.05±0.13	14.5±9.89	33.9	29.2	22.97
100	50	2.31±0.07±0.21	5.77±11.3	28.0	13.9	12.78
110	50	3.33±0.08±0.29	-0.97±10.9	21.4	7.33	7.46
120	50	4.17±0.10±0.36	-1.52±10.2	18.4	5.05	4.51
125	50	4.63±0.10±0.40	-1.72±9.73	17.4	4.28	3.53
130	50	5.00±0.11±0.44	-2.46±9.46	16.2	3.69	2.81
135	50	5.19±0.12±0.45	-2.97±9.11	14.9	3.28	2.24

Chapter 6

Conclusion

Using the Collider Detector at Fermilab, we have determined the upper limits on the $\tilde{t}_1\bar{\tilde{t}}_1$ cross section for the cases in which either $\mathcal{B}(\tilde{t}_1 \to b\tilde{\chi}_1^{\pm}) = 100\%$ or $\mathcal{B}(\tilde{t}_1 \to bl\tilde{\nu}) = 100\%$. We assumed that the lepton in $\tilde{t}_1 \to bl\tilde{\nu}$ could be an $e^{\pm}$, $\mu^{\pm}$, or $\tau^{\pm}$ with equal probability. Some of the cross section limits in the $\tilde{t}_1 \to bl\tilde{\nu}$ decay scenario for particular $m_{\tilde{t}_1}$ and $m_{\tilde{\nu}}$ are lower than the theoretical cross sections calculated in next-to-leading order. We considered these mass points excluded at the 95% confidence level and plotted this excluded region in the plane of $m_{\tilde{t}_1}, m_{\tilde{\nu}}$.

The Collider Detector at Fermilab is currently being upgraded, and there are run improvements planned for the Tevatron as well. Some of the improvements planned for the Tevatron include increasing the luminosity by a factor of 20 to at least 2 fb^{-1} and increasing in the collision energy from $\sqrt{s}$=1.8 to 2.0 TeV [55]. The increase in $\sqrt{s}$ translates into an increase in the $\tilde{t}_1\bar{\tilde{t}}_1$ production cross section of roughly 40%. The CDF detector upgrades include expanded SVX coverage to $|\eta| \leq 2$ with an extra layer of silicon and double sided readout to provide measurement in $r-z$, with improved resolution in $r-\phi$. These improvements and the addition of an intermediate layer of silicon (ISL) will increase the b jet tagging efficiency from the former $\sim$40% to $\sim$65%. The CDF triggering will include a b-jet tag trigger which will add sensitivity to $\tilde{t}_1$ in non-leptonic decay modes. These combined improvements will increase our chances for observing $\tilde{t}_1$ in Run II.

Appendices

Appendix A

Level 3 Trigger Efficiency Measurements

The Level 3 trigger is a software filter that analyzes reconstructed physics objects, such as electrons, muons, and jets. Similar code is used for offline filtering on these same objects. The Level 3 trigger efficiencies are measurements of the efficiencies for the Level 3 code to identify physics objects with respect to the offline code. The differences can be due to improvements in the CDF offline code made after the Run 1B data taking period.

We measured the Level 3 trigger efficiencies for the dominant triggers found in the data sets MULB and ECLB from Run 1B. The dominant triggers were determined from a subsample of the data that was stripped for this $\tilde{t}_1$ search but should be representative of the whole with respect to trigger paths. Trigger efficiencies are determined as a function of p_T for use in the trigger simulation described in Section 4.2.

The dominant Level 3 trigger in the ECLB stripped data is ELEB_CEM_8_6, which passes 99.03% of the events. This trigger accepts events with an electron with CEM energy greater than 7.5 GeV and CTC $p_T \geq 6.0$ GeV/c. The trigger ELEB_CEM_8 passes 92.53% of the remaining events. This trigger accepts events with an electron with CEM energy greater than 7.5 GeV. The two triggers combined pass 99.93% of the events, so the electron trigger study was limited to this combination.

The dominant Level 3 trigger in the MULB stripped data is MUOB_CMU_CMP_8, which passes 93.44% of the events. This trigger accepts events in which a CMU muon with CMP confirmation has $p_T \geq 8$ GeV, The trigger MUOB_CMX_8 passes 98.61% of the events not passed by MUOB_CMU_CMP_8, and MUOB_CMX_15 passes 50% of the remaining events. The MUOB_CMX_8 and MUOB_CMX_15 triggers accept

events in which a CMX muon has $p_T \geq 8$ GeV or 15 GeV/c, respectively. The efficiencies for these three triggers are determined separately.

A.1 Method for Determining Trigger Efficiencies

The efficiencies of the Level 3 electron (muon) triggers are determined using the well known procedure of looking for events with good electrons (muons) in an uncorrelated Level 3 trigger stream then counting the number of these that pass the electron (muon) trigger under study [56]. The ECLB stream is used to study MUOB_CMU_CMP_8, MUOB_CMX_8 and MUOB_CMX_15. The MULB stream is used to study ELEB_CEM_8 and ELEB_CEM_8_6.

The following criteria define a good electron:

- central (deposits its energy in the CEM)
- Hadron/EM calorimeter energy ≤ 0.05
- $|\Delta x| \leq 3.0$ cm
- $|\Delta z| \leq 5.0$ cm
- $\chi^2_{strip} \leq 10.0$
- $\chi^2_{wire} \leq 10.0$
- $L_{shr} \leq 0.2$
- lies in the fiducial region
- γ conversions removed
- passes the Level 1 trigger L1_CALORIMETER (This trigger has a CEM tower threshold of 8.0 GeV.)
- passes one of these Level 2 triggers:
  - CEM_8_CFT_7_5_XCES (electron $E_T \geq 8.0$ GeV, $p_T \geq 7.5$ GeV/c)
  - CEM_8_CFT_7_5 (electron $E_T \geq 8.0$ GeV, $p_T \geq 7.5$ GeV/c)
  - CEM_12_CFT_12_XCES (electron $E_T \geq 12.0$ GeV, $p_T \geq 12.0$ GeV/c)
  - CEM_16_CFT_12 (electron $E_T \geq 16.0$ GeV, $p_T \geq 12.0$ GeV/c)

All Level 3 trigger cuts are included in this list.

The following criteria define a good muon:

- a CMU muon with CMP confirmation or a CMX muon
- EM calorimeter energy ≤ 2.0 GeV
- Hadron calorimeter energy ≤ 6.0 GeV
- $|\Delta x|$ (CMU) $\leq$ 2cm
- $|\Delta x|$ (CMP) $\leq$ 5cm
- $|\Delta x|$ (CMX) $\leq$ 5cm
- lies in the fiducial region
- cosmic rays removed
- χ^2_x (CMU) ≤ 11.0
- χ^2_z (CMU) ≤ 14.0
- χ^2_x (CMP) ≤ 11.0
- χ^2_x (CMX) ≤ 16.0

The last four items are required by MUOB_CMU_CMP_8 or MUOB_CMX_8. If the muon hits both the CMU and CMP, it must pass CMU_CMP_6PT0_HTDC (muon $p_T \geq 6.0$ GeV/c) at Level 1 and CMUP_CFT_7_5_5DEG (muon $p_T \geq 7.5$ GeV/c) or CMUP_CFT_12_5DEG (muon $p_T \geq 12.0$ GeV/c) at Level 2. CMX muons must pass CMX_10PT0_HTDC (muon $p_T \geq 10.0$ GeV/c) at Level 1 and CMX_CFT_12_5DEG(muon $p_T \geq 12.0$ GeV/c) at Level 2.

The Level 1 and 2 triggers prerequisites decouples their efficiencies from the Level 3 efficiency calculation. The resulting Level 3 efficiency can be multiplied by those of Level 1 and 2 to give an overall trigger efficiency.

Events used in the electron trigger study are required to have only one electron that could pass the ELEB_CEM_8 or ELEB_CEM_8_6 trigger requirements ignoring the E_T cut. Muon candidate events can have only one type 3 or 4 muon. This simplifies the efficiency calculation.

A.2 Results

The ELEB_CEM_8 and ELEB_CEM_8_6 combined trigger efficiencies are plotted in Fig. A.1 as a function of E_T. The MUOB_CMU_CMP_8, MUOB_CMX_8, and MUOB_CMX_15 trigger efficiencies are shown in Figs. A.2, A.3, and A.4 as a function of p_T. Since MUOB_CMX_8 was on for only a portion of Run 1B, many good CMX muons found in the ECLB stream did not have the opportunity to pass this trigger. The reported MUOB_CMX_8 efficiency is the product of the true trigger efficiency and the fraction of the time the trigger was running during Run 1B.

If the trigger efficiency in a given p_T bin was estimated to be 100% (0%), the plotted error is the 95% C.L. lower (upper) limit for binomial statistics from reference [57].

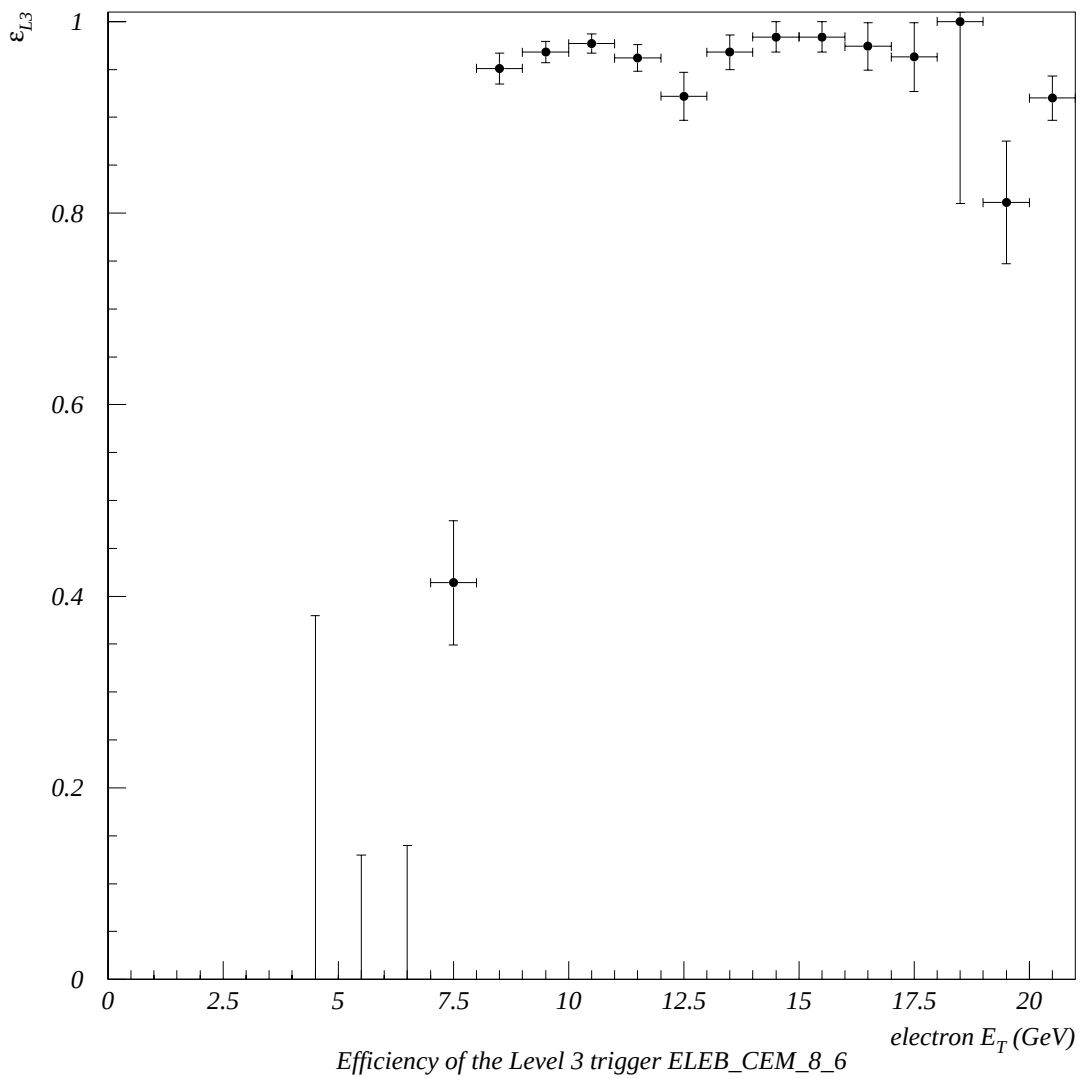

Figure A.1: Combined trigger efficiencies for the Level 3 triggers ELEB_CEM_8 and ELEB_CEM_8_6 as a function of electron E_T. Efficiencies were calculated for 1 GeV bins. The last bin contains events with $E_T \geq 20$ GeV. For bins in which the estimated efficiency is equal to 100% (0%), the plotted error is the 95% C.L. lower (upper) limit from reference [57].

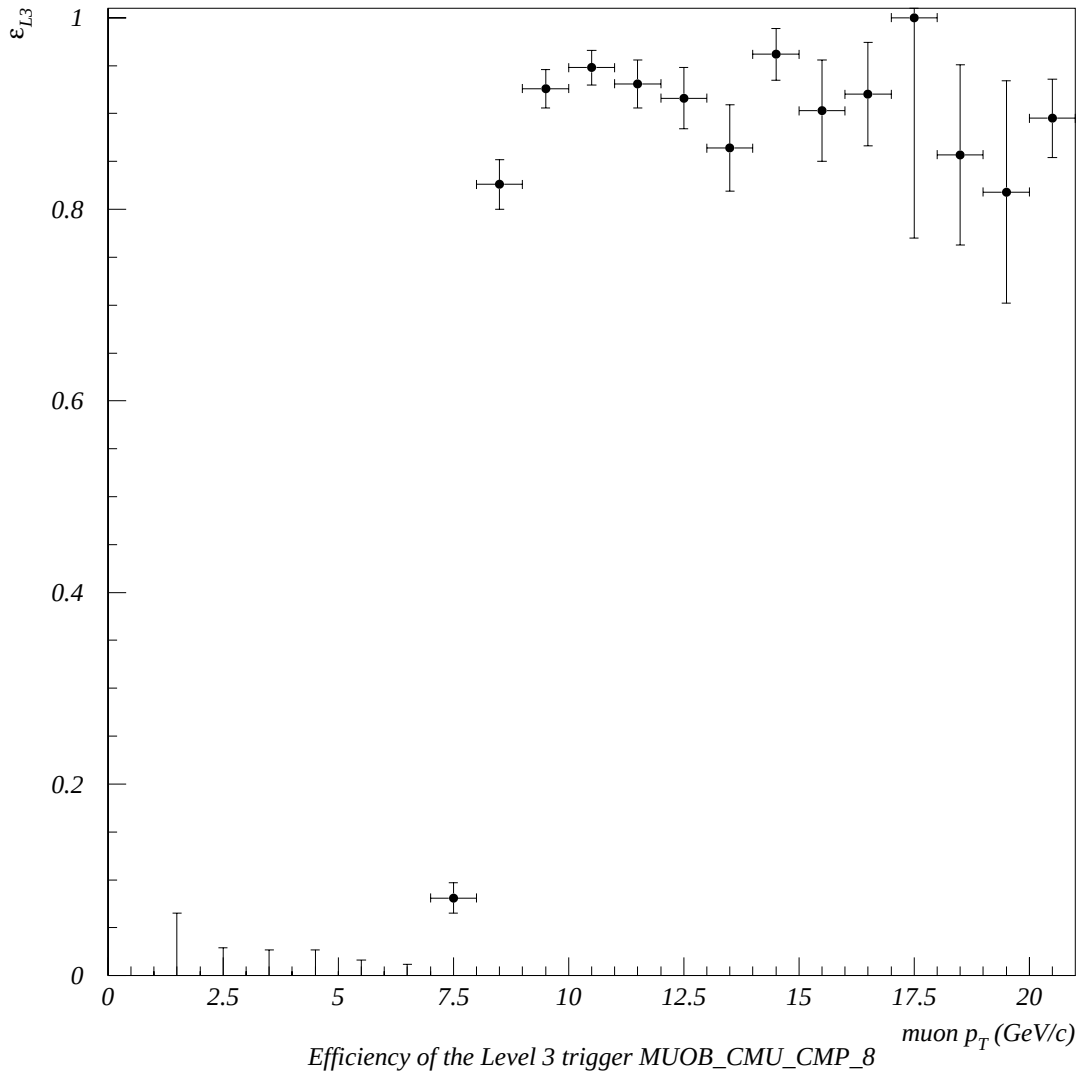

Figure A.2: Trigger efficiency for the Level 3 trigger MUOB_CMU_CMP_8 as a function of muon p_T. Efficiencies were calculated for 1 GeV/c bins. The last bin contains events with $p_T \geq 20$ GeV/c. For bins in which the estimated efficiency is equal to 100% (0%), the plotted error is the 95% C.L. lower (upper) limit from reference [57].

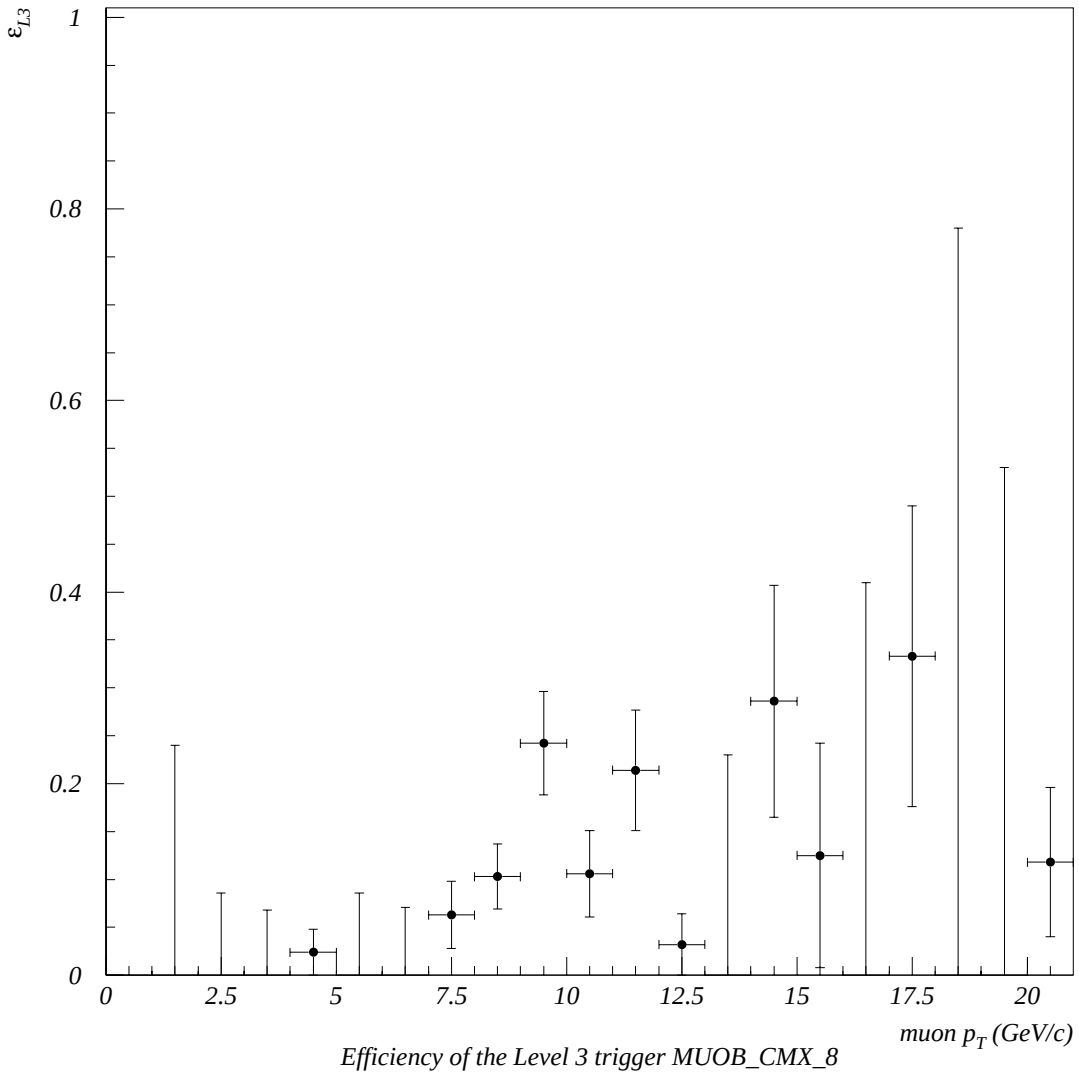

Figure A.3: Trigger efficiency for the Level 3 trigger MUOB_CMX_8 as a function of muon p_T. Since MUOB_CMX_8 was on for only a portion of Run 1B, this efficiency is the product of the true trigger efficiency and the trigger run time. Efficiencies were calculated for 1 GeV/c bins. The last bin contains events with $p_T \geq 20$ GeV/c. For bins in which the estimated efficiency is equal to 0%, the plotted error is the 95% C.L. upper limit from reference [57].

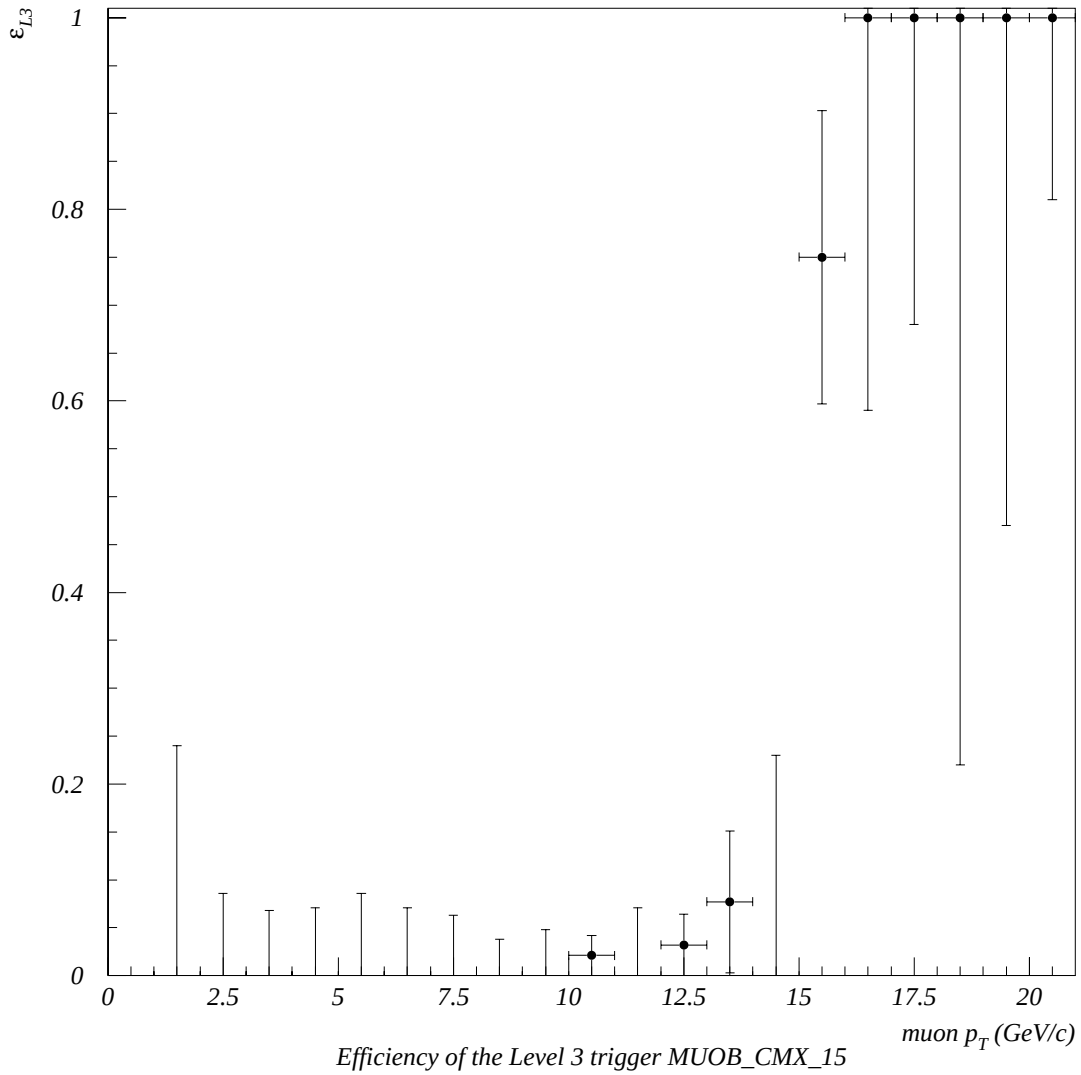

Figure A.4: Trigger efficiency for the Level 3 trigger MUOB_CMX_15 as a function of muon p_T. Efficiencies were calculated for 1 GeV/c bins. The last bin contains events with $p_T \geq 20$ GeV/c. For bins in which the estimated efficiency is equal to 100% (0%), the plotted error is the 95% C.L. lower (upper) limit from reference [57].

Appendix B

Error Propagation for Large Errors

The standard error propagation equation for a function of an arbitrary number of variables, $f(\mathbf{x})$, is derived from a Taylor series expansion about the means[1], $\bar{\mathbf{x}}$:

$$f(\mathbf{x}) \cong f(\bar{\mathbf{x}}) + \sum_{i=1}^{n} (x_i - \bar{x}_i) \left. \frac{\partial f(\mathbf{x})}{\partial x_i} \right|_{\mathbf{x}=\bar{\mathbf{x}}} \tag{B.1}$$

To justify truncating this series, $x_i - \bar{x}_i$ must be small. The variance of $f(\mathbf{x})$ is

$$\begin{aligned} \sigma_f^2 &= E[(f(\mathbf{x}) - E[f(\mathbf{x})])^2] \\ &\simeq E[(f(\mathbf{x}) - f(\bar{\mathbf{x}}))^2], \end{aligned} \tag{B.2}$$

where $E[x]$ is the expectation value of x, $E[(x)^n]$ is the nth moment, and $E[(x-\bar{x})^n]$ is the nth moment about the mean of x. Substituting Eq. B.1 into Eq. B.2 gives

$$\sigma_f^2 \simeq \sum_{i=1}^{n} \sum_{j=1}^{n} \left. \frac{\partial f(\mathbf{x})}{\partial x_i} \right|_{\mathbf{x}=\bar{\mathbf{x}}} \left. \frac{\partial f(\mathbf{x})}{\partial x_j} \right|_{\mathbf{x}=\bar{\mathbf{x}}} E[(x_i - \bar{x}_i)(x_j - \bar{x}_j)]. \tag{B.3}$$

where we have pulled the partial derivative terms outside of the expectation value since they are constants. Recognizing that, for any probability distribution $w(\mathbf{x})$,

$$\begin{aligned} E[(x_i - \bar{x}_i)(x_j - \bar{x}_j)] &= \int_{-\infty}^{+\infty} \cdots \int_{-\infty}^{+\infty} (x_i - \bar{x}_i)(x_j - \bar{x}_j) w(\mathbf{x}) \prod_{i=1}^{n} dx_i \\ &= \sigma_{ij} \end{aligned}$$

and that $\sigma_{ij} = \delta_{ij}\sigma_i^2$ for independent variables x_i, Eq. B.3 becomes the standard error propagation equation:

$$\sigma_f^2 \simeq \sum_{i=1}^{n} \left(\left. \frac{\partial f(\mathbf{x})}{\partial x_i} \right|_{\mathbf{x}=\bar{\mathbf{x}}} \sigma_i \right)^2. \tag{B.4}$$

[1] This treatment is found in almost any book on error analysis. I am following B. R. Martin [58].

If $x_i - \bar{x}_i$ is not necessarily small, we should carry the Taylor series expansion out to more terms.[2] Eq. B.1 becomes

$$\begin{aligned} f(\mathbf{x}) &= f(\bar{\mathbf{x}}) + \sum_{i=1}^{n} (x_i - \bar{x}_i) \left.\frac{\partial f(\mathbf{x})}{\partial x_i}\right|_{\mathbf{x}=\bar{\mathbf{x}}} + \frac{(x_i - \bar{x}_i)^2}{2!} \left.\frac{\partial^2 f(\mathbf{x})}{\partial x_i^2}\right|_{\mathbf{x}=\bar{\mathbf{x}}} \\ &\quad + \frac{(x_i - \bar{x}_i)^3}{3!} \left.\frac{\partial^3 f(\mathbf{x})}{\partial x_i^3}\right|_{\mathbf{x}=\bar{\mathbf{x}}} + \ldots \end{aligned}$$

And Eq. B.3 becomes

$$\begin{aligned} \sigma_f^2 &\simeq E\left[\sum_{i=1}^{n}\sum_{j=1}^{n} \left((x_i - \bar{x}_i) \left.\frac{\partial f(\mathbf{x})}{\partial x_i}\right|_{\mathbf{x}=\bar{\mathbf{x}}} + \frac{(x_i - \bar{x}_i)^2}{2!} \left.\frac{\partial^2 f(\mathbf{x})}{\partial x_i^2}\right|_{\mathbf{x}=\bar{\mathbf{x}}} + \frac{(x_i - \bar{x}_i)^3}{3!} \left.\frac{\partial^3 f(\mathbf{x})}{\partial x_i^3}\right|_{\mathbf{x}=\bar{\mathbf{x}}} \right) \right. \\ &\quad \left. \times \left((x_j - \bar{x}_j) \left.\frac{\partial f(\mathbf{x})}{\partial x_j}\right|_{\mathbf{x}=\bar{\mathbf{x}}} + \frac{(x_j - \bar{x}_j)^2}{2!} \left.\frac{\partial^2 f(\mathbf{x})}{\partial x_j^2}\right|_{\mathbf{x}=\bar{\mathbf{x}}} + \frac{(x_j - \bar{x}_j)^3}{3!} \left.\frac{\partial^3 f(\mathbf{x})}{\partial x_j^3}\right|_{\mathbf{x}=\bar{\mathbf{x}}} \right) \right] \quad \text{(B.5)} \end{aligned}$$

Since $\sigma_{ij} = \delta_{ij}\sigma_i^2$, we can omit terms quadratic in $x_i x_j$ where $i \neq j$. We are also only interested in x_i which have a Gaussian probability distribution. The general solutions for $E[(x_i - \bar{x}_i)^n]$ for a Gaussian distribution are [58]:

$$E[(x_i - \bar{x}_i)^n] = \begin{cases} \frac{n!}{(n/2)!\ 2^{n/2}}\ \sigma^n & \text{for even } n \\ 0 & \text{for odd } n \geq 3 \end{cases}$$

Using these results, Eq. B.5 becomes

$$\begin{aligned} \sigma_f^2 &\simeq E\left[\sum_{i=1}^{n}\sum_{j=1}^{n} \left((x_i - \bar{x}_i) \left.\frac{\partial f(\mathbf{x})}{\partial x_i}\right|_{\mathbf{x}=\bar{\mathbf{x}}} + \frac{(x_i - \bar{x}_i)^2}{2!} \left.\frac{\partial^2 f(\mathbf{x})}{\partial x_i^2}\right|_{\mathbf{x}=\bar{\mathbf{x}}} \right) \right. \\ &\quad \times \left((x_j - \bar{x}_j) \left.\frac{\partial f(\mathbf{x})}{\partial x_j}\right|_{\mathbf{x}=\bar{\mathbf{x}}} + \frac{(x_j - \bar{x}_j)^2}{2!} \left.\frac{\partial^2 f(\mathbf{x})}{\partial x_j^2}\right|_{\mathbf{x}=\bar{\mathbf{x}}} \right) \\ &\quad \left. + \sum_{i=1}^{n} \left(\frac{(x_i - \bar{x}_i)^3}{3!} \left.\frac{\partial^3 f(\mathbf{x})}{\partial x_i^3}\right|_{\mathbf{x}=\bar{\mathbf{x}}} \right)^2 \right] \\ &\simeq \sum_{i=1}^{n}\sum_{j=1}^{n} E\left[(x_i - \bar{x}_i)(x_j - \bar{x}_j) \left.\frac{\partial f(\mathbf{x})}{\partial x_i}\right|_{\mathbf{x}=\bar{\mathbf{x}}} \left.\frac{\partial f(\mathbf{x})}{\partial x_j}\right|_{\mathbf{x}=\bar{\mathbf{x}}} \right. \\ &\qquad \left. + \frac{(x_i - \bar{x}_i)^2 (x_j - \bar{x}_j)^2}{4} \left.\frac{\partial^2 f(\mathbf{x})}{\partial x_i^2}\right|_{\mathbf{x}=\bar{\mathbf{x}}} \left.\frac{\partial^2 f(\mathbf{x})}{\partial x_j^2}\right|_{\mathbf{x}=\bar{\mathbf{x}}} \right] \\ &\quad + \sum_{i=1}^{n} E\left[\left(\frac{(x_i - \bar{x}_i)^3}{3!} \left.\frac{\partial^3 f(\mathbf{x})}{\partial x_i^3}\right|_{\mathbf{x}=\bar{\mathbf{x}}} \right)^2 \right] \end{aligned}$$

[2] This is recommended by the Particle Data Group.

$$\simeq \sum_{i=1}^{n}\left(\left.\frac{\partial f(\mathbf{x})}{\partial x_i}\right|_{\mathbf{x}=\bar{\mathbf{x}}}\sigma_i\right)^2+\sum_{i=1}^{n}\sum_{j=1}^{n}\left.\frac{\partial^2 f(\mathbf{x})}{\partial x_i^2}\right|_{\mathbf{x}=\bar{\mathbf{x}}}\left.\frac{\partial^2 f(\mathbf{x})}{\partial x_j^2}\right|_{\mathbf{x}=\bar{\mathbf{x}}}\frac{\sigma_i^2\sigma_j^2}{4}$$
$$+\frac{15}{36}\sum_{i=1}^{n}\left(\left.\frac{\partial^3 f(\mathbf{x})}{\partial x_i^3}\right|_{\mathbf{x}=\bar{\mathbf{x}}}\right)^2\sigma_i^6. \tag{B.6}$$

The second and third terms are the correction to the standard error propagation equation when we carry the Taylor expansion out to third order in x_i for Gaussian distributions.

Our function of interest is f(x,y)=x/y, where σ_x is large but σ_y/y is typically less than 10%. The partial derivatives are

$$\frac{\partial f(x,y)}{\partial x}=\frac{1}{y} \quad , \quad \frac{\partial f(x,y)}{\partial y}=\frac{-x}{y^2}$$
$$\frac{\partial^2 f(x,y)}{\partial x^2}=0 \quad , \quad \frac{\partial^2 f(x,y)}{\partial y^2}=\frac{2x}{y^3}.$$
$$\frac{\partial^3 f(x,y)}{\partial x^3}=0 \quad , \quad \frac{\partial^3 f(x,y)}{\partial y^3}=\frac{-6x}{y^4}.$$

We see that for our special case, even if the odd moments had not vanished we would still not have terms higher than the first derivative with respect to x. Eq. B.6 becomes

$$\begin{aligned}\sigma_f^2 &\simeq \left(\frac{\partial f(x,y)}{\partial x}\sigma_x\right)^2+\left(\frac{\partial f(x,y)}{\partial y}\sigma_y\right)^2+\left(\frac{\partial^2 f(x,y)}{\partial y^2}\sigma_y^2\right)^2+\frac{15}{36}\left(\frac{\partial^3 f(x,y)}{\partial y^3}\sigma_y^3\right)^2\\ &\simeq \left(\frac{\sigma_x}{y}\right)^2+\left(\frac{-x}{y^2}\sigma_y\right)^2+\left(\frac{2x}{y^3}\frac{\sigma_y^2}{4}\right)^2+\frac{15}{36}\left(\frac{-6x}{y^4}\sigma_y^3\right)^2\\ &\simeq \left(\frac{\sigma_x}{y}\right)^2+\left(\frac{-x}{y}\frac{\sigma_y}{y}\right)^2+\left(\frac{x}{2y}\frac{\sigma_y^2}{y^2}\right)^2+15\left(\frac{x}{y}\frac{\sigma_y^3}{y^3}\right)^2\end{aligned} \tag{B.7}$$

We can conclude that the last two terms in Eq. B.7 are small since they are proportional to $(\sigma_y/y)^4$ and $(\sigma_y/y)^6$.

References

[1] S. Martin, *A Supersymmetry Primer*, hep-ph/9709556 (1997).

[2] M. Drees, *An Introduction to Supersymmetry*, KEK-TH-501, (1996).

[3] P. West, *Introduction to Supersymmetry and Supergravity*, 2d Ed. World Scientific (1990).

[4] K. Cahill, *Elements of Supersymmetry*, hep-ph/9907295, (1999).

[5] Quantum field theory and the Standard Model are described in detail in S. Weinberg, *The Quantum Theory of Fields, Vol. II*, Cambridge (1995). Additional material relating to the Standard Model can be found in C. Quigg, *Gauge Theories of the Strong, Weak, and Electromagnetic Interactions*, The Benjamin-Cummings Publishing Co., Inc., Canada (1983).

[6] B. Tannenbaum, *A Search for Chargino-Neutralino Production at the Fermilab Tevatron Collider*, NMCPP 97/12 (1997).

[7] W. Beenakker *et al.*, *SUSY Particle Production at the Tevatron*, CERN-TH/98-368, (1998). The authors created the computer code PROSPINO to calculate NLO cross sections (see hep-ph/99611232). Chris Holck generated the cross sections we display in this document.

[8] W. Porod, *More on Light Decays of the Lighter Top Squark*, hep-ph/9812230 (1998).

[9] The fermilab web page has a very nice photo tour of the accelerator complex at *http://www.fnal.gov/pub/accel_tour.html*.

[10] D. Patterson, *FNAL Linac*, Fermilab internal note (1986).

[11] For a description of the original CDF detector see F. Abe *et al.*, (The CDF Collaboration), Nucl. Instr. and Meth. **A**350, 74 (1994).

[12] For a description of the CDF detector upgrades see F. Abe *et al.*, (The CDF Collaboration), Phys. Rev. **D50**, 2966 (1994); D. Amidei *et al.*, Nucl. Instr. and Meth. **A**71 (1988).

[13] A slightly more detailed treatment is given in The European Physics Journal **C**, 188 (1998). This is also referred to as the Particle Data Book.

[14] T. Westhusing and T. Liss, *Making a CMUO bank*, CDF internal note 1836 (1992).

[15] E. Guillian, *Top Quark Decay Kinematics in Fully Reconstructed $t\bar{t}$ Events in the e or μ + $\not\!\!E_T$ + $\geq$ 4 Jet Decay Channel*, Ph.D. Thesis. The University of Michigan (1999).

[16] F. Abe *et al.*, (The CDF Collaboration), Phys. Rev. **D45**, 1448 (1992).

[17] The Monte Carlo data sets generated by Stephan Lammel for exotics searches are described on this web page: *http://www-cdf.fnal.gov/internal/physics/exotic/susy/info/mc_run_1b.html.*

[18] F. Abe *et al.*, (The CDF Collaboration), Phys. Rev. Lett. **80**, 5275 (1998).

[19] K. Ackerstaff, *et al.*, (OPAL Collaboration), Eur. Phys. J. C 2, 213 (1998).

[20] ALEPH Collaboration, *Search for Charginos and Neutralinos at 183 GeV for Large Slepton Masses*, ALEPH 98-016 (1998).

[21] L3 Collaboration, *Search for Scalar Leptons, Charginos and Neutralinos in e^+e^- Collisions at $\sqrt{s}$ = 183 GeV*, L3 Note 2231 (1998).

[22] The LEP1 lower limit on $m_{\tilde{\nu}}$ is 41.1 GeV/c^{2}from D. Decamp *et al.*, The ALEPH Collaboration, Phys. Rep. **216**, 253 (1992).

[23] ALEPH Collaboration, *Scalar Quark Searches in e^+e^- Collisions at $\sqrt{s}$ = 181-184 GeV*, CERN-EP/98-076 (1998), submitted to Phys. Lett. B. The OPAL Collaboration, *Search for Scalar Top and Scalar Bottom Quarks at $\sqrt{s}$ = 183 GeV at LEP*, CERN-EP/98-107 (1998) and Eur. Phys. J. C 6, 225-238 (1998). LEP2 results for $m_{\tilde{t}_1}$ are found in the following: R.Barate et al. for the ALEPH collaboration, *Searches for sleptons and squarks in e+e- collisions at $\sqrt{s}$=188.6 GeV*, to be submitted to Phys. Lett. **B**.

[24] H. Baer, F.E. Paige, S.D. Protopopescu, and X. Tata, in *Simulating Supersymmetry with ISAJET 7.0/ISASUSY 1.0*, Proceedings of Workshop on Physics at Current Accelerators and the Supercollider, Eds. J. Hewett, A. White, and D. Zeppenfield (Argonne National Laboratory, 1993).

[25] G. Marchesini *et al.*, Comput. Phys. Commun. **67**, 465 (1992).

[26] Apollinari *et al.*, *Measurement of the data to simulation scale factor for the tagging efficiency of SECVTX and JPB*, CDF internal note 4257 (1997). This reference is recommended by the top group conveners in *Godparents Report on the new $t\bar{t}$ Cross Section Measurement in the lepton + jets channel using SECVTX tags*, CDF internal note 4939 (1999).

[27] T. Stelzer, Z. Sullivan, and S. Willenbrock, Phys. Rev. **D56**, 5619 (1998).

[28] J.P. Done, M. Chertok, and T. Kamon, *ISAJET Monte Carlo Validation*, CDF internal note 4903 (1998).

[29] F. A. Berends *et al.*, Nucl. Phys. **B357**, 32 (1991).

[30] D. Cronin-Hennessy *et al.*, *Measurement of the $W^{\pm} \to e^{\pm}\nu$ + n Jet Cross Section in 1.8 TeV $p\overline{p}$ Collisions*, CDF internal note 3070 (1996). The scale factor we use is also consistent with CDF Collaboration, F. Abe *et al.*, Phys. Rev. Lett. **79**, 4760 (1997).

[31] M. Mangano, *The Unweighting of Matrix Element Monte Carlos*, CDF internal note 1665 (1991).

[32] D. Gerdes, *Improved Unweighting of VECBOS Monte Carlo Events*, CDF internal note 3180 (1995).

[33] T. Sjostrand and M. Bengtsson, Comput. Phys. Commun. **39**, 347 (1986); T.Sjostrand and M. Bengtsson, Comput. Phys. Commun. **43**, 367 (1987).

[34] J.P. Done, M. Chertok, and T. Kamon, *Study of Run-1B Lepton Identification Efficiencies for SUSY Searches*, CDF internal note 4218 (1997).

[35] M. Kruse *et al.*, *High P_t Lepton ID Efficiencies for Run 1b*, CDF internal note 2883 (1994).

[36] M. Pillai, *Momentum Dependence of Efficiencies of Muon Identification Cuts*, CDF internal note 3776 (1996).

[37] S. Kopp and C. Grosso-Pilcher, CDF Note 1992 (1993).

[38] M. Krasberg and T. LeCompte, *CMCOS: The Run 1A Cosmic Ray Filter*, CDF internal note 2032 (1993).

[39] J.P. Done, M. Chertok, and T. Kamon, *Study of Run-1B Lepton Isolation Efficiencies for SUSY Searches*, CDF internal note 4291 (1997).

[40] The routine includes trigger efficiencies from CDF notes 4700, 3665, 2596, 2391, 2795, 3028, 3622, 2795, 3060, 4076 and 4017.

[41] F. Abe, *et. al*, (The CDF Collaboration), Phys. Rev. **D 52** 2624 (1994).

[42] This concept for the second Z^0 filter comes from G.Apollinari *et. al* , *Measurement of the ttbar production cross section using SECVTX tags*, CDF internal note 3855 (1997).

[43] CDF Collaboration, F. Abe *et al.*, Phys. Rev. D **50**, 2966 (1994).

[44] The matrix is coded in the file fake_sumet_qjtb_opt3.dbt. This file is accessed using secfak_ii.cdf. Both files were shown to us by Rob Roser.

[45] D. Buskulic *et al.*, Phys. Lett. B **313**. 535 (1993).

[46] The CDF implementation of *jet probability* is described in D. Gerdes, *B Identification Using Jet Probability*, CDF internal note 2023 (1993).

[47] R. Demina *Study of Charm Efficiency to Jet Probability Tag*, CDF internal note 4444 (1998).

[48] M. Paulini *et al.*, *About the Sample Composition of SECVTX Tagged Single Lepton Data*, CDF internal note 3757 (1996).

[49] D. Cronin-Hennessy and A. Beretvas, *Luminosity at CDF*, CDF internal note 4721 (1998).

[50] M. Chertok *et al.*, *Search for Lepton Number Violating* $\tilde{\chi}_1^0$ *Decay in LS Dielectron + Multijet Events*, CDF internal note 4229 (1998).

[51] A description of the Poisson counting experiment upper limit method which takes predicted backgrounds and errors into consideration is found in J. Conway and K. Maeshima, *Upper Limits on Poisson Processes Incorporating Uncertainties in Acceptance and Background*, CDF internal note 4476 (1998).

[52] The documentation for this program is CERN Applications Software Group, *HBOOK Reference Manual*, CERN Program Library Long Writeup Y250 (1993).

[53] The documentation for this program is F. James, *MINUIT: Function Minimization and Error Analysis*, CERN Program Library Long Writeup D506 (1994).

[54] To determine an upper limit when the mean is approaching zero, the Particle Data Group recommends G. Feldman and R. Cousins, Phys. Rev. **D57**, 3873 (1998).

[55] The CDFII COlloboration, *The CDFII Detector: Technical Design Report*, FERMILAB-Pub-96/390-E (1996).

[56] See T. Kamon *et al.*, *Study of the Inclusive Lepton Trigger Efficiency for the Run 1A SUSY Trilepton Analysis*, CDF note 2596 (1995), and R. Roser and T. Liss, *A Measurement of the Trigger Efficiencies for $t\bar{t}$ Events in Run 1B*, CDF note 3442 (1996).

[57] C. Blyth and H. Still, *Binomial Confidence Intervals*, Journal of the American Statistical Assoc. Vol. 78, No. 381 (1983). For statistics $n > 30$, which are not tabulated in the above reference, the approximation 1-3/n (3/n) is used for the 95% C.L. lower (upper) limit for bins with ε= 100% (0%). This approximation is courtesy of Ed Bedrick, Department of Mathematics, Univ. of New Mexico. It should be noted that for $0 < \varepsilon < 100\%$, the 95% C.L. limit is significantly farther than a standard deviation from the mean of a binomial distribution.

[58] B.R. Martin, *Statistics for Physicists*, Academic Press (1971).